The University of Zambia

School of Engineering

Department of Geomatic Engineering

Assessment of Land Surface Temperature Using Remote Sensing and GIS Techniques for Detection and Analysis of the Urban Heat Island (UHI) Effect

-A Case of Lusaka City

BY

JEDIDIAH CHIBINGA

2019072637

SUPERVISORS:

Dr. P. H. Nyimbili

Mr. M. Sakala

October, 2023

Assessment of Land Surface Temperature Using Remote Sensing and GIS Techniques for Detection and Analysis of the Urban Heat Island (UHI) Effect

-A Case of Lusaka City

By Jedidiah Chibinga - 2019072637

ABSTRACT

Unchecked urbanization worldwide has caused irreversible ecological damage, elevating Land Surface Temperatures (LST) and the Urban Heat Island (UHI) effect, and posing a serious risk to natural habitats. Lusaka is undergoing this trend, yet research on UHIs in African cities, especially Lusaka, is limited. This study utilised remote sensing through Landsat and MODIS to explore 25 years of winter and summer LST variations. The analysis utilised UHI intensity, the urban-rural gradient, and LST-land cover correlations and included. Heat Vulnerability Indices (HVIs) to map out heat-related risks. The findings uncovered much lesser daytime LST in urban areas compared to rural ones, but an inverse pattern at night. While winter LST had decreased (~Δ0.2℃), summer LST had risen (~Δ6℃), signifying an alarming trend. Areas with higher proportions of bare land were more vulnerable to extreme heat events. This research aims to inform urban planning to the UHI effect in Lusaka.

Keywords: remote sensing, GIS, google earth engine, urban heat island, heat vulnerability index, landsat, MODIS, night-time UHI, summer and winter UHI.

Supervisor:	Supervisor: ....
Signature:	Signature: ....
Date: …………………………………………...	Date: ……………………………………….

The University of Zambia

School of Engineering

Department of Geomatic Engineering

Assessment of Land Surface Temperature Using Remote Sensing and GIS Techniques for Detection and Analysis of the Urban Heat Island (UHI) Effect

-A Case of Lusaka City

BY

JEDIDIAH CHIBINGA

2019072637

SUPERVISORS:

Dr. P. H. Nyimbili

Mr. M. Sakala

“This report is submitted in partial fulfilment for the award of the degree of Bachelor of Engineering, University of Zambia”

DECLARATION

I, JEDIDIAH CHIBINGA, hereby declare that this report being submitted is my work and has, to the best of my knowledge, not been produced or submitted at this University or any other institution and that all sources of information have been duly acknowledged.

I, therefore, will be solely responsible if any kind of plagiarism is found.

ACKNOWLEDGMENT

I would like to share my sincere gratitude to everyone who has helped with the completion of this project. During the work, I faced many challenges due to my lack of knowledge and experience these people helped me overcome these challenges.

I would like to express my profound gratitude to the University of Zambia for providing me with the resources, facilities, and a conducive academic environment necessary for the successful completion of this research project.

I am also deeply appreciative of the guidance, support, and mentorship provided by my supervisors, Dr. P. H. Nyimbili and Mr. M. Sakala. Their expertise, patience, and unwavering commitment throughout this research have been invaluable. Your insights and guidance have been a source of inspiration, and I am grateful for the knowledge and skills I have gained under your mentorship.

I would also like to thank Christopher Shilengwe and my other colleagues and fellow students who provided support, shared valuable insights, and encouraged me throughout this research journey.

Finally, I extend my gratitude to my family and friends for their unwavering support and understanding during this period of intense study and research.

Thank you All.

DEDICATION

I would like to dedicate this research to my parents and my lovely brothers and sisters; Joel, Jessica, Joanna, and Jonathan. I am thankful for their love and continuous encouragement and support and love throughout my tertiary education.

SUMMARY

Rapid and uncontrolled urbanisation in numerous major cities around the world has led to negative irreversible changes in their natural environments and ecology. This has resulted in an increase in Land Surface Temperatures (LST) and the Urban Heat Island (UHI) effect which has the potential to adversely affect the health and well-being of the environment's habitats. The city of Lusaka is not exempt from this global trend. However, the research into UHIs in African cities, and particularly in Lusaka, is notably scarce. To bridge this gap, this study aimed to identify and analyse the UHI effect in Lusaka while identifying the degrees of susceptibility of different areas within the city to this phenomenon. Remotely sensed Landsat and Aqua/Terra-MODIS imagery from Google Earth Engine (GEE) was used to identify and assess the spatial and temporal winter and summer LST changes over the past 25 years. The assessment included analysis of the urban-rural gradient, UHI intensity, and relationships between LST and land cover. Furthermore, Heat Vulnerability Indices (HVIs) were constructed to illustrate the geographical distribution of heat-related risk. The results showed lower urban LSTs compared to rural areas during the day and opposite effects at night. In addition, over the years, winter and summer LSTs have decreased (~Δ0.2℃) and increased (~Δ6℃), respectively. Notably, a strong relationship was identified between densities of bare land and impervious surfaces (positive), and vegetation and water (negative). Consequently, regions with higher densities of land cover linked to positive relationships faced a higher risk of instances of extreme heat and vice versa. In addition, summer LSTs would continue to rise if current urbanisation and land use trends prevail. These findings hope to serve as a valuable resource for urban planning and design, offering actionable insights to mitigate the adverse impacts of the UHI effect in Lusaka.

Keywords: remote sensing, GIS, google earth engine, urban heat island, heat vulnerability index, landsat, MODIS, night-time UHI, summer and winter UHI.

TABLE OF CONTENTS

LIST OF FIGURES

LISTS OF TABLES

LISTS OF APPENDICES

ABBREVIATIONS

UHI	Urban Heat Island
GIS	Geographic Information System
GEE	Google Earth Engine
RS	Remote Sensing
LST	Land Surface Temperature
LULC	Land Use/Land Cover
HVI	Heat Vulnerability Index
RF	Random Forest
MODIS	Moderate Resolution Imaging Spectroradiometer
NDVI	Normalized Difference Vegetation Index
ETM+	Enhanced Thematic Mapper Plus
OLI	Operational Land Imager
NIR	Near Infrared
TIR	Thermal Infrared
SWIR	Short-wave Infrared

CHAPTER: 1

INTRODUCTION

1.1. Background

Since Zambia's independence, Lusaka experienced rapid population growth and urban expansion. Its population has grown from 0.12 million in 1963 to 1.7 million in 2010 and is currently estimated to be over 2 million (Simwanda and Murayama, 2016). This rapid population growth has been largely attributed to mass urbanization as much of the country's population seeks a better life in the nation's capital (UN-Habitat, 2007). For the most part, this rapid urbanization has resulted in unplanned settlements that are mostly concentrated around the city's centre (Chitonge & Mfune, 2015).

To cope with the population boom, the city has also experienced rapid and haphazard development in several sectors such as the infrastructural sector which is of significant interest in this study. This increase in infrastructure has led to changes in Land Use and Land Cover (LULC) (Simwanda et al., 2020) which in turn have led to the altering of the Land Surface Temperatures (LST) within the city. These changes put the city under constant ecological and environmental threats.

One of the most widely documented ecological effects is the phenomenon known as the Urban Heat Island (UHI) effect. This phenomenon is characterized by higher temperatures in urban areas compared to their surrounding rural areas. It is primarily caused by the modification of land surfaces due to urbanization (Fuladlu et al., 2019), leading to altered energy balances and reduced natural cooling mechanisms. The UHI effect has significant implications for urban environments, including impacts on human health, energy consumption, and environmental sustainability (Sebaibi, 2021). Therefore, accurate assessment and analysis of land surface temperature (LST) within urban areas are crucial for understanding and mitigating the UHI effect.

Remote sensing, along with Geographic Information Systems (GIS) techniques, has emerged as a valuable approach for assessing LST and analysing the UHI effect (De Almeida et al., 2021). Remote sensing utilizes satellite or airborne sensors to capture information about the Earth's surface from a distance. It utilizes sensors with specific spectral bands to capture thermal signatures, allowing for the estimation of surface temperatures (Imhoff et al., 2010). Therefore, it provides spatially explicit data on LST, allowing for large-scale monitoring and analysis of urban heat patterns.

GIS techniques complement remote sensing by enabling the integration, analysis, and visualization of LST data along with other relevant geographic and environmental information. Google Earth Engine (GEE), which is a cloud computing platform, allows for the acquisition and integration of LST data with other geospatial datasets, such as land use/land cover maps, and topographic information for the analysis, and visualization of LST data (Galodha & Gupta, 2021). Through spatial analysis and modelling, GIS enables the identification of spatial patterns, hotspots, and gradients of LST, facilitating the detection and quantification of the UHI effect.

Several studies have utilized remote sensing and GIS to carry out several investigations that enable the assessment of the UHI effect. Roy and Bari, 2022 used GEE to filter, process, and analyse trends in land surface temperature and landscape features with logistic regression. It leveraged spectral indices to derive images of Landsat 5 Thematic Mapper (TM), and Landsat 8 Operational Land Imager (OLI) of Sylhet Sadar Upazila, Bangladesh, from 2000 to 2018. Another study by Arellano & Roca, (2023) used MODIS imagery to determine night-time LST in the metropolitan areas of Barcelona, contrasting Landsat's very limited night-time images with daytime ones. In this research, Landsat 5 and 8, and MODIS satellite imagery from Google Earth Engine were used to carry out similar investigations on Lusaka’s urban landscape.

In addition, studies have shown that extreme hot weather conditions have been associated with increased morbidity and mortality, but risks are not evenly distributed throughout the population (Reid et al., 2012). Therefore, Heat Vulnerability Indices (HVI) have been used to geographically locate populations with increased vulnerability to heat. For example, (Conlon et al., 2020) measured the vulnerabilities of different census tracts of Detroit, Michigan, USA, by considering factors that affect peoples’ vulnerability to extreme heat such as environmental exposure, population sensitivity, and adaptation capacity.

In recent years, numerous studies have employed remote sensing and GIS techniques to assess LST and investigate the UHI effect in various urban areas worldwide. Therefore, this study conducts an assessment of the surface UHI effect in Lusaka using LST through various geospatial approaches. In addition to this, it aims to identify areas within the city that would be particularly susceptible to the impacts of the UHI if mitigation efforts are not put in place. This will provide valuable insights into the spatial extent, temporal dynamics, and contributing factors of UHI, supporting evidence-based decision-making for urban planning, climate adaptation, and public health interventions.

1.2. Problem statement

The city of Lusaka’s population is rapidly growing, and so are the demands for various necessities especially that of infrastructural development. Meeting these demands has led to changes in the city’s geographical landscape such as the loss of vegetation cover and the increase in the amount of surfaces that quickly heat up during the day and slowly release heat at night. As a result, this could lead to an increase in land surface temperatures which if left unchecked can lead to heat-related illnesses and death among vulnerable populations such as older adults, very young children, and people with underlying illnesses such as diabetes, obesity etc, as well as increased energy consumption and associated emissions.

In view of the above, this study is aimed at analyzing the land surface temperatures which will aid in UHI effect detection and analysis.

1.3. Main Objective

The main objective of this research was to detect and analyse the Urban Heat Island effect in Lusaka City.

1.4. Specific Objectives

The main objective of the research was attained by achieving the following specific objectives:

i. To determine the characteristics of the UHI effect.
ii. To uncover certain contributing factors to the UHI effect.
iii. To identify trends in the UHI effect.
iv. To identify the vulnerability of areas within the city to the UHI effect.
v. To provide valuable and actionable information for urban planners and policymakers.

1.5. Research Questions

This research seeks to achieve the above objectives by answering the following questions:

i. Does the UHI effect exist in the city of Lusaka?
ii. What are some of its likely sources and characteristics?
iii. How does the UHI effect vary temporally, i.e., from day to night, winter to summer, and over the years?
iv. How significant of a threat is the UHI effect currently?
v. Which areas of the city are most susceptible to heat risk?
vi. What potential local mitigation efforts can be put in place?

1.6. Significance of study

Studying the Urban Heat Island effect in Lusaka is essential for understanding and addressing the challenges associated with urbanization, climate change, public health, energy consumption, and environmental sustainability. Information derived from this study will aid the city in developing evidence-based policies and strategies to create more liveable, resilient, and sustainable urban environments.

CHAPTER: 2

LITERATURE REVIEW

The UHI effect is a phenomenon that exists when metropolitan cities experience higher temperatures compared to the surrounding rural countryside (Logan, 2021). Temperature differences between cities and the countryside can vary by 5 degrees Celsius during the daytime and 3 degrees Celsius during the night-time (US EPA, 2022). According to (Druckenmiller, 2023), several factors are known to cause the UHI effect, these include low urban surfaces which quickly heat up during the day and slowly release heat at night, urban geometries with tall buildings that can create an urban canyon effect that blocks wind flow and traps heat near the surface, anthropogenic heat from cars, air conditioning units, and industrial facilities, and the urban greenhouse effect which can trap and amplify heat above cities.

There are generally two forms of UHI's. Surface UHIs (SUHI) which are measured from artificial and natural surfaces, and Atmospheric UHIs (AUHI), which are measured from air temperatures ranging from the surface to either the layer of air where people live, below the tops of trees and roofs (canopy layer UHI) or high altitudes, where urban landscapes no longer influence the atmosphere ~1.5 km (boundary layer UHI) (U.S. Environmental Protection Agency, 2008; (Branea et al., 2016)).

Remote sensing, through the use of satellites with optical sensors capable of detecting thermal infrared radiation emitted from the surface of the earth, has been used in studies all over the world to assess LST and investigate the UHI effect. Simwanda et al. (2019) in particular for the study of UHIs utilized LST derived from Landsat 8 data to spatially analyse the characteristics of UHIs in four different African cities. However, when investigating LST over several decades, multiple satellites with thermal capabilities such as Landsat 5 in conjunction with Landsat 8, have to be utilized as individual satellites generally will not cover that period (Ranagalage et al. 2019). Most satellites have temporal resolutions of several days. However, when it comes to investigating day and night LST, ideal satellite sensors, such as the Moderate Resolution Imaging Spectroradiometer (MODIS) sensors on board the Terra and Aqua satellites, should have at least twice-daily temporal resolutions (Wang et al., 2020).

Several studies have found that changes in Land Use/ Land Cover (LULC) patterns also impact the intensity and spatial patterns of the UHI effect. Simwanda et al. (2019) found significant correlations between the mean LST and LULC metrics such as the patch density, size, shape, complexity, and aggregation of the LULC. The study found that larger and contiguous green spaces produced stronger cool island effects than those of several smaller patches of green space whose total area equals the large, contiguous patches. The opposite was true about impervious surfaces. Therefore, it concluded, just like other studies it referred to, that LULC is an important factor in mitigating or exacerbating the surface UHI effects.

The temporal dynamics of LST and LULC are important aspects when it comes to assessing the UHI effect. This is carried out by conducting a time series analysis of LST in an area and examining daily and seasonal variations over several years. Ullah et al. (2023) used this method to analyse the influence of LULC on LST in a large urban area of Tianjin from 2005 to 2020. It found that a 5.94% increase in the built-up area increased the LST by 1.5%, while an increase in vegetation cover by 10% showed a negative correlation. In addition, the study concluded that LULC has a cooling effect of about 1.40 ◦C in the city and its average warming effect was about 0.5%. Finally, this study also found that built-up areas had a surface temperature increase from 28.86 °C to 37.23 °C between 2005 and 2020, while in the empty ground area, they increased from 21.56 °C to 25.01 °C.

Heat Vulnerability Indices (HVI) have also been used in studies when assessing the UHI effect to represent overall heat risk which can help identify susceptible regions and sub-populations in cities in the face of cases of extreme heat (Hong et al., 2021). They provide mapping tools to visualize the vulnerability across census tracts in a city through three aspects: environmental exposure, population sensitivity, and adaptation capacity. Exposure quantifies the severity of extreme heat. Sensitivity reflects demographics and pre-existing health condition that increases the risk of developing worse outcomes under similar heat exposure. Adapting to these three aspects entails modifying and reducing the level of heat exposure or sensitivity (City and County of San Francisco). Therefore, HVIs are able to facilitate the design of different heat mitigation strategies based on the spatial information they provide.

GIS played a vital role in the detection, visualisation, and analysis of the UHI effect in most studies. Google Earth Engine (GEE), which is a cloud computing platform has a mammoth archive or library of remotely sensed datasets including LST products from various satellites. In addition to storing remotely sensed data, this platform has analysis and visualisation capabilities which have made it ideal for assessing the UHI effect.

Several studies similar to this research have been conducted. Simwanda et al. (2019), conducted a spatial analysis of SUHIs in Lagos (Nigeria), Nairobi (Kenya), Addis Ababa (Ethiopia), and Lusaka (Zambia). This study examined the relationship between land surface temperature (LST) and the spatial patterns, composition, and configuration of impervious surfaces/green spaces in four African cities. This study used Landsat OLI/TIRS data and various geospatial approaches, including urban–rural gradient, urban heat island intensity, statistics, and urban landscape metrics-based techniques, to facilitate the analysis. Aspects derived from this study included parameters for sub setting the study area, and selecting satellite data, techniques for pre-processing and extracting LST from Landsat data, and of course techniques for analysing the spatial patterns of the UHI effect.

Another study by Ullah et al. (2023), analysed the impact of urbanization on the UHI effect. This study used Google Earth Engine to analyse the relationship between the UHI intensity and Tianjin City’s land cover characteristics. It did so by dividing the land cover characteristics into five categories: built-up, agricultural, bare areas, forest, and water, and investigated their relationship with the LST over fifteen years from 2005 to 2020. Aspects of LULC classification and calculation using GEE, and correlation with LST were derived from this study.

To incorporate HVIs in this research, Hong et al. (2020) study on HVI development and mapping was used to obtain aspects concerning HVI construction parameters and methods, and factors characterising vulnerability to extreme heat. This study developed an HVI web mapping tool that incorporated both outdoor and indoor heat exposure across census tracts in the city of Fresno, California. The tool developed provided both an aggregated single vulnerability indicator, and three sub-indicators highlighting three different aspects of heat vulnerability: environmental exposure, population sensitivity, and adaptation capacity. Finally, to facilitate the design of different heat mitigation strategies, the tool also allowed users to customize the weights of individual factors.

CHAPTER: 3

METHODOLOGY

3.1. Study Area

Lusaka is the capital and largest city of Zambia. The city is located between latitudes 15° 18′ 08″ S and 15° 35′ 08″ S, and longitudes 28°11′ 59″ E and 28° 29′ 13″ E with an average elevation of 1260 m above mean sea level. Lusaka is situated in a relatively flat area that covers approximately 360 square kilometres. Escarpments lie to the east and north of Lusaka, which end in the Luangwa Valley (Nguvulu and Okello, 2017). According to (Kottek et al. 2006), the climate of Lusaka is classified as Cwa (C = Mild temperate w = Dry winter a = Hot summer) implying that it is mild or temperate with generally dry winters and hot summers, and an average annual temperature, evapotranspiration, and precipitation of 20.0°C, 2218mm, and 650 mm respectively. At a monthly average temperature of 28.9°C, October is the hottest month of the year while July, with a monthly average temperature of 9.6°C is the lowest average temperature of the whole year.

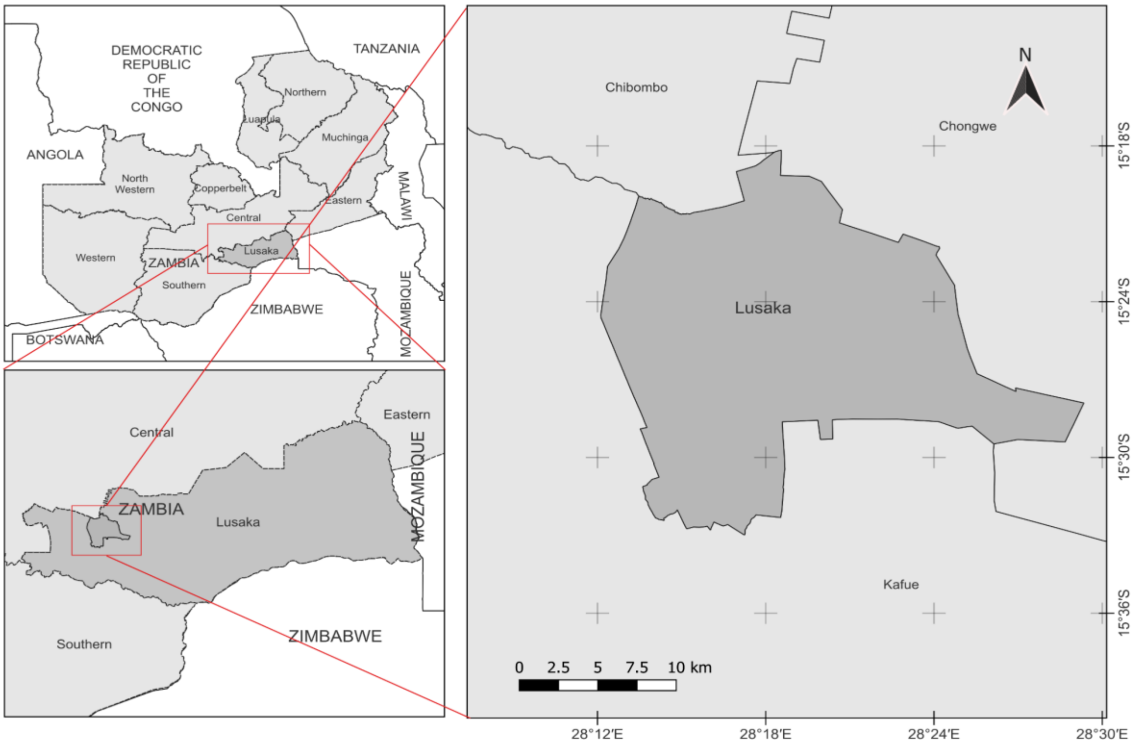

Figure 3.1. Location map of study area

In addition to the city of Lusaka, the study area also included a 40 km × 40 km subset with a 20 km radius from the centre of the city, extending beyond the confines of the city. This was done to enable the assessment of land surface temperatures of the rural areas surrounding the city as well.

3.2. Methods

The flowchart in the diagram below depicts a summarized breakdown of the steps that will be undertaken to achieve the specific objectives of the research. Each of the steps will elaborated further in the subsequent sections.

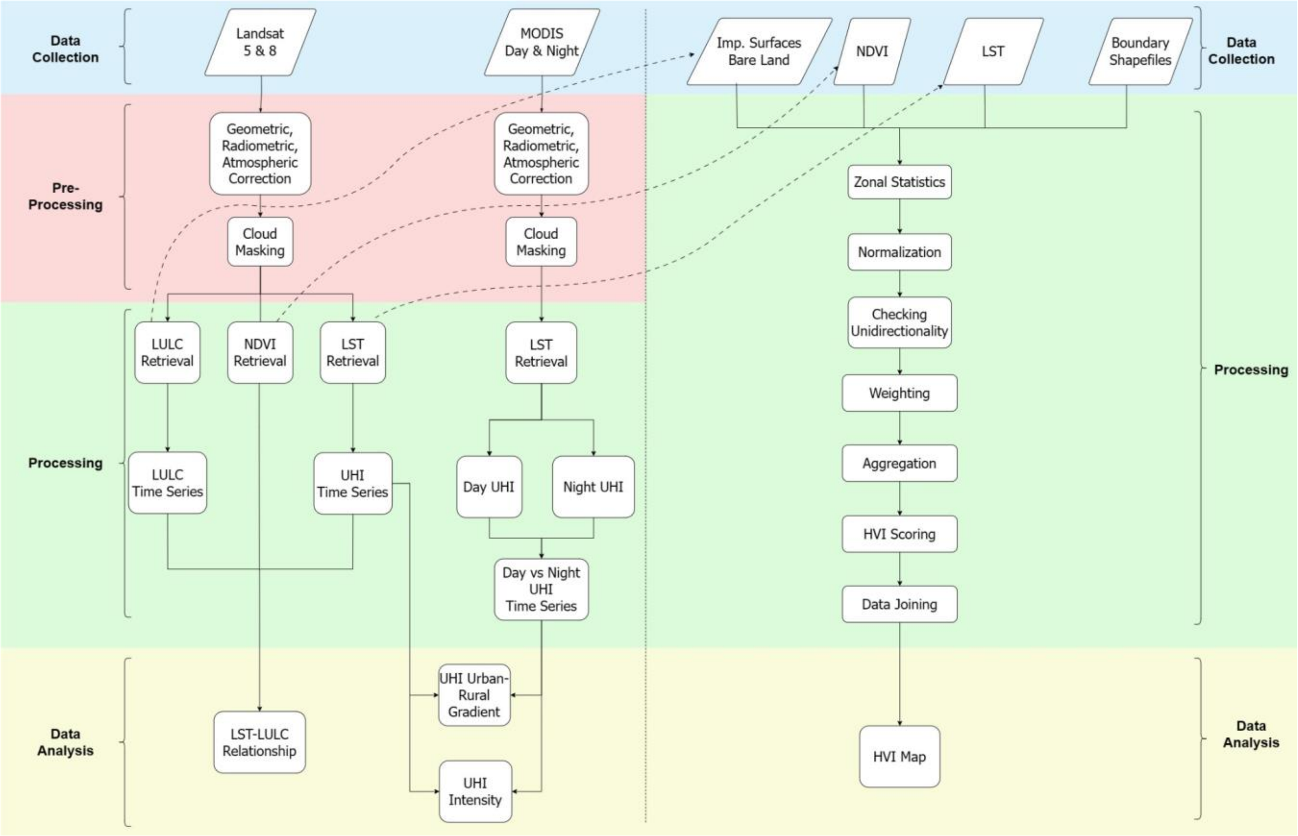

Figure 3.2. Flowchart of workflow.

The collection of data that was to be analysed to achieve the objectives of this research was carried out as shown in the methodology flowchart. The subsequent sections aim to elaborate on the methodology and describe the datasets used and the platforms that facilitated acquiring this data.

3.2.1. Data Collection

To assess the UHI effect in the city of Lusaka, land surface temperatures had to be acquired. Through the use of Google Earth Engine (GEE), this research used a combination of Landsat and MODIS satellite imagery to facilitate the acquisition of the land surface temperatures over about twenty-five years.

GEE was used primarily because it provides access to a large and diverse collection of geospatial datasets that are analysis-ready (pre-processed and harmonized to enable consistent and accurate analysis) and it also allows one to perform fast and scalable analysis on the cloud (Earth Blox, 2022).

3.2.1.1. Landsat

Landsat imagery was the primary source of LST data that was collected for this research because it is capable of providing easily accessible imagery over several decades, with a good balance between spatial and temporal resolution. However, its spectral resolution consisting of bands from the blue to the shortwave and near-infrared spectrums, and most importantly, thermal-infrared bands for assessing land surface temperatures idealized its selection (USGS, n.d.).

Satellite images from two Landsat satellite missions were acquired because no single satellite could provide imagery for the required period. Landsat 5 was used to collect 6 images of the study area from between 1998 and 2008. Additionally, Landsat 8 was used to collect 6 images of the study area from between 2015 and 2022. Therefore, a total of 12 Landsat satellite imagery were collected of the study area.

All the imagery collected was cloud-free (<15%) for the years 1998, 2005, 2008, 2015, 2020, and 2022. This imagery was obtained over twenty-five years to assess the temporal variation and trends of the LST.

The Landsat 5 and 8 imagery for each of the years was collected for both the cold (May to July) and hot/dry (September to November) seasons of the year. Imagery from the cold season was chosen because it occurs right after the wet season. This was required to investigate LST during a period with significant green spaces and therefore further investigate the influence of green spaces on LST.

In addition, imagery from the hot/dry season was chosen to eliminate non-permanent green spaces that only exist during the wet season, and therefore investigate LST during the hottest time of the year when the UHI tends to be most significant. Therefore, a total of 24 Landsat satellite imagery were collected of the study area.

3.2.1.2. MODIS

MODIS imagery from the Terra satellite was a secondary source of imagery for this research to supplement the imagery provided by Landsat. Despite its very low spatial resolution, this satellite source was selected due to its very high twice-daily temporal resolution, meaning that it was able to provide day and night LST (NASA, n.d.).

MODIS imagery collected was also cloud-free and from winter and summer times of the year. However, the imagery acquired was the mean LST between of the years 2000-2002, 2005-2007, 2010-2012, 2015-2017, and 2020-2022. Day and night imagery was acquired for this period to measure the variation of the LST between the day and night time.

3.2.1.3. Heat Vulnerability Index (HVI)

It was not going to do this research justice by only investigating and assessing the characteristics of LST to detect and analyse the UHI. It was therefore necessary that actionable and informative information be presented from the data derived from the Landsat imagery. In this vain, information needed to be provided as to the varying degrees of susceptibility of residents of particular areas of the city of Lusaka to instances of extreme heat. This research aimed to do so by constructing a heat vulnerability map after considering different factors that are capable of exacerbating the effects of extreme heat.

Several factors are considered when assessing a population's vulnerability to heat. These factors are generally grouped into three categories, namely Environmental exposure which quantifies the severity of extreme heat, sensitivity that reflects demographics and pre-existing health condition that increases the risk of developing worse outcomes under similar heat exposure, and adaptive capacity which indicates factors that modify the level of heat exposure or sensitivity (Hong et al., 2021).

This research focused on the first HVI category, environmental exposure, which encompasses conditions related to the physical environment that contribute to heat vulnerability. Conditions that were considered in addition to the land surface temperatures were impervious surface, vegetation, and bare land. This information was derived from the Landsat 5 and 8 imagery acquired. Finally, neighbourhood boundary a shapefile was generated using data from Google Earth to delineate the HVI of each neighbourhood.

3.2.2. Pre-processing

Satellite pre-processing is an essential step in satellite image analysis as it improves the quality and accuracy of various applications (Shrawankar & Khandare, 2016)

Pre-processing generally involves carrying out corrections such as radiometric calibration, and geometric and atmospheric correction (Shrawankar & Khandare, 2016). However, since the Level 2, Collection 2, Tier 1 Landsat dataset was used, it was not necessary to carry out the corrections as these corrections were already applied to the imagery (Choate et al., n.d.).

Likewise, the MODIS imagery (MOD11A1 - MODIS/Terra Land Surface Temperature/Emissivity Daily L3 Global 1km SIN Grid) also had the required corrections applied to it (NASA LAADS DAAC, n.d.).

3.2.3. Processing

The processing step involved deriving the land surface temperatures and land use land covers from the collected and pre-processed Landsat and MODIS imagery which were then analysed to achieve the research's objectives. In addition, it also involved preparing and merging the HVI factors which were used to obtain the final HVI map.

3.2.3.1. Retrieval of Land Surface Temperature

In order to obtain the LST from the collected Landsat imagery, the Digital Numbers (DN) of the thermal bands (band 6 in Landsat 5 and band 10 in Landsat 8) have to be converted to absolute units of at-sensor spectral radiance while the red and near-infrared bands are used to obtain the Normalized Difference Vegetation Index (NDVI). The spectral radiance and NDVI are then used to obtain the LST in Kelvin as shown in the stepwise process below:

Table 3.1: Stepwise process for LST determination (Ullah et al., 2023).

Process Name	**Equations**
Spectral Radiance (SR)	$L_\lambda = 0.0003342 * DN + 0.1$
Brightness Temperature (T_B)	$T_B = \frac{K_2}{ln((K_1/L_\lambda) + 1)} - 273.15$
Normalized Difference Vegetation Index (NDVI)	$NDVI = \frac{NIR - Red}{NIR + RED}$
Fractional Vegetation (F_v)	$F_v = \frac{NDVI - NDVI_{min}}{NDVI_{max} - NDVI_{min}}$
Surface Emissivity (Sε)	$S\varepsilon = 0.004 * F_v + 0.986$
Land Surface Temperature (LST)	$LST = \frac{T_B}{1 + (\lambda_\sigma T_B/hc)\, ln\varepsilon}$

where λ is the effective wavelength, σ is the Boltz–Mann constant (1.38 × 10−23 J/K), h is the Plank constant (6.626 × 10−34 Js), and c is the speed of light in vacuum (2.998 × 10−8 m/s).

As alluded to in *Section 3.2.2*, Landsat Level 2 imagery was used. This also meant that this dataset contained one thermal infrared (TIR) band (SR_B6 in Landsat 5 and SR_B10 in Landsat 8) processed to orthorectified Surface Temperature (ST) which was used in the calculation of the ST products, as well as Quality Assessment (QA) bands. The presence of these ST bands meant that the steps in Table 3.1 did not need to be carried out as they had already been accounted for in the dataset (NASA, n.d.). Therefore, the only steps that were taken to obtain the Landsat LST were masking out the clouds using the QA_pixel bands and obtaining the LST in degrees Celsius from Kelvin using the scale factor expression:

$$(A * 0.00341802) + 149 - 273.15 \qquad (1)$$

where **A** is the SR_B6 band or SR_B10 band.

Obtaining the LST from the MODIS imagery was very similar to that of Landsat. It only required masking out the clouds using the Quality Control (QC) band and then obtaining the LST in degrees Celsius from Kelvins using the scale factor expression:

$$(A * 0.02) - 273.15 \quad \text{(2)}$$

where **A** is the LST_Day_1km band or LST_Night_1km band.

3.2.3.2. Obtaining Normalized Difference Indices

Many studies have been conducted an index-based approach to examining the relationship between LST and LULC. This approach measures the correlation between LST and LULC indices such as NDVI and NDWI. In this research, these two indices were computed from all the Landsat imagery acquired.

The Normalized Difference Vegetation Index (NDVI) has values ranging between − 1 and + 1 and it enhances all vegetation, resulting in a positive value. Soil may have values close to zero, while waterbody features tend to have negative values (John et al., 2020). NDVI was computed as follows:

$$NDVI = \frac{\rho NIR - \rho Red}{\rho NIR + \rho Red} \quad \text{(3)}$$

where ρRed-reflectance is the red band (band 3 for Landsat 5, and band 4 for Landsat 8) and ρNIR-reflectance is the NIR band (band 4 for Landsat 5, and band 5 for Landsat 8).

3.2.3.3. Extraction of Land Cover

A large amount of literature has demonstrated that the LST of a particular area can be related to and influenced by its land cover. Therefore, Land Use Land Cover (LULC) was extracted after classifying each of the Landsat imagery collected. The land cover classes of interest were impervious surfaces, bare land, water, and green spaces comprised of cropland and natural vegetation.

Impervious surfaces included buildings, transport utilities, and all other impervious areas, green spaces were comprised of forests, grass, and cropland, and water included small lakes, ponds, reservoirs, streams, and rivers.

Supervised classification using the Random Forest (RF) algorithm and pixel-based image classification were used. The RF model used 300 trees and 5 randomly selected predictors per split. In addition, the training sites were randomly split with 80% for training and 20% for testing. RF model was selected due to higher accuracies when using time series satellite images than when using single date images, i.e., when temporal aggregation methods derived from time series images are applied (i.e., the use of metrics such as mean or median) (Phan et al., 2020). Pixel-based classification on the other hand was used after comparing results with object-based classification. Pixel-based image classification gave better results.

The accuracy of the land cover classification results was assessed in GEE using a confusion matrix and the Kappa coefficient was maintained to be not less than 80%.

3.2.3.4. Construction of HVI

To construct the HVI map, zonal statistics were carried out on data derived from the LST and LULC, to obtain information on the mean LST, and the proportions of the land use in each of the boundary areas or neighbourhoods (Poteet, n.d.).

Thereafter, the data was checked for unidirectionality in the data to ensure that higher values depicted increasing vulnerability and vice-versa. This was done by simply subtracting the value from 1.

After ensuring that the data was unidirectional, it was then normalized by scaling the variables to a common range. This step was important because different variables may have different units or scales, and normalizing allowed for fair comparison (Poteet, n.d.). This research used a *z-scoring* method of normalization which measures the number of standard deviations from the mean (Reid et al., 2012). The range of the z-score was then converted to an HVI component score as shown below.

$$Z - score = \frac{[Observed\ value - Mean]}{Standard\ Deviation} \ldots\ldots\ldots\ldots\ldots\ldots\ldots\ldots \quad (4)$$

Table 3.2: Conversion of range of Z-Score to HVI component score (Reid et al., 2019).

Range of Z-Score	HVI Component Score
-2 or lower	1
-2 to -1	2
-1 to 0	3
0 to 1	4
1 to 2	5
2 or higher	6

Weights are generally assigned to each variable based on its relative importance in contributing to heat vulnerability. For example, factors like impervious surfaces would be assigned higher weights as they are deemed to have a more significant impact on vulnerability (Hong et al., 2021). In this research, no weights were assigned to the HVI scores.

The normalized and weighted variables were then combined into a single composite index. This was done through simple weighted summation (Poteet, n.d.). The result was a single score for each geographic unit (neighbourhood).

The composite index calculated in the previous step represented the Heat Vulnerability Index (HVI) or HVI score in other terms. It quantified the overall vulnerability of each geographic unit. The higher the HVI score the greater the vulnerability to heat-related risks (Hong et al., 2021).

Finally, data joining was carried out to combine the HVI scores with spatial data, which in this case was the geographic information system (GIS) shapefile, to associate the vulnerability scores with specific geographic areas or neighbourhoods. This step allowed for the creation of a spatial representation of the HVI which could be depicted on a map.

3.2.4. Data Analysis

QGIS in conjunction with Microsoft Excel was used to analyse the data collected and processed in Google Earth Engine. The methods alluded to in the subsequent section were employed to analyse and assess the LST to detect the UHI and its characteristics.

3.2.4.1. Urban-Rural Gradient

The urban-rural gradient measures the spatial variation in temperature within an urban area compared to its surrounding non-urban or rural areas. This method of analysis involved the creation of concentric rings or buffer zones around the city centre with standard distance intervals extending to the rural areas (Ranagalage et al., 2019).

The steps employed in this analysis were mainly drawn from Simwanda et al., 2019, who conducted a similar analysis. This research similarly adopted the 200m interval concentric rings for the Landsat UHI gradient and analysis. On the other hand, 1000m interval concentric rings for the MODIS UHI gradient and analysis due to the low spatial resolution (1000m) of the imagery. To complete the analysis, the mean temperatures in each of the ring intervals were obtained to measure the temperature gradient.

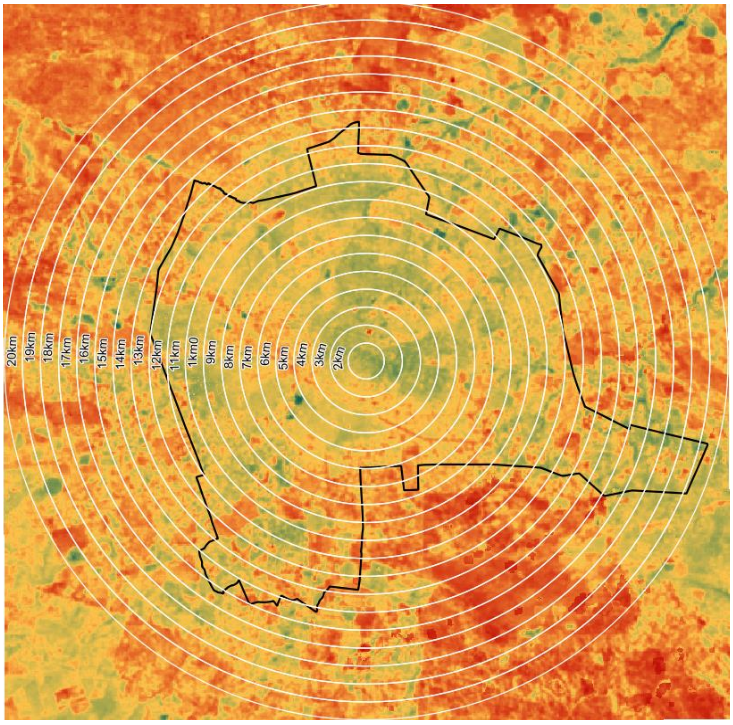

Figure 3.3. 1000m interval buffer setting for calculating MODIS UHI gradient and intensity. A 200m interval buffer setting was used for calculating Landsat UHI gradient and intensity.

3.2.4.2. UHI Intensity

The UHI intensity measured the magnitude of the temperature difference between the urban and rural environments. It quantified how much warmer the urban area is compared to the rural areas.

To carry out this analysis the urban and rural areas were delineated based on the physical extent of the built-up or impervious surfaces (Simwanda et al., 2019). This was done because the administrative boundaries of a city are not a reliable means of defining an urban area as boundaries tend to change over time, and are therefore not comparable when conducting a time series analysis causing them to be over- or under-estimated (Herold et al., 2002).

Therefore, concentric zones defined in Section 3.2.4.1 were used to determine the urban area. All concentric zones that contained impervious surfaces with percentages greater than 10 were classified as urban areas while the rest beyond the maximum radius of the urban or built-up footprint were considered as rural. The impervious surface value minimum of 10% was chosen after superimposing the concentric rings and land cover imagery and identifying the impervious cover percentage at which the urban or built-up footprint ended.

The UHI intensity was therefore calculated using the expression:

$$UHI\ Intensity\ = LST_{urban} - LST_{rural} \ldots\ldots\ldots\ldots\ldots\ldots \quad (5)$$

where LST_{urban} - represents the LST in urban areas

LST_{rural} - represents the LST in rural area.

3.2.4.3. LST-LULC Relationship

This method of analysis involved carrying out various sub-analyses to investigate the relationship between land surface temperatures and the land covers of regions in the study area.

The first analysis involved extracting the mean surface temperatures of each of the land cover classes. This analysis was used to identify which land cover types were of most significance in contributing to the land surface temperatures.

In addition, the densities of impervious surfaces, bare land, and green spaces were determined in each zone and plotted across the urban-rural gradient for each study area. This analysis aimed to identify the LULC-LST relationship along the urban-rural gradient.

Finally, the relationship was also investigated by analysing the correlation between normalized indices and LST and LULC. To achieve this, this research analysed the relationship between the Normalized Difference Vegetation Index (NDVI), and LST.

3.2.4.4. HVI Map

The steps described in Section 3.2.3.5 resulted in a thematic map that was used to visualize the HVI scores across the study area and depict the spatial distribution of heat vulnerability.

Analysis of this map involved identifying areas of high and low vulnerability. The ultimate goal of this analysis was a visual aid that would help inform decision-making and prioritize interventions in areas with the highest vulnerability.

CHAPTER: 4

RESULTS

Before delving into the details of the findings of this research, it is essential to acknowledge the results of extensive data collection efforts that formed the foundation of this research. This chapter presents the outcomes of the collected data that was processed as part of the methodology.

4.1. Land Surface Temperature

The initial and most crucial step of the data collection stage of this research involved the retrieval of land surface temperatures from two different satellites. The outcomes are shown in the subsequent sections.

It is worth noting that from the imagery that was acquired and analysed, only Landsat imagery from the years 1998, 2008, and 2020, and MODIS imagery from 2000-2002, 2010-2012, and 2020-2022 will show in this section.

4.1.1. Landsat

Landsat imagery (60m – Landsat 7, 100m – Landsat 8) was used to obtain winter and summer land surface temperatures of higher spatial resolution compared to that of MODIS (1000m).

4.1.1.1. Winter

As alluded to in Section 3.2.1.1, imagery from the winter was acquired to investigate LST right after the wet season, during a time period with significant green spaces. This was to mainly investigate the influence of green spaces on land surface temperatures. The results are shown in the subsequent figures.

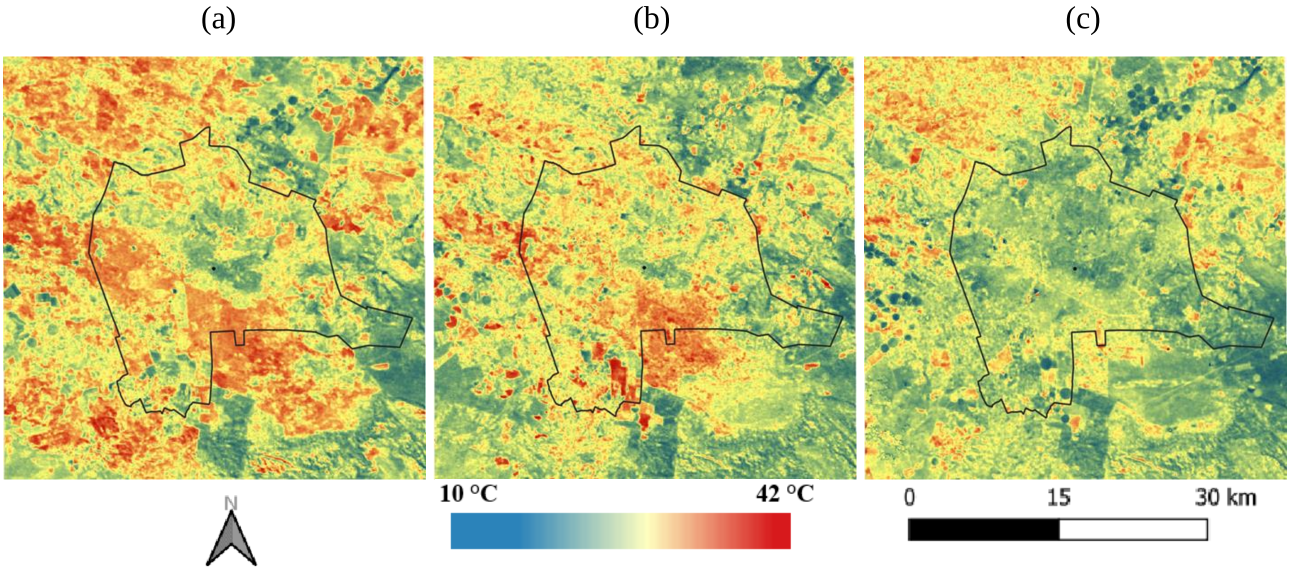

Figure 4.1. Winter Landsat LST for (a) 1998 (b) 2008, and (c) 2020.

Relevant Literature

The research conducted by Simwanda et al. in 2019 also retrieved the winter Landsat LST in and around Lusaka city for the year 2016. Its findings were similar to those obtained in this research and will be further discussed in *Chapter 6*.

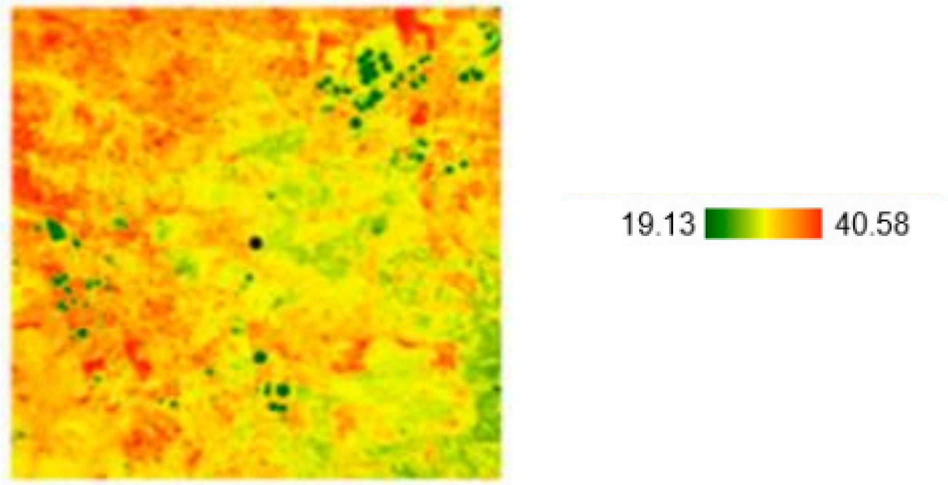

Figure 4.2. 2016 winter LST of Lusaka obtained by Simwanda et al., 2019.

4.1.1.2. Summer

Likewise, imagery from the summer was acquired to eliminate non-permanent green spaces that only exist during the wet season, and therefore investigate LST during the hottest time of the year when the UHI tends to be most significant. The results are shown in the figures below.

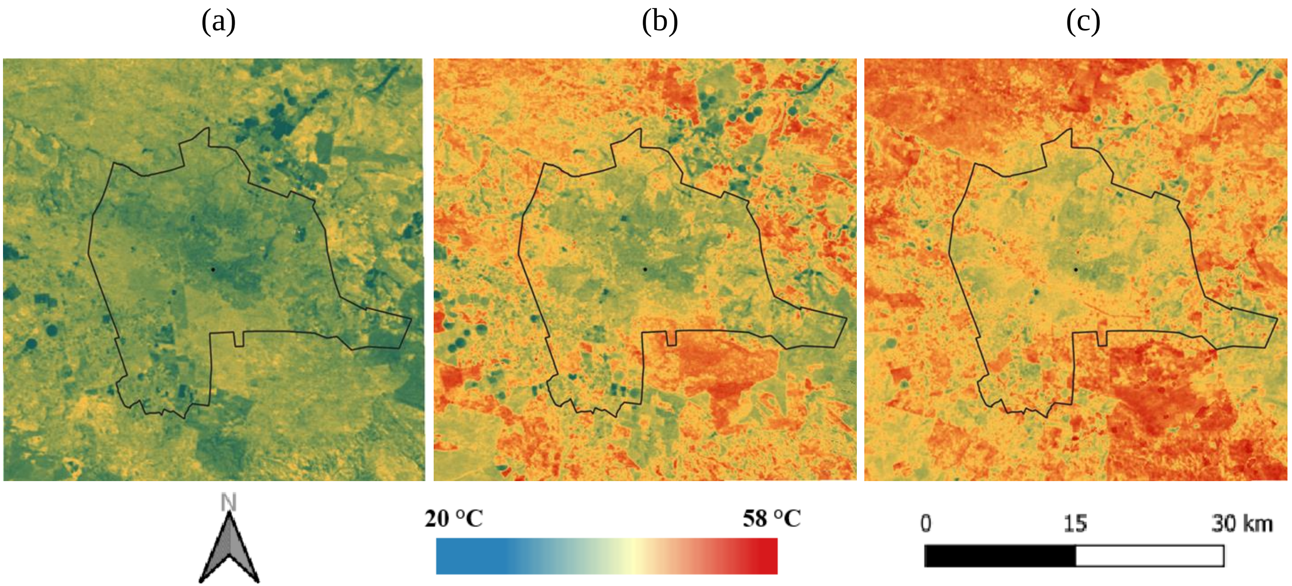

Figure 4.3. Summer Landsat LST for (a) 1998 (b) 2008, and (c) 2020.

4.1.2. MODIS

Despite having a much lower spatial resolution MODIS imagery was used to obtain winter and summer land surface temperatures as well. Its significance however was its ability to provide day and night land surface temperatures.

4.1.2.1. Winter

Just like Landsat, MODIS imagery from winter, with the addition of day and night time imagery, was used to conduct a comparative analysis of land surface temperatures between the two times of the day. The results are shown in the subsequent figures.

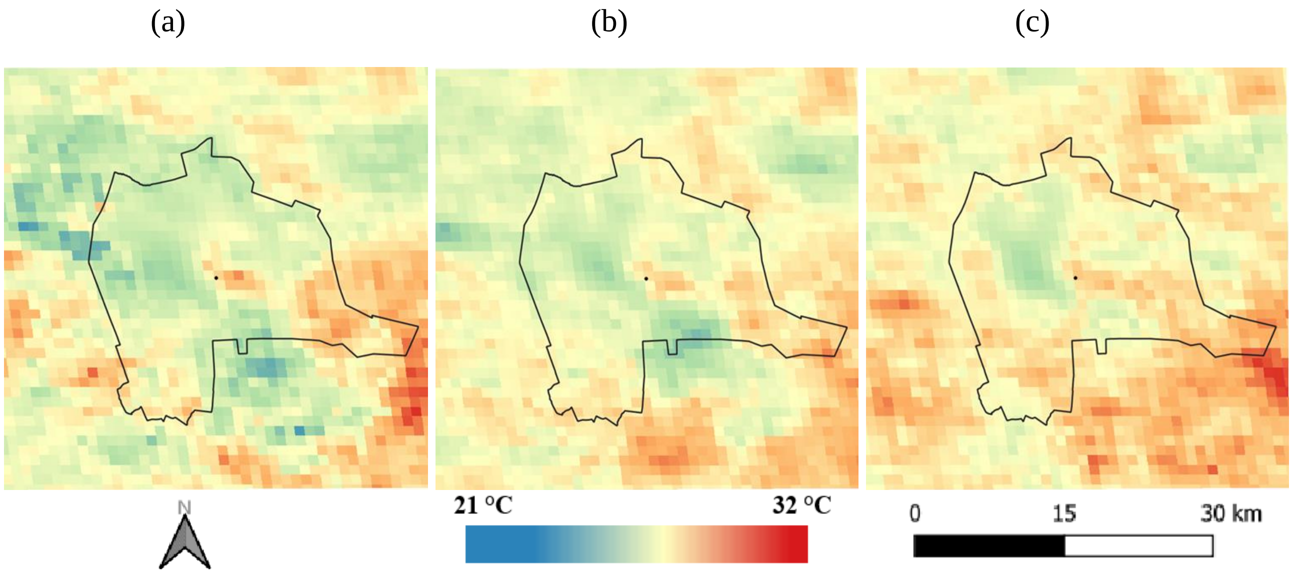

Figure 4.4. Daytime-winter mean MODIS LST for the years (a) 2000-2002 (b) 2010-2012, and (c) 2020-2022.

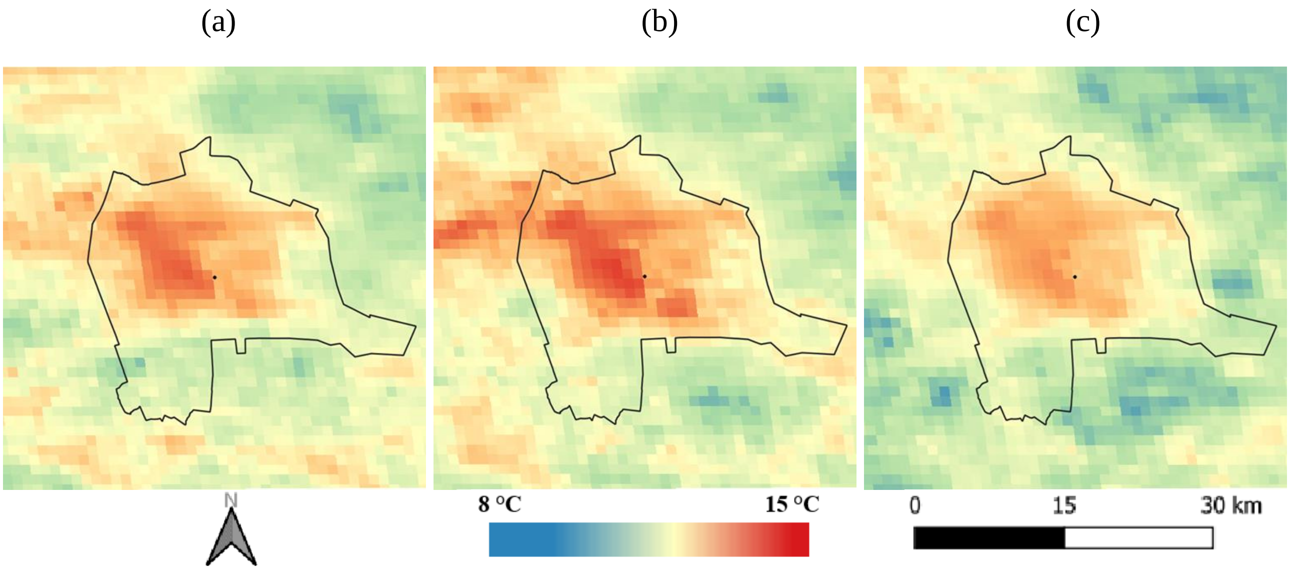

Figure 4.5. Night-time-winter mean MODIS LST for the years (a) 2000-2002 (b) 2010-2012, and (c) 2020-2022.

4.1.2.2. Summer

Similarly, summer day and night-time imagery was also acquired to conduct a comparative analysis of land surface temperatures during the summer. The results are shown in the subsequent figures.

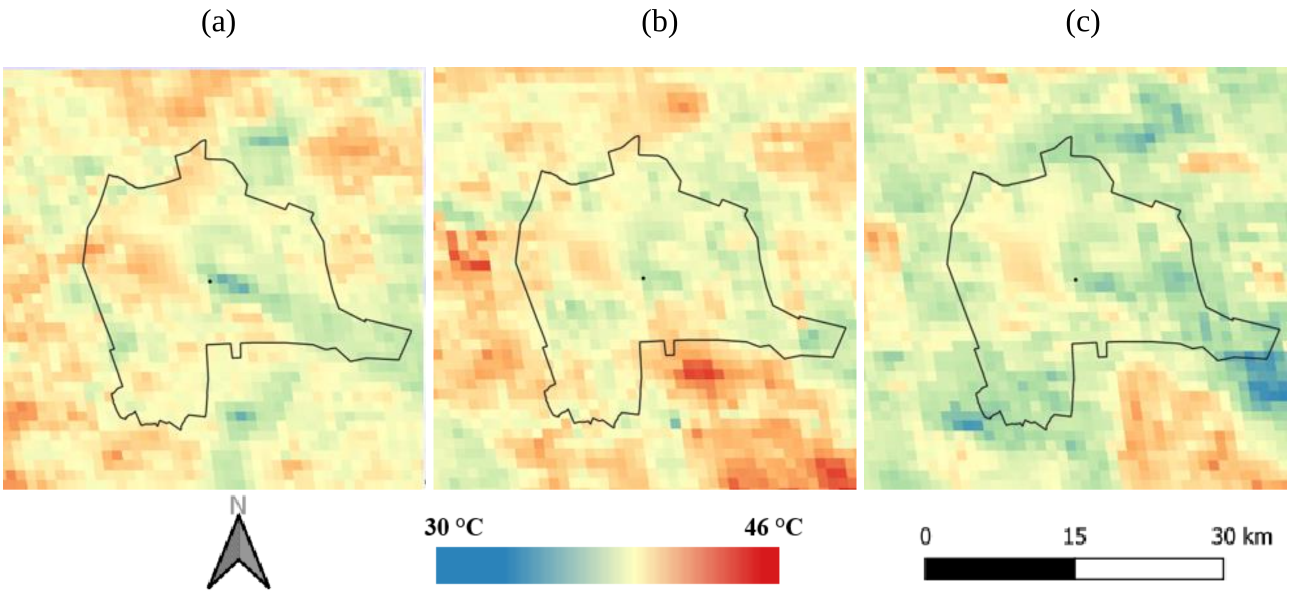

Figure 4.6. Day-summer mean MODIS LST for (a) 2000-2002 (b) 2010-2012, and (c) 2020-2022.

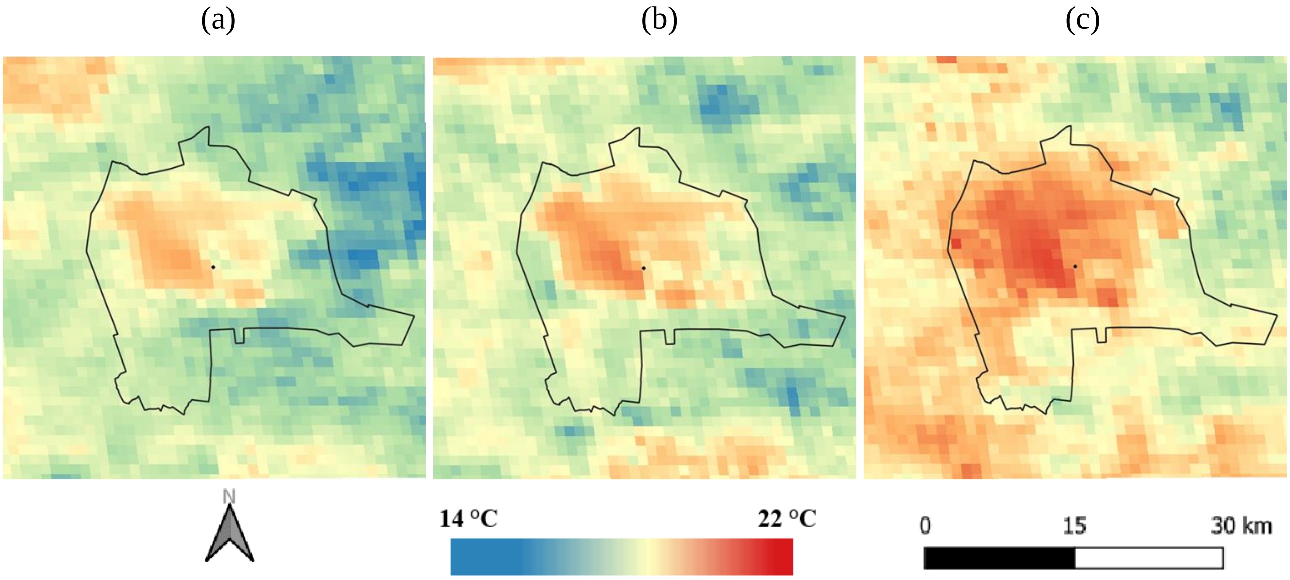

Figure 4.7. Night-time-summer mean MODIS LST acquired for (a) 2000-2002 (b) 2010-2012, and (c) 2020-2022

4.2. Land Use Land Cover

To supplement the analysis of land surface temperatures and provide valuable insights into why certain areas exhibit elevated temperatures while others remain cooler, it was essential to obtain land cover data for the study area as well. The results of the land cover classification using Landsat imagery are shown in the following sections.

Although imagery from 1998, 2005, 2008, 2015, 2020, and 2022 were classified and used in the analysis, only imagery from the years 1998, 2008, and 2020 will be shown in this section.

4.2.1. Winter

Winter land cover was acquired mainly to investigate the influence of green spaces i.e., cropland and natural vegetation, on land surface temperatures. The results are shown in the figures below.

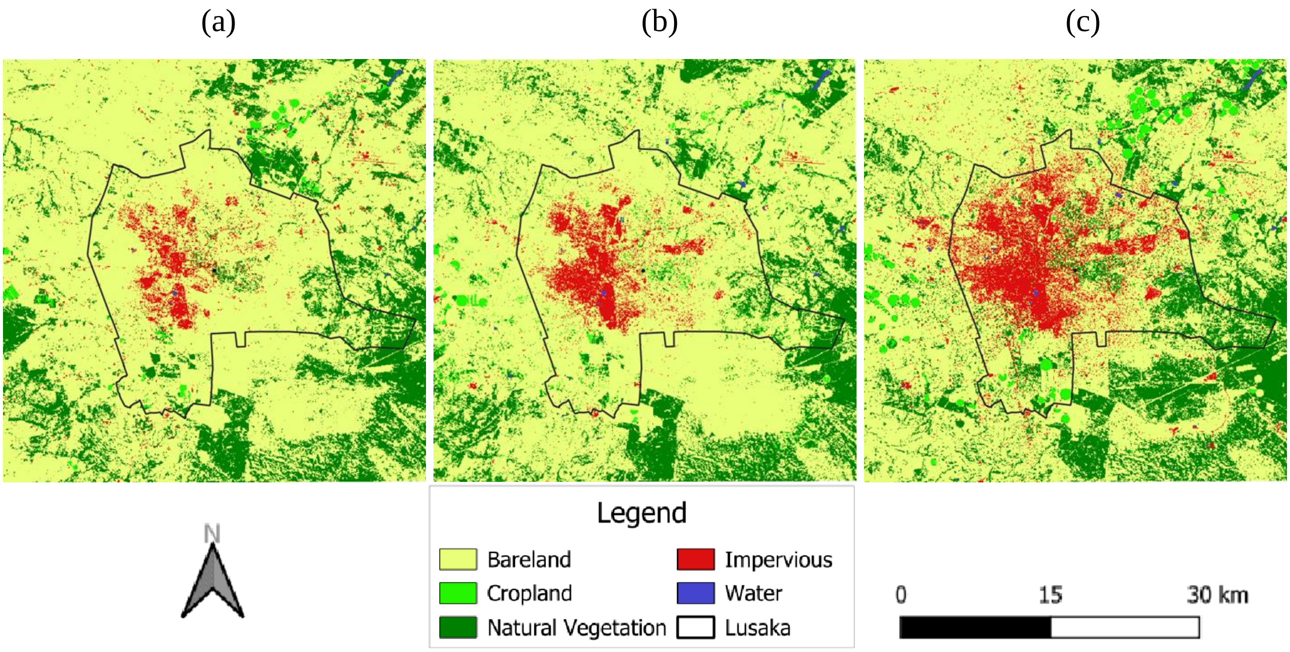

Figure 4.8. Winter Landsat land use land cover for (a) 1998 (b) 2008, and (c) 2020.

4.2.2. Summer

On the other hand, the summer land cover was acquired to investigate the factors influencing land surface temperatures at the most significant time of the year. The results are shown in the figures below.

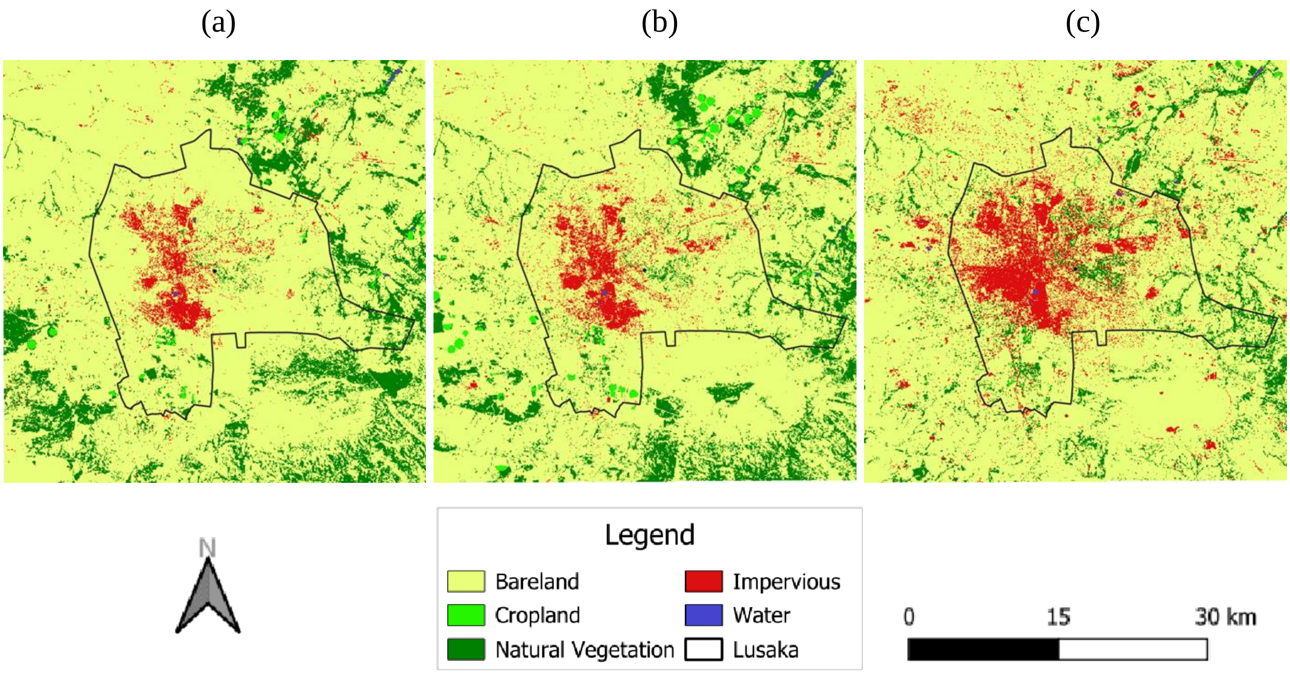

Figure 4.9. Summer Landsat land use land cover for, (a) 1998 (b) 2008, and (c) 2020.

CHAPTER: 5

DATA ANALYSIS

This section, delves into the heart of this research, analysing and scrutinizing the data collected. The primary aim of this analysis is to reveal the intricate characteristics, trends, and underlying factors contributing to the formation of UHIs within Lusaka. To wrap the data analysis up, information susceptibility of different areas within Lusaka to the UHI effect will be uncovered.

5.1. Urban-Rural Gradient Analysis

By definition, the UHI effect occurs when urban areas experience higher temperatures compared to outlying rural areas. This section, therefore, seeks to analyse the characteristics of the UHI with respect to how these temperatures vary from the centre of Lusaka's urban area towards outlying rural areas.

5.1.1. Landsat

Analysis of Landsat imagery provided insight into how this variation occurred in the winter (at the end of the wet season) and during the dry, and hottest time of the year.

From Figure 4.1 and especially Figure 4.3, it is visually discernible that the results show that there seem to be higher temperatures further away from the city centre compared to closer areas. This was counter-intuitive based on the definition of the UHI effect.

Further analysis was carried out to verify this fact, which was also evident in Figure 5.1. This figure showed temperature differences with slopes of +1.4%, -1.0%, and +1.5%, and for the years 1998, 2008, and 2020 respectively.

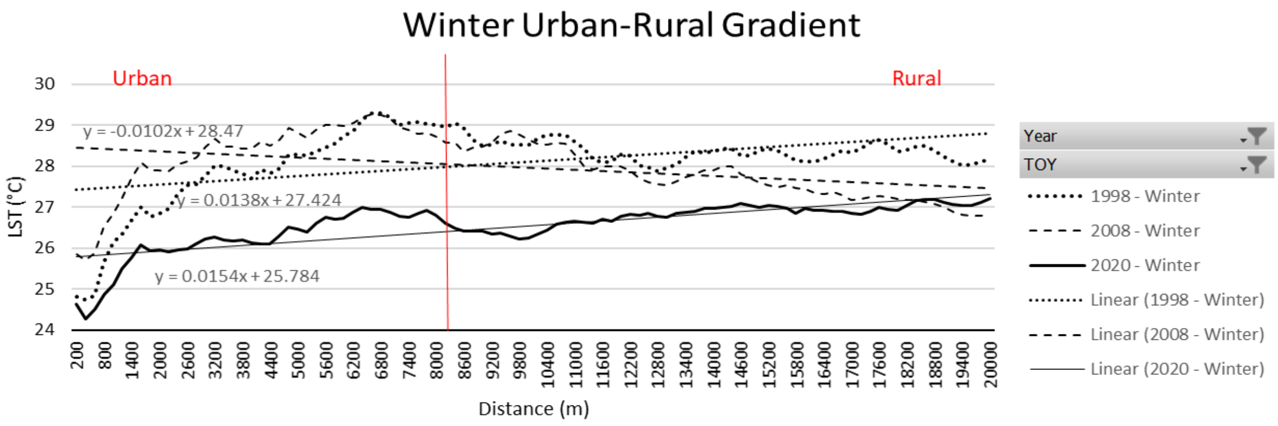

Figure 5.1. Landsat winter UHI urban-rural gradient.

This trend is even more profound in summer. Constant temperature increases can be seen with more than twice as high slopes of up to +3.9%, 4.8%, and +4.4% in the years 1998, 2008, and 2020 respectively.

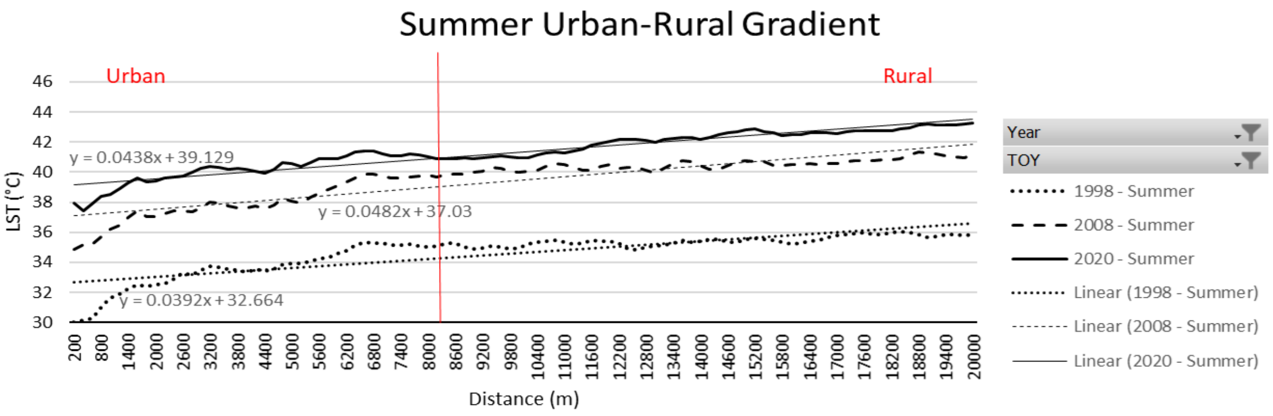

Figure 5.2. Landsat summer UHI urban-rural gradient.

5.1.2. MODIS

This section seeks to deepen the understanding of the UHI characteristics by exploring how the urban-rural gradient varies between day and night time. Despite providing very low spatial resolution LST, MODIS imagery still provided valuable general insight into the day-to-night temporal characteristics of the UHI gradient.

Similar to Landsat imagery in Figure 4.1 and Figure 4.3, daytime MODIS imagery in Figure 4.4 and Figure 4.6 also shows lower LSTs in urban areas compared to rural areas.

However, what was astonishing to see from Figure 4.5 and Figure 4.7 was how both winter and summer night-time LSTs appeared to be higher in urban areas and lower in outlying rural areas.

Further urban-rural gradient analysis in Figure 5.3 showed that the winter night-time gradients had increasingly negative slopes correlating with what was observed in the LST imagery.

Due to the low spatial resolution characterized by this imagery, it was not analysed quantitatively.

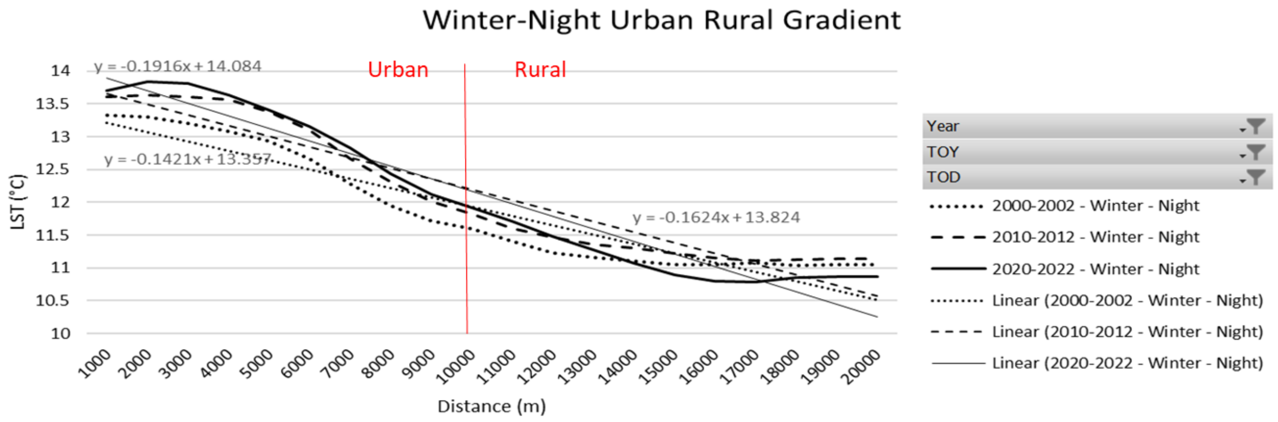

Figure 5.3. MODIS winter night-time UHI urban-rural gradient.

Similar characteristics were observed during the summer night-time as shown in Figure 5.4. The gradients, however, were less steep.

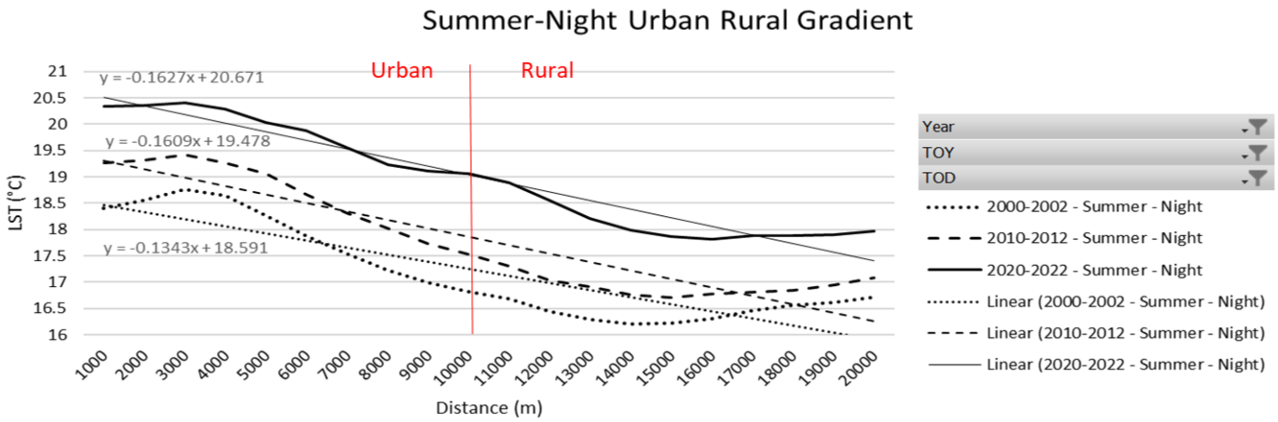

Figure 5.4. MODIS summer night-time UHI urban-rural gradient.

5.2. UHI Intensity Analysis

The results obtained from the Landsat imagery were investigated further to broaden the understanding of the characteristics of the UHI effect. Under this section, a comparison was drawn between the temperatures in rural and urban areas. The findings corroborated with those under the UHI gradient analysis as depicted by Figure 5.5 and Figure 5.6, temperatures were often higher in rural areas, especially in the summer times of the year.

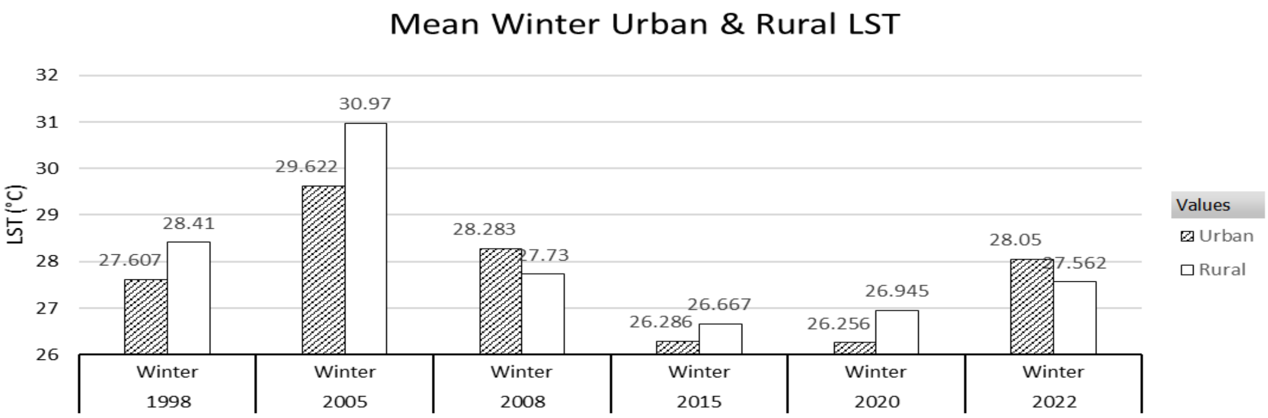

Figure 5.5. Mean winter urban and rural land surface temperatures.

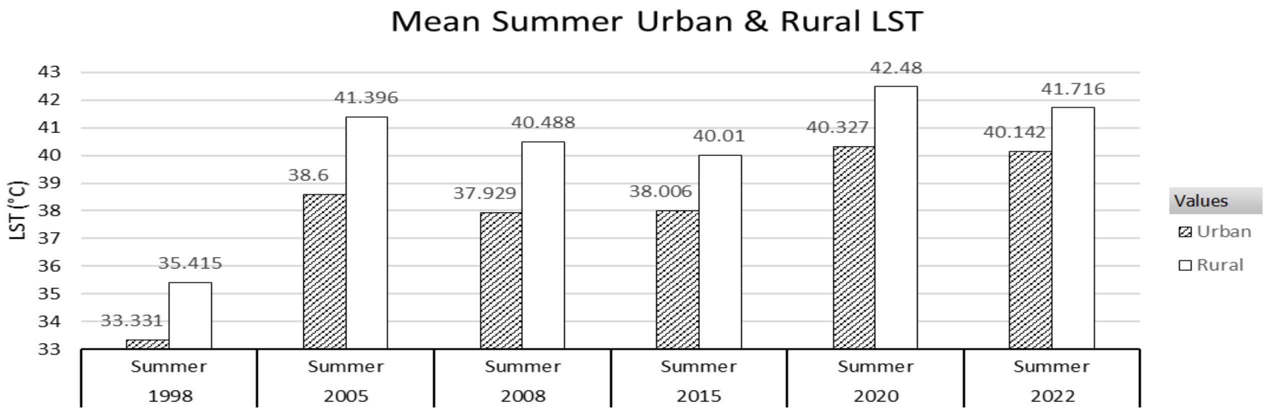

Figure 5.6. Mean summer urban and rural land surface temperatures.

According to Figure 5.7, rural areas were much hotter than urban areas by as much as 1.348℃ in the winter months of 2005. However, in the years 2008 and 2022 hotter LSTs were experienced in urban areas with intensities of up to 0.553℃ and 0.488℃, respectively.

The negative values in the UHI intensities depicted intensities where rural areas were hotter than urban areas.

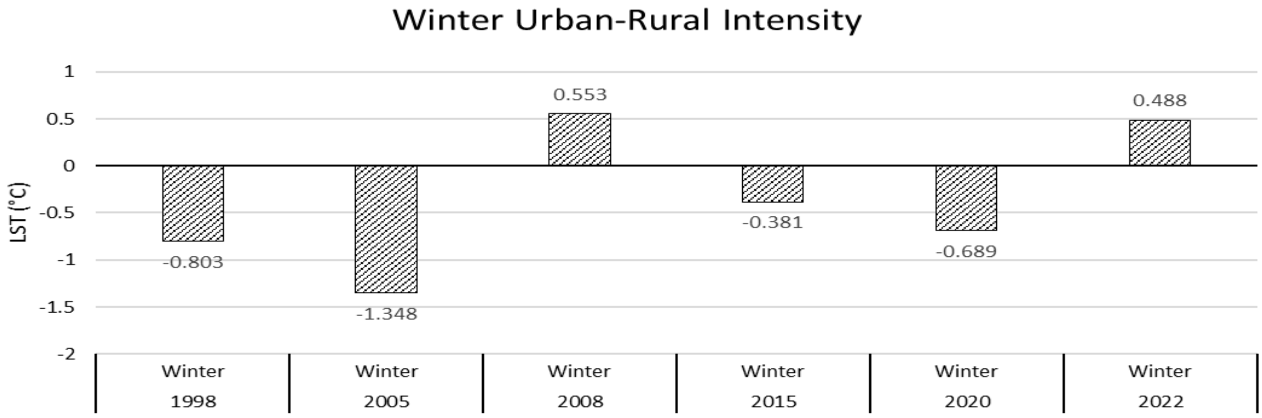

Figure 5.7. Winter urban-rural UHI intensities.

However, rural areas were consistently much hotter than urban areas in the summer throughout the years with UHI intensities ranging from 1.574℃ to as much as 2.796℃ in 2022 and 2005 respectively.

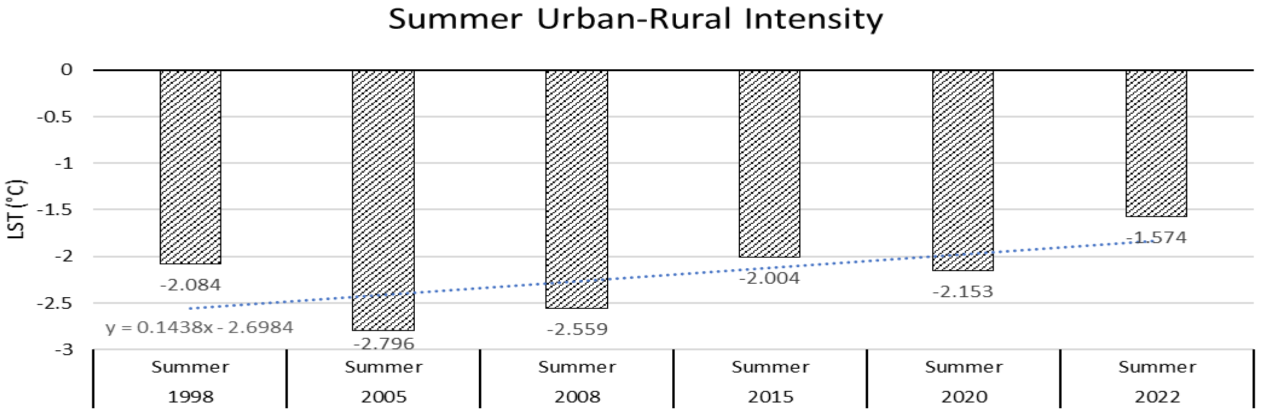

Figure 5.8. Summer urban-rural UHI intensities.

5.3. LST-LULC Relationship

In an attempt to understand why a negative urban-rural gradient and consequently characteristics showing higher temperatures in rural areas were being obtained in the study area, the relationship between LST and its underlying LULC was investigated. This analysis further explained the factors contributing to the UHI effect or lack thereof.

There are several established methodologies for investigating and determining the factors that lead to the UHI effect.

5.3.1. Mean Land Cover Land Surface Temperature

The starting point of the LST-LULC relationship was to analyse the mean temperatures for the various land covers. This analysis was carried out to confirm that there was a variation in LST among the land-use/land-cover classes in the study area.

Figure 5.9 showed that bare land tends to have the highest winter LST followed by impervious surfaces, natural vegetation, cropland, and water with average mean LSTs of about 28.6℃, 28.2℃, 26.3℃, 24.7℃, and 23.4℃, respectively.

In 2005, bare land, impervious surfaces, and natural vegetation all had the highest mean LSTs of 31.4℃, 30.5℃, and 29.7℃, respectively. While cropland and water had their highest temperatures in 2022 and 2008 respectively.

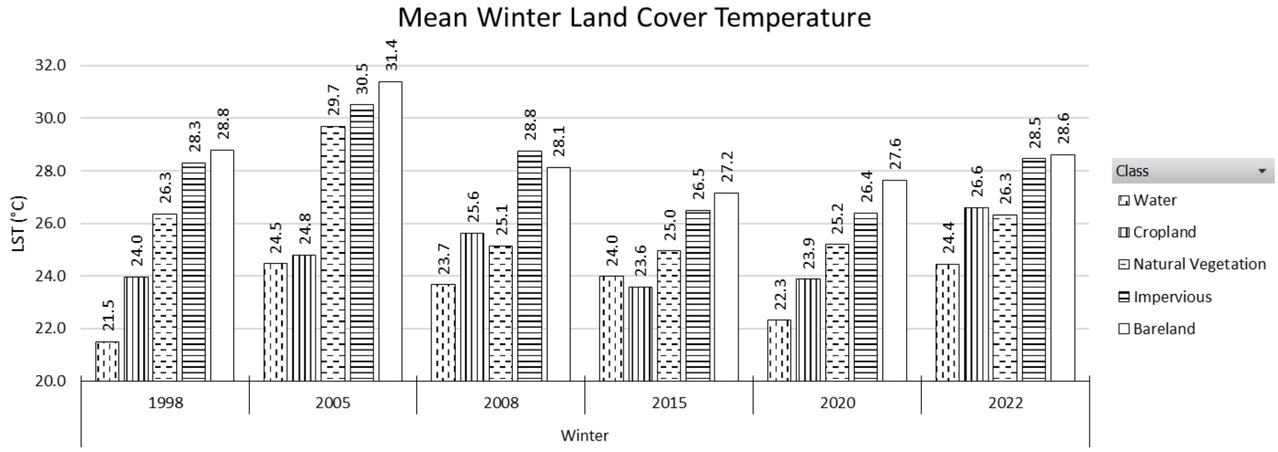

Figure 5.9. Mean winter land cover land surface temperatures.

Similar results were observed during the summer where bare land consistently had the highest mean LST. Average mean LSTs over the years were much higher during the summer with temperatures of 40.6℃, 39.0℃, 38.9℃, 33.5℃ and 29.2℃ for bare land, impervious surfaces, natural vegetation, cropland, and water, respectively. The average mean LST during the summer was significantly higher than during the winter with water in the summer having a higher temperature than that of bare land in the winter by about 0.8℃.

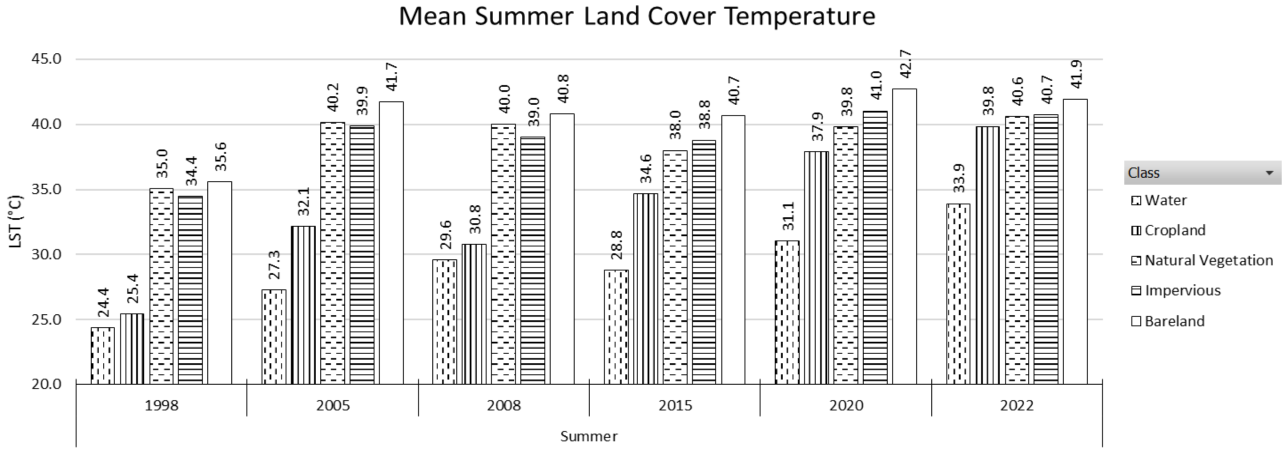

Figure 5.10. Mean summer land cover land surface temperatures.

5.3.2. Relationship along the urban-rural gradient

The relationship between the land cover and LST was also investigated by comparing the LST and the density of the land cover from the urban city centre towards the outlying rural areas.

From the figures in Figure 5.11, it was observed that during the winter, there was a close relationship between LST and the density of bare land, impervious surface, and vegetation (cropland and managed vegetation). As the density of bare land increased, the LST increased as well. The same was observed about impervious surfaces, especially in 2008 as shown in Figure 5.11 (b), between 2000m and 8000m from the city centre, where the LST increased even with a reduction in the density of bare land.

The opposite relationship between LST and vegetation could also be seen during the winter period when vegetation cover had its highest density compared to the summer. The LST decreased as the density of vegetation increased towards the outlying rural areas.

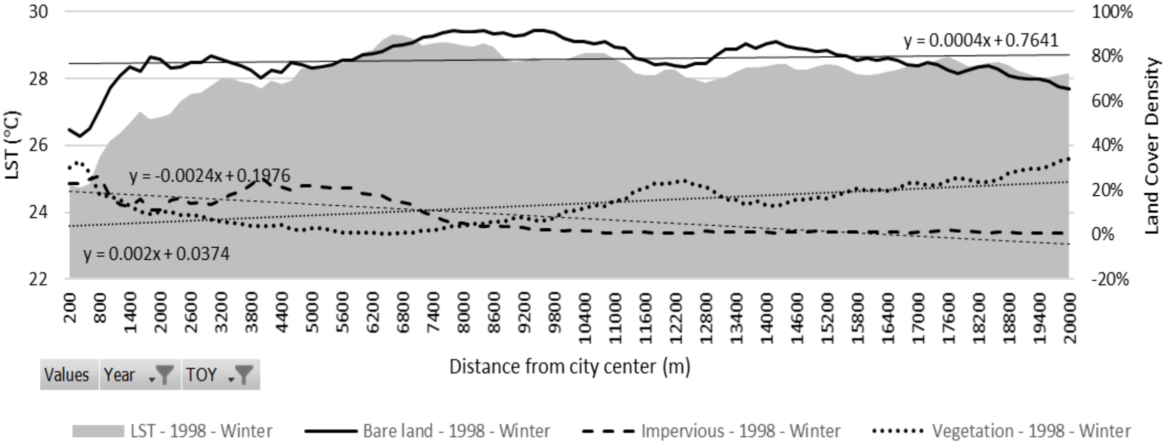

(a)

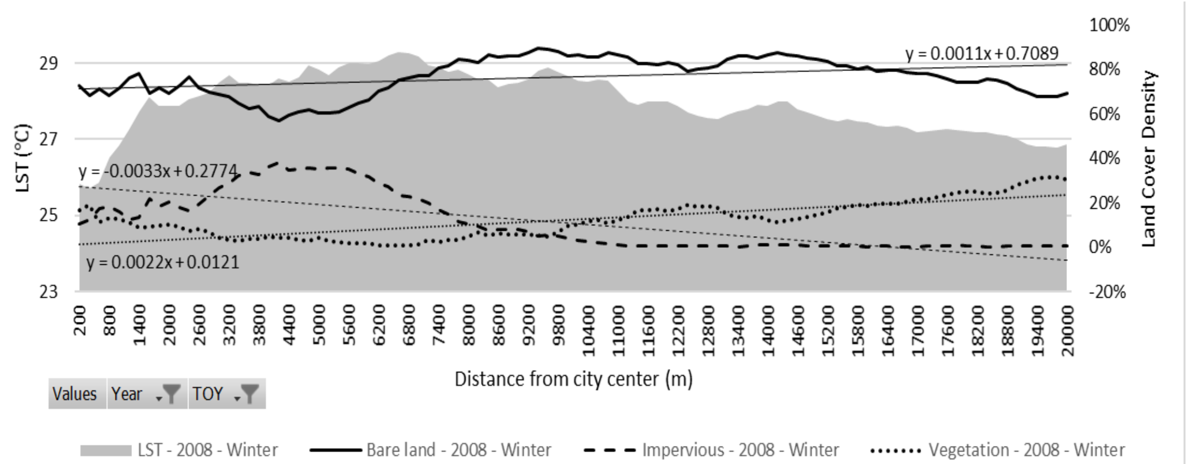

(b)

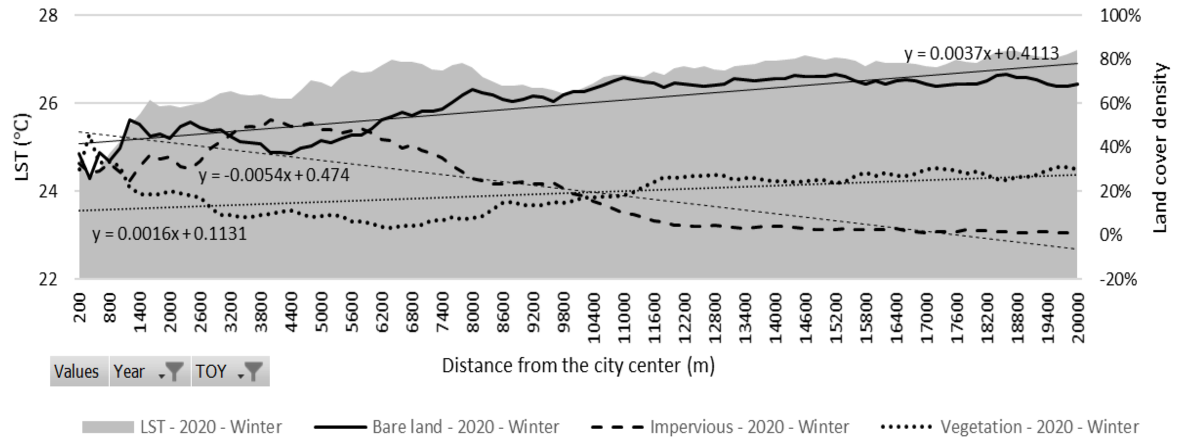

(c)

Figure 5.11. Relationships between the inter LST and bare land, impervious surfaces, and vegetation along the urban–rural gradient in (a) 1998, (b) 2008, and (c) 2020.

The summer period also showed similar relationships between these land covers and the LST. The relationship between the LST was difficult to observe as the density of vegetation was much less for this time of the year. A much closer relationship, however, was observed between LST and the density of bare land. This observation was most recognizable in 2020 as seen in Figure 5.12 (c).

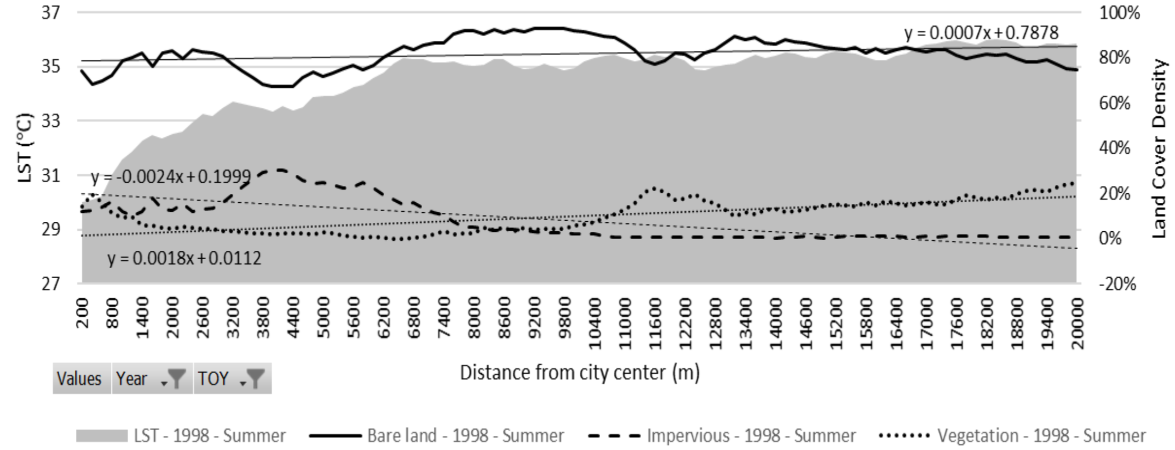

(a)

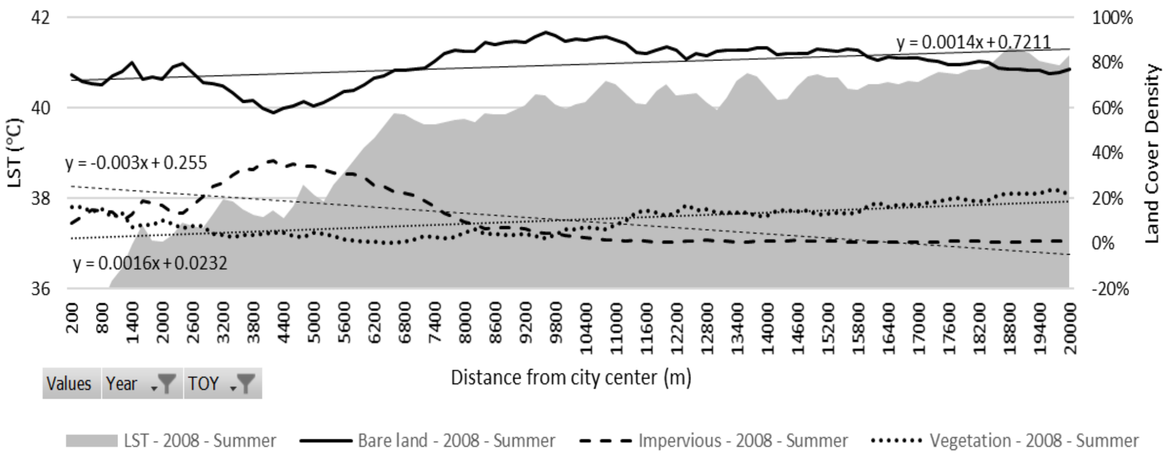

(b)

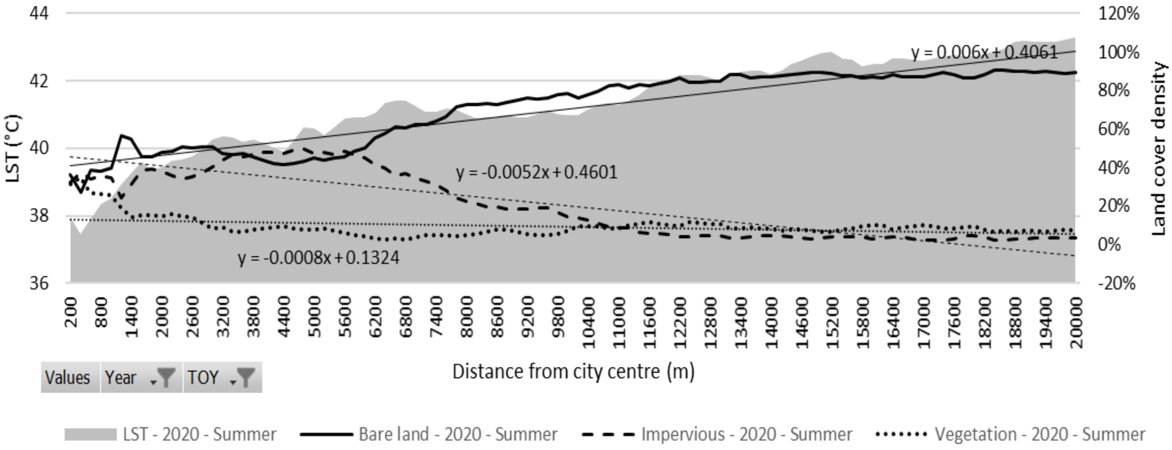

(c)

Figure 5.12. Relationships between the summer LST and bare land, impervious surfaces, and vegetation along the urban-rural gradient for (a) 1998, (b) 2008, and (c) 2020.

Overall, the density of impervious surfaces was generally reducing along the urban-rural gradient as shown by the trendlines' negative slope. On the other hand, the densities of bare land and vegetation were both increasing along the urban-rural gradient. Howbeit, the density bare land was much greater than that of vegetation.

5.3.3. Index-Based Approach

In this analysis, the relationship between land cover and the LST was investigated using the Normalized Difference Vegetation Index (NDVI). Correlation analysis was also conducted using Pearson's correlation coefficient (R), and coefficient of determination (R^2).

The results of Figure 5.13 show a strong negative reducing correlation between NDVI and LST, especially in the winter with R values of -0.6997, -0.5628, and -0.4468 in 1998, 2008, and 2020, respectively. The corresponding R^2 found were 0.4896, 0.3228, and 0.1996, which meant that 49%, 32%, and 20% of the variations in LST were explained by NDVI in 1998, 2008, and 2020, respectively.

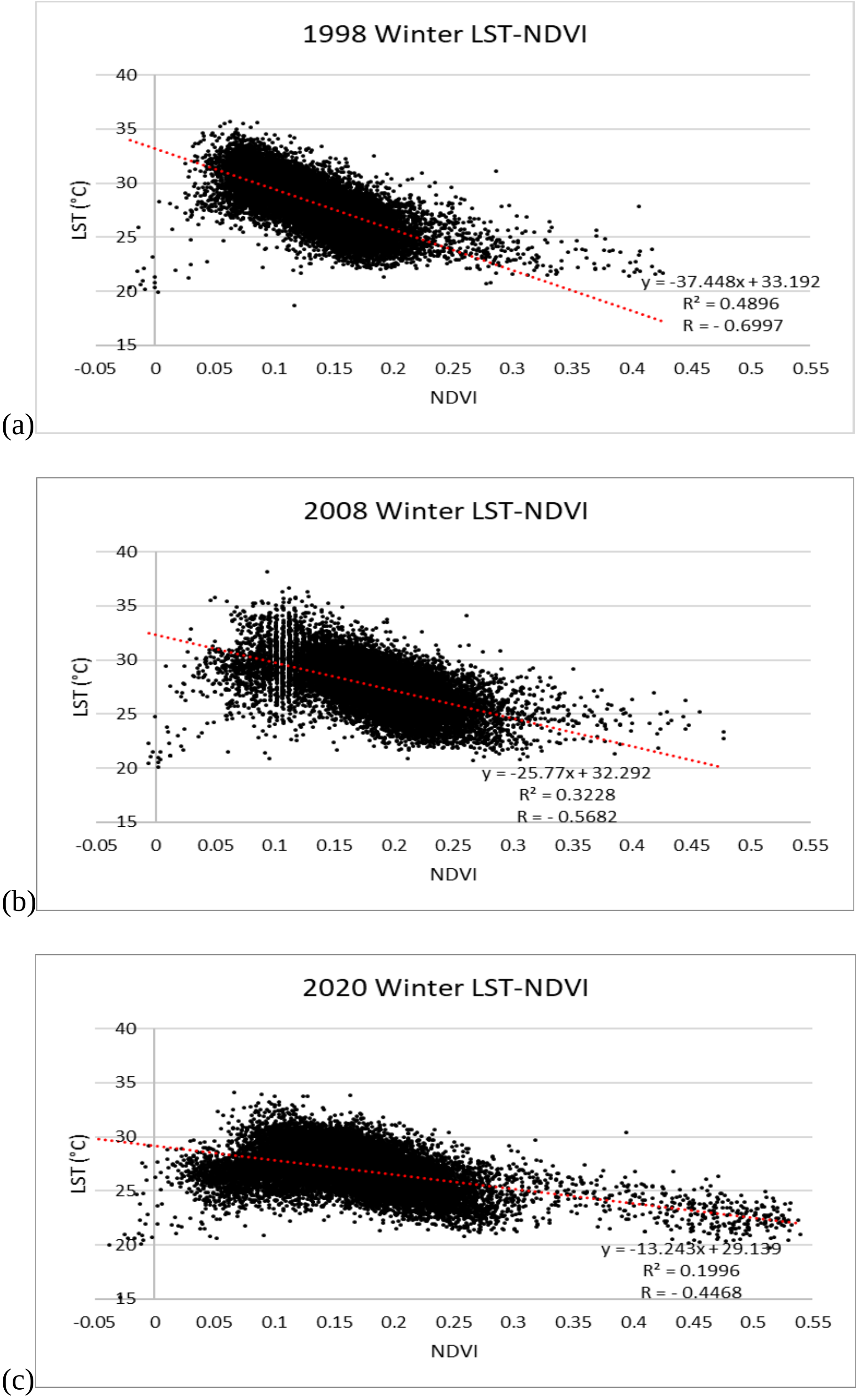

Figure 5.13. Relationship between winter LST and NVDI for (a) 1998, (b) 2008, and (c) 2020.

The results in Figure 5.14 showed a relatively less strong negative correlation between NDVI and LST during the summer. This was observed by the R values of -0.6339, -0.6073, and -0.3415 in 1998, 2008, and 2020, respectively. R^2 values of 0.4018, 0.3688, and 0.1166, which showed that 40%, 37%, and 11% of the variations in LST were explained by NDVI in 1998, 2008, and 2020, respectively.This therefore meant that the lower the NDVI, the higher the LST, and vice versa.

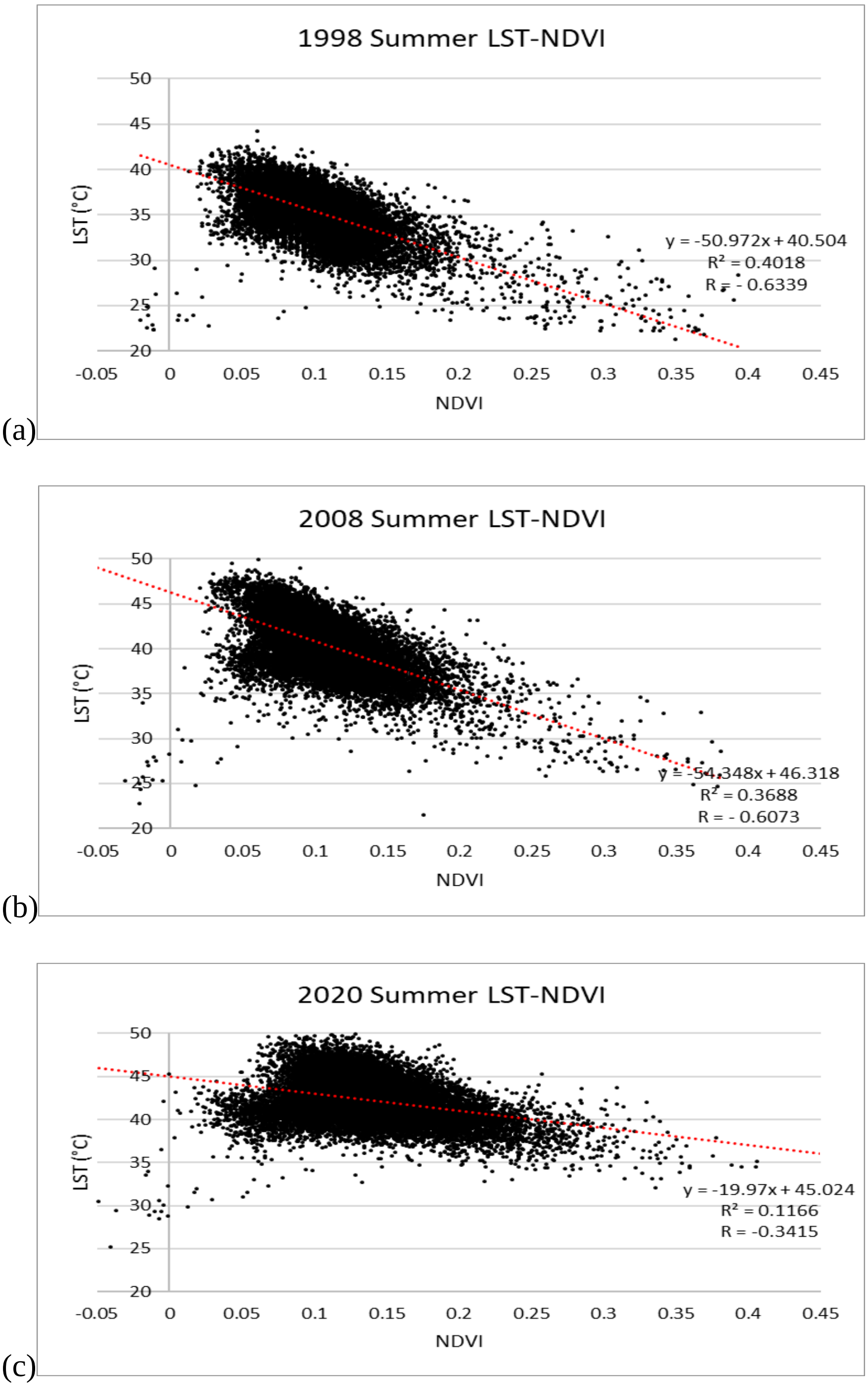

Figure 5.14. Relationship between summer LST and NVDI for (a) 1998, (b) 2008, and (c) 2020.

5.4. LST Trends

The best way to understand present phenomena and how they are likely to be in the future is by looking at their characteristics in the past. In this regard, this section sought to explore the behaviour of LST and the UHI effect over the past 25 years.

5.4.1. UHI Intensity Time Series

Time series analysis of urban and rural LSTs showed fluctuation during the winter times of the year. Figure 5.5 in Section 5.2 showed urban LSTs of 27.61℃, 29.62℃, 28.28℃, 26.29℃, and 28.05℃, and rural LSTs of 28.41℃, 30.97℃, 27.73℃, 26.67℃, 26.95℃, and 27.56℃ for the years 1998, 2005, 2008, 2015, 2020 and 2022, respectively.

This resulted in fluctuating winter intensities of -0.803℃, 1.348℃, 0.553℃, -0.381℃, -0.689℃, and 0.488℃ in 1998, 2005, 2008, 2015, 2020 and 2022, respectively. Fluctuations in these intensities made it difficult to establish any trends for this time of the year.

The summer times of the year however showed increasingly less negative UHI intensities as seen in Figure 5.8. This was because temperatures in urban areas were increasing at a much faster rate over the years compared to rural areas. This was seen in Figure 5.15 where the trendline slope of urban LSTs over the years was higher (+1.123 slope) compared to that of rural areas (+0.979 slope).

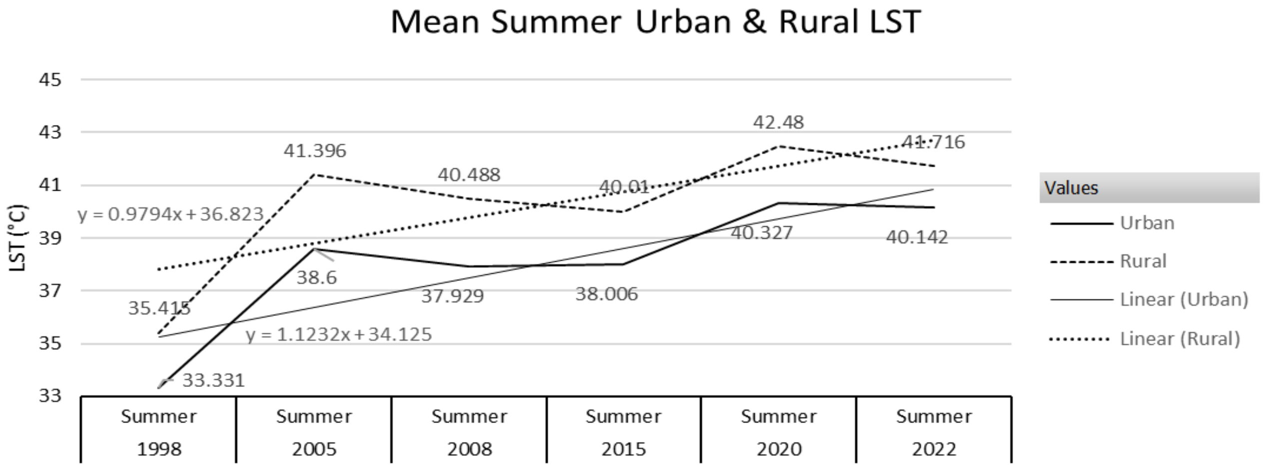

Figure 5.15. Time series for summer winter urban and rural LST.

5.4.2. Lusaka LST Time Series

Finally, a time series analysis of the average LST in Lusaka city alone was carried out to have an understanding of how overall land surface temperatures were varying over the last 25 years.

In Figure 5.18, the winter time series showed a reducing trend in land surface temperatures from 1998 to 2022.

In the summer however, which is the most significant time of the year due to its much higher land surface temperatures, showed an increasing trend as seen by the positive gradient of the simple linear regression line. In 1998, the average LST was 34.41℃ which was comparatively lower that 39.91℃, 38.99℃, 38.37℃, 40.64℃, and 40.41℃ in 2005, 2008, 2015, 2020, and 2022 respectively. This meant that temperatures increased by as much as 4.58℃ between 1998 and 2008, 6.23℃ between 1998 and 2020, and 6.0℃ between 1998 and 2022.

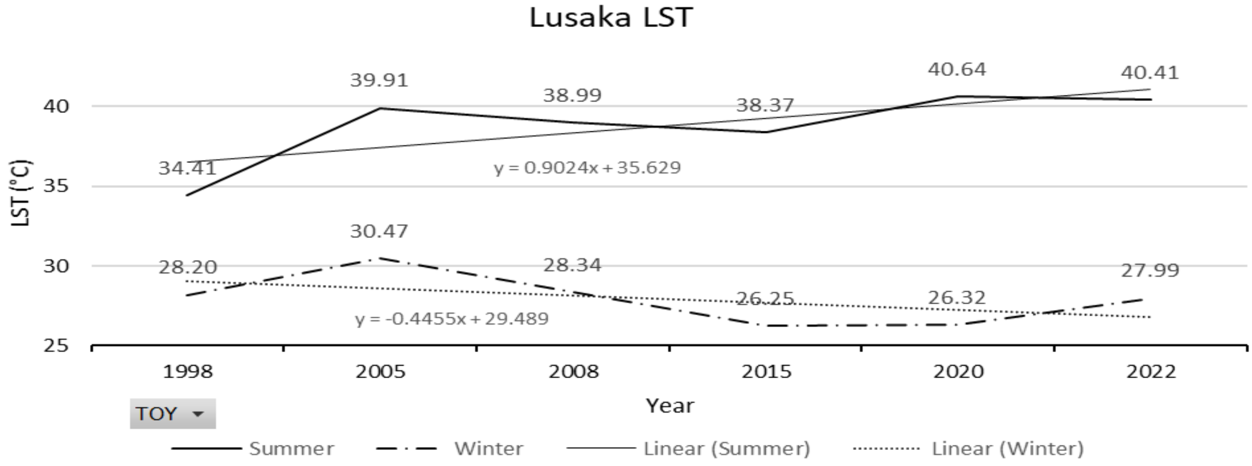

Figure 5.16. Time series for the mean LST in Lusaka.

5.5. Heat Vulnerability Indices

To wrap up the analysis, this research also investigated the varying degrees of susceptibility of residents in particular areas of Lusaka to instances of extreme heat in the previous year (2022). It considered factors that increase exposure to extreme heat such as land surface temperatures, and the amount of vegetation cover, impervious surfaces, and bare land.

The varying exposures of different neighbourhoods to land surface temperatures are shown in Figure 5.17 (a). From this figure, was seen that some areas that were exposed or experienced the highest LSTs were Chilenje, Lilayi, Kaunda Square, Chibolya, etc, with HVI scores of 5. On the other hand, some of the neighbourhoods that had the least exposure to high LSTs with HVI scores of 1 were Kabulonga, Cathedral Hill, Handsworth, Olympia, etc.

Figure 5.17 (b) displayed the susceptibility to extreme heat with respect to vegetation cover. It was observed in the previous sections that vegetation has in inverse relationship with LST. Therefore, areas with higher vegetation had lower HVI scores illustrating lower exposure to extreme heat. It was seen from this figure that areas with HVI scores of 2 such as Roma, State lodge, Twin Palm, etc had lower exposure compared to Misisi, Bauleni, Kanyama, etc that had the highest exposure with HVI scores of 5-6 due to lack of vegetation cover.

The other factor that could increase exposure to extreme heat was the amount of impervious surfaces in the area. Figure 5.17 (c) showed that areas such as Misisi, Chibolya, Chinka, Industrial Area, etc were much more susceptible to extreme heat with HVI scores of 5-6, compared to areas such as Leopards Hill, Lilayi, Twin Palm, etc that had HVI scores of 2 based on the amount of impervious surfaces they contained. This can be seen in the land use map in Figure 4.9(c).

The last factor analysed was of course bare land which also increased the vulnerability of areas to extreme heat. Areas such as John Laing, Chibolya, Chinka, Misisi, etc with HVI scores of 1 had less vulnerability due to bare land. On the other hand, areas with HVI scores up to 5 such as Makeni Bonaventure, Linda, Ngwerere, had higher vulnerability due to this facto as show in Figure 6.17 (d)

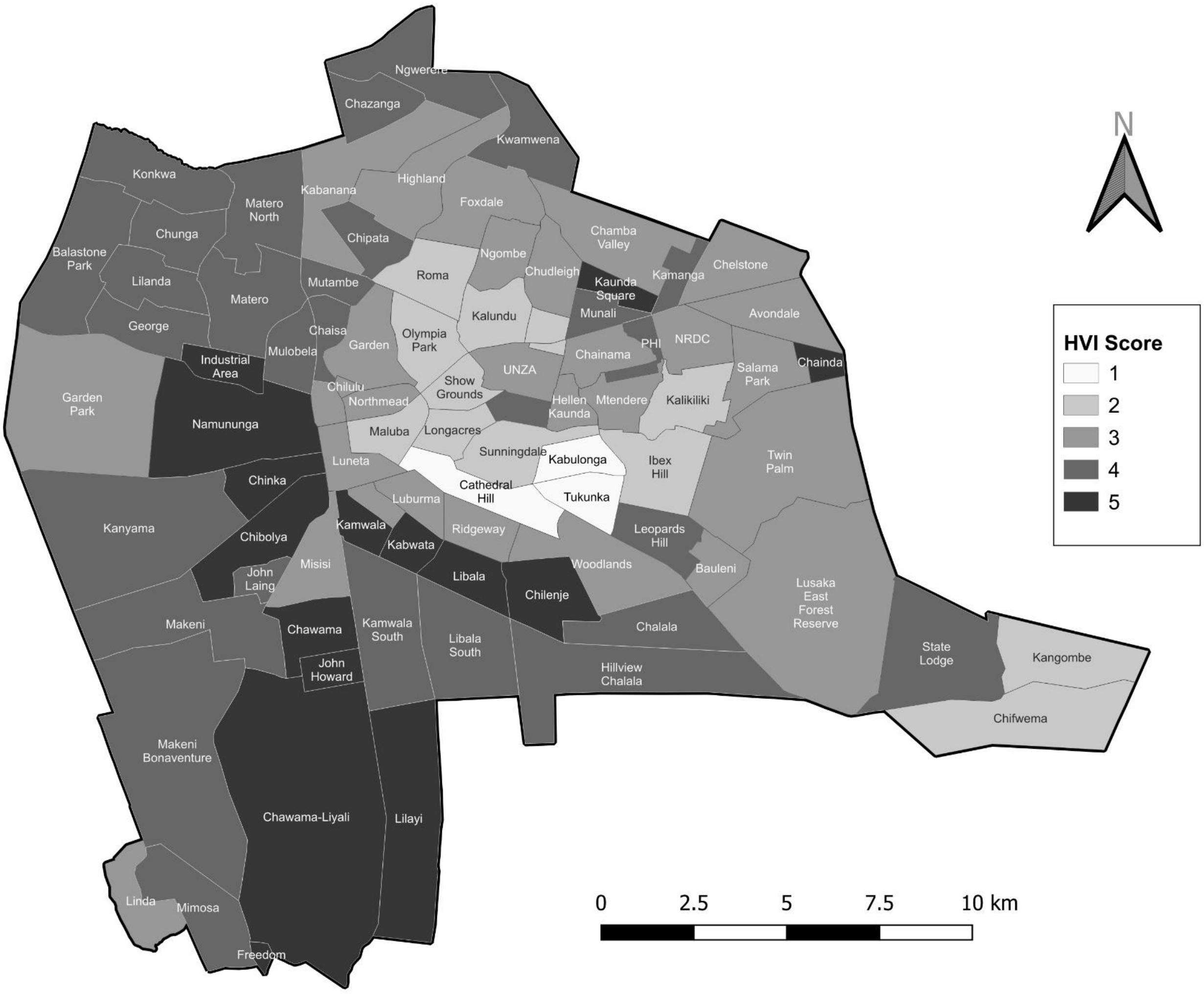
HVI Score
1
2
3
4
5
N
0
2.5
5
7.5
10 km
Ngwerere
Chazanga
Kwamwena
Konkwa
Matero North
Kabanana
Highland
Foxdale
Chamba Valley
Chunga
Balastone Park
Chipata
Ngombe
Kamanga
Chelstone
Lilanda
Matero
Mutambe
Roma
Chudleigh
Kaunda Square
Kalundu
Munali
Avondale
George
Chaisa
Garden
Olympia Park
PHI
NRDC
Chainama
Salama Park
Chainda
Industrial Area
Mulobela
Chilulu
Show Grounds
UNZA
Garden Park
Northmead
Hellen Kaunda
Mtendere
Kalikiliki
Namununga
Maluba
Longacres
Sunningdale
Kabulonga
Ibex Hill
Twin Palm
Luneta
Cathedral Hill
Chinka
Luburma
Tukunka
Kanyama
Kamwala
Ridgeway
Leopards Hill
Chibolya
Kabwata
Woodlands
Misisi
Bauleni
John Laing
Libala
Chilenje
Lusaka East Forest Reserve
Makeni
Chawama
Kamwala South
Chalala
Libala South
State Lodge
John Howard
Hillview Chalala
Kangombe
Chifwema
Makeni Bonaventure
Chawama-Liyali
Lilayi
Linda
Mimosa
Freedom

(a)

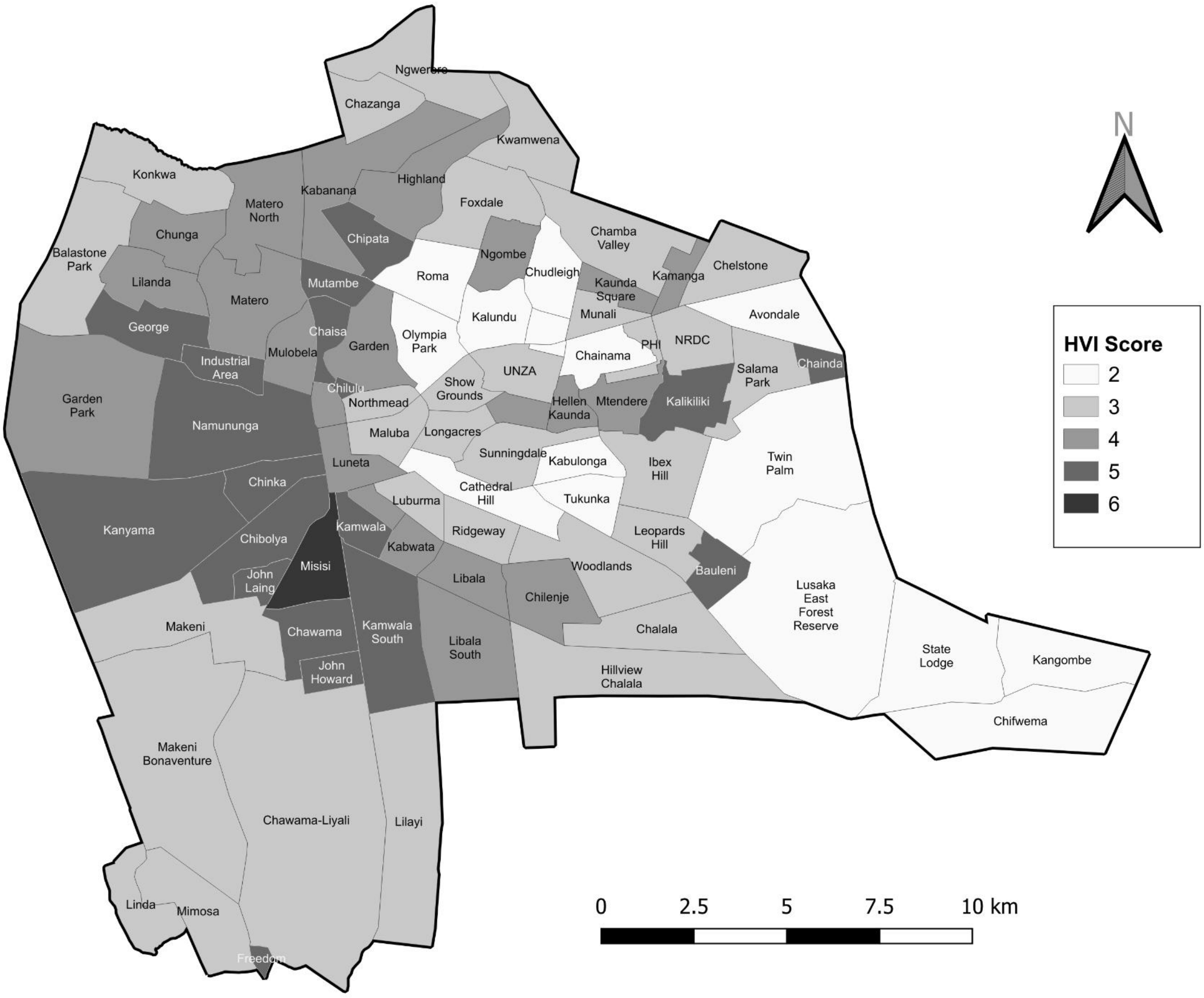
Ngwerere
Chazanga
Kwamwena
Konkwa
Kabanana
Highland
Matero North
Foxdale
Chunga
Chipata
Chamba Valley
Balastone Park
Roma
Ngombe
Chudleigh
Chelstone
Lilanda
Mutambe
Kaunda Square
Kamanga
Matero
Kalundu
Munali
Avondale
George
Chaisa
Olympia Park
Chainama
PHI
NRDC
Mulobela
Garden
Industrial Area
UNZA
Salama Park
Chainda
Chilulu
Show Grounds
Garden Park
Northmead
Hellen Kaunda
Mtendere
Kalikiliki
Namununga
Maluba
Longacres
Sunningdale
Kabulonga
Twin Palm
Luneta
Ibex Hill
Chinka
Cathedral Hill
Luburma
Tukunka
Kanyama
Kamwala
Ridgeway
Leopards Hill
Chibolya
Kabwata
Woodlands
Misisi
Bauleni
John Laing
Libala
Lusaka East Forest Reserve
Chilenje
Makeni
Chawama
Kamwala South
Chalala
Libala South
State Lodge
John Howard
Kangombe
Hillview Chalala
Chifwema
Makeni Bonaventure
Chawama-Liyali
Lilayi
Linda
Mimosa
Freedom
N
HVI Score
2
3
4
5
6
0
2.5
5
7.5
10 km

(b)

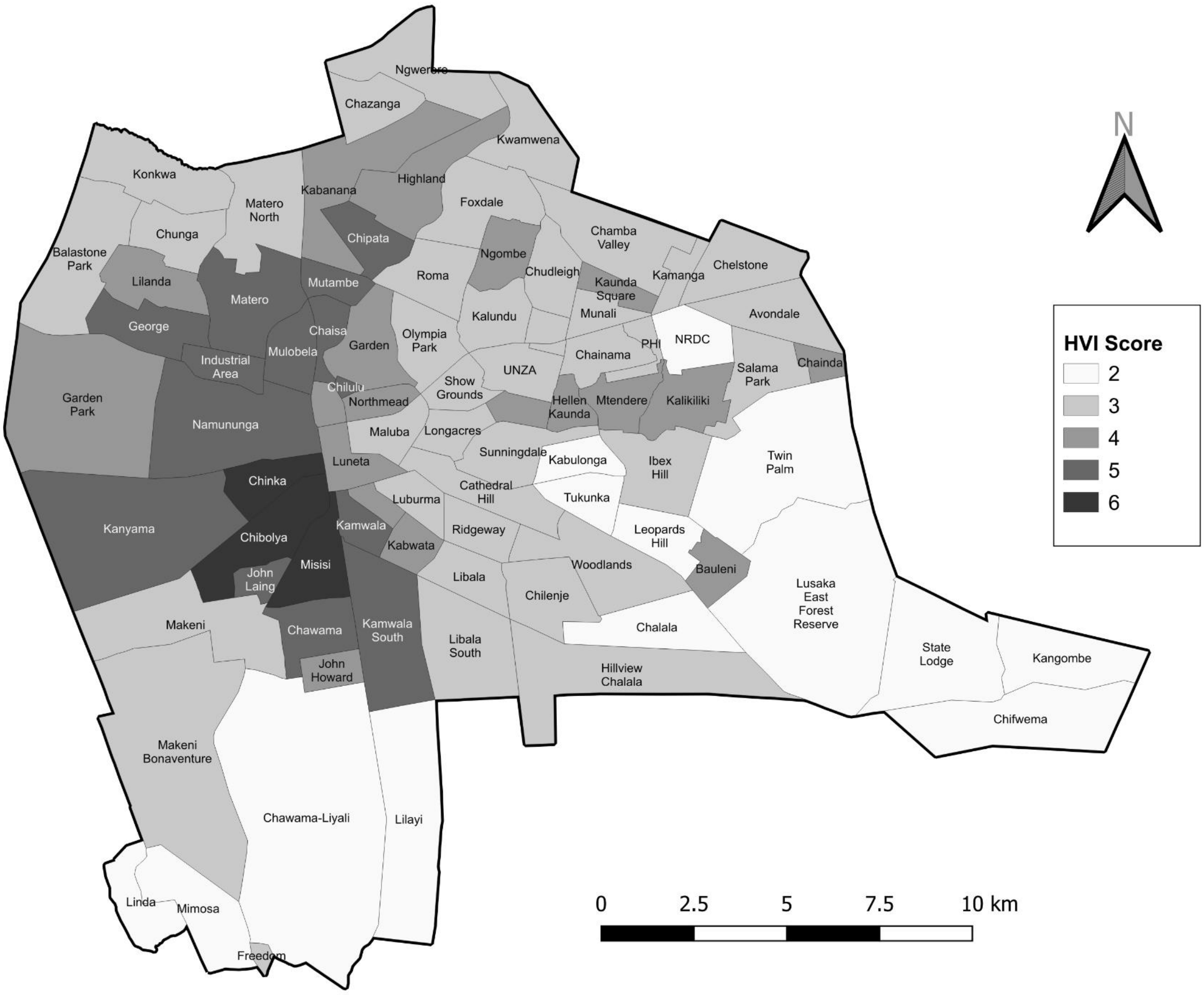
N
HVI Score
2
3
4
5
6
0
2.5
5
7.5
10 km
Ngwerere
Chazanga
Kwamwena
Konkwa
Kabanana
Highland
Matero North
Foxdale
Chunga
Chipata
Chamba Valley
Balastone Park
Ngombe
Chelstone
Lilanda
Matero
Mutambe
Roma
Chudleigh
Kaunda Square
Kamanga
George
Chaisa
Kalundu
Munali
Avondale
Industrial Area
Mulobela
Garden
Olympia Park
Chainama
PHI
NRDC
Garden Park
Chilulu
Show Grounds
UNZA
Salama Park
Chainda
Northmead
Hellen Kaunda
Mtendere
Kalikiliki
Namununga
Maluba
Longacres
Luneta
Sunningdale
Kabulonga
Ibex Hill
Twin Palm
Chinka
Cathedral Hill
Luburma
Tukunka
Kanyama
Kamwala
Ridgeway
Leopards Hill
Chibolya
Kabwata
Woodlands
Misisi
Bauleni
John Laing
Libala
Lusaka East Forest Reserve
Chilenje
Makeni
Kamwala South
Chawama
Chalala
Libala South
John Howard
State Lodge
Kangombe
Hillview Chalala
Chifwema
Makeni Bonaventure
Chawama-Liyali
Lilayi
Linda
Mimosa
Freedom

(c)

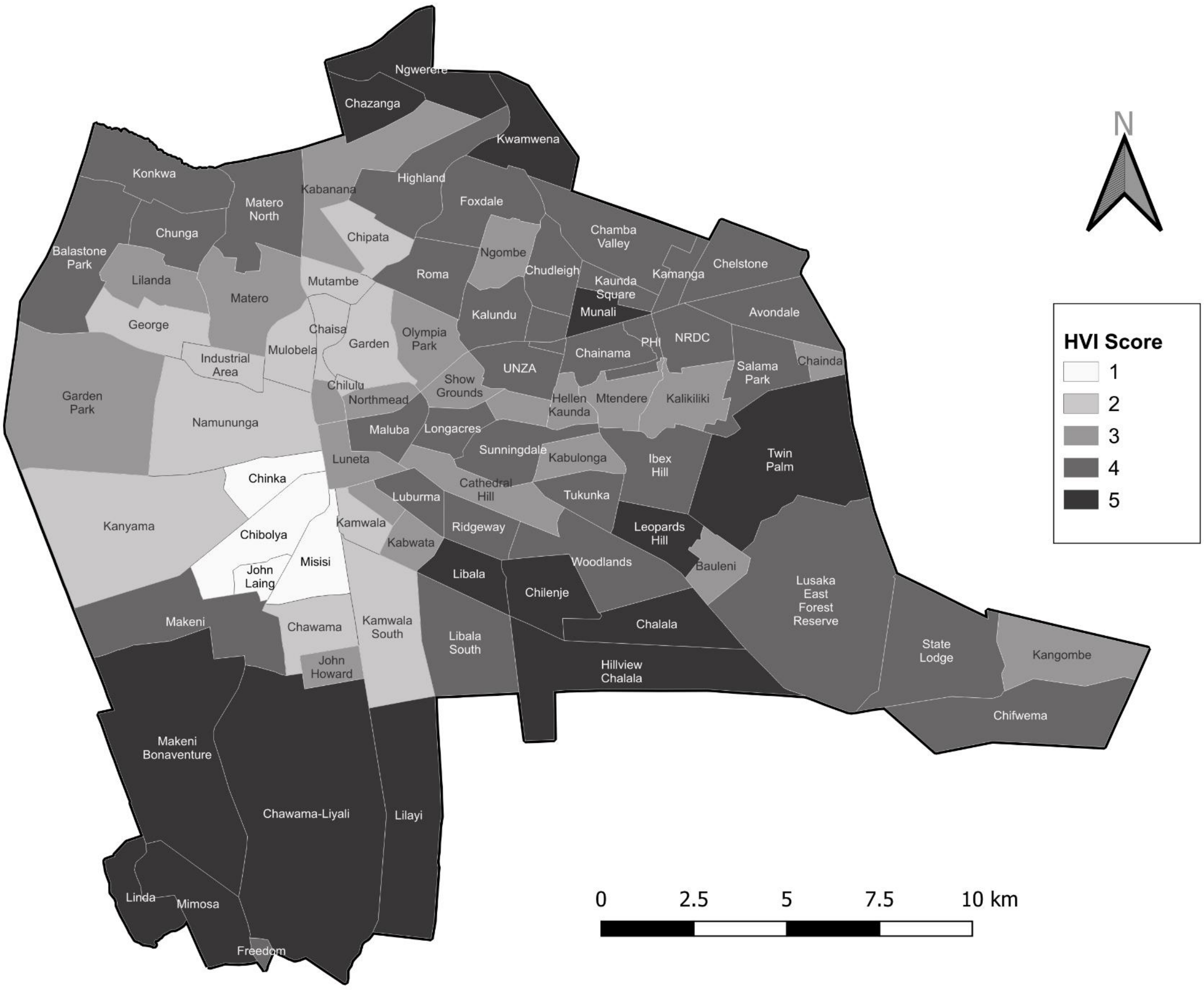

(d)

Figure 5.17. Lusaka neighbourhood HVIs for (a) LST, (b) vegetation cover, (c) impervious surfaces, and (d) bare land.

The analysis was concluded by amalgamating the HVI scores of the different HVI exposure factors into one HVI map. Figure 5.18 showed that areas with the highest overall exposure were Chibolya, Chawama, Kamwala, Kaunda Square, etc with overall HVI scores of 17. Kabulonga and Tukunta, Cathedral Hill, Kangombe had the lowest HVI scores of 8 and 9 respectively.

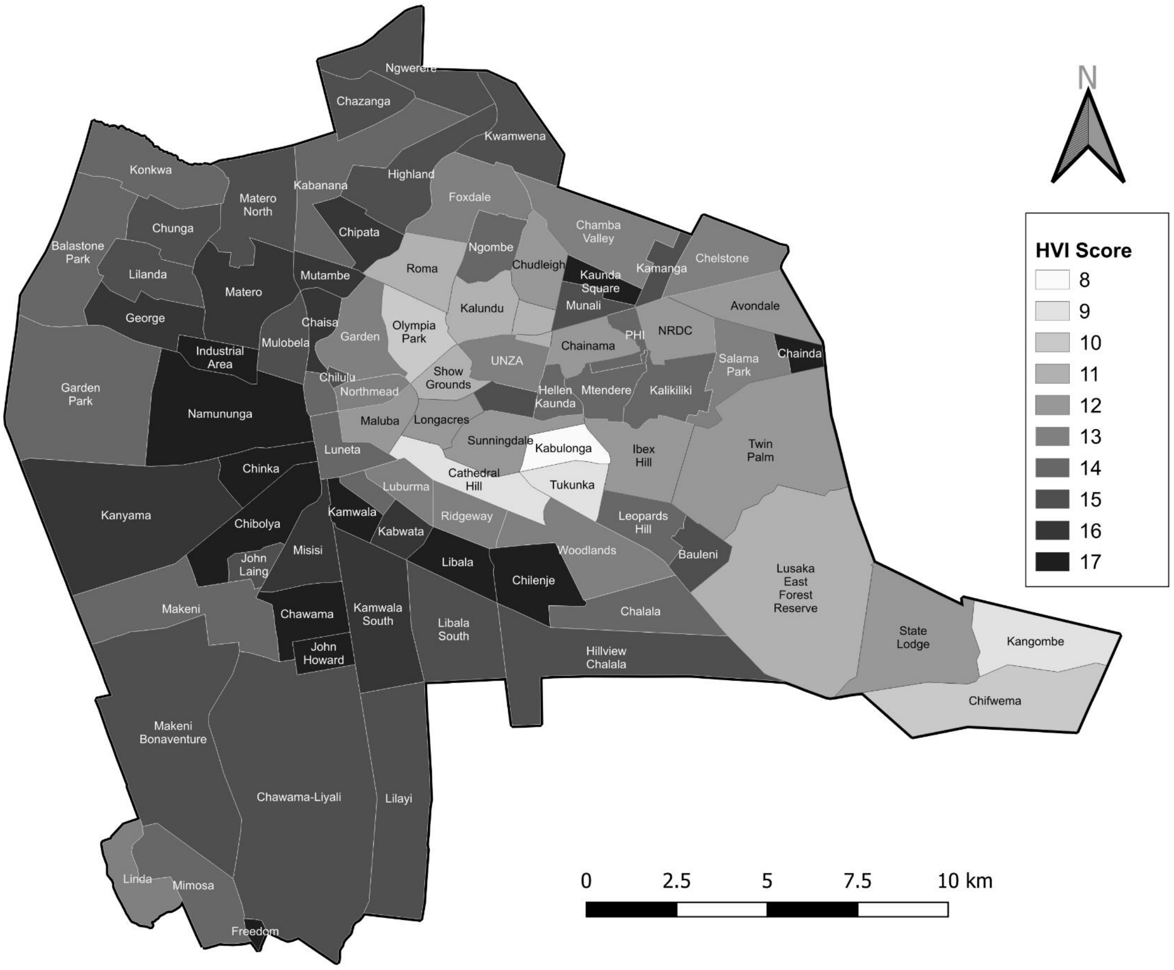

Figure 5.18. Lusaka neighbourhood overall HVIs.

More information on the HVI scores of neighbourhoods within Lusaka city concerning each of the factors can be found in Appendix E.

CHAPTER: 6

DISCUSSION

To discuss the characteristics of the UHI in the city of Lusaka, it was necessary, to begin with understanding the influences of the land cover within and around the city. Such an understanding gave more insight as to why these characteristics occurred the way they did.

6.1. Influence of Land Cover on Land Surface Temperature

In this study, the relationship between LST and land cover was investigated. The results and analysis found that bare land had the highest land surface temperatures both during winter and summer.

Analysis derived from Section 5.3.1 showed an average winter temperature difference of up to 0.469℃ between bare land and impervious surfaces, which had the second-highest LST. This difference was even much higher during the summer with average temperatures as high as 1.594℃ over the study period. This was consistent with results found by (Haylemariyam, 2018).

Impervious surfaces on the other hand had temperatures higher than both natural vegetation and cropland. The average temperature difference when compared to natural vegetation was 0.049℃ in the summer and as high as 1.882℃ during the winter. This was probably because winter occurred at the end of the rainy season when natural vegetation had higher density compared to the summer when tree canopies were less dense thus exposing more bare land and increasing the surface temperatures. When compared to cropland, the average temperature difference was 5.523℃ in the summer and 3.146℃ during the winter. This showed that cropland had higher cooling effects compared to natural vegetation, most like due to its higher density occurrence which exposes less bare land and higher moisture content as a result of irrigation. Overall, it was noted that vegetation cover played a vital role in lowering LST by providing shade and cooling of the surroundings through ground concealment and evapotranspiration (Ogunjobi et al., 2018, John et al., 2020).

Finally, when compared to cropland, which had shown cooling effects, water showed even higher cooling effects. the average temperature difference was 4.289℃ in the summer and 1.352℃ during the winter. This meant that water also has the potential to have a cooling effect on LST through process water evaporation (Wang et al., 2020).

Therefore, impervious surface, natural vegetation, cropland, and water were 0.469℃, 2.378℃, 3.615℃ and 4.967℃ cooler than bare land during the winter and 1.594℃, 1.643℃, 7.117℃ and 11.406℃ cooler during the summer, respectively

The influence of land cover on LST analysed in Section 5.3.2 also showed a close relationship between bare land and higher LST. Both Figures 5.11 and 5.12 showed very similar trajectories of the line plots representing bare land and LST, especially during the summer when the land cover density of bare land was much higher. In addition, the land cover density of bare land was consistently over 60% in the winter and about 80% in the summer. This meant bare land was two times denser than vegetation and impervious cover, and up to four times during the summer, especially in rural areas. As a result, the influence of bare land on the LST was much more discernible than impervious surfaces and vegetation cover on the urban-rural gradient.

Finally, Section 3.3.3 which carried out an index-based approach to the analysis of the influence of LULC on LST, revealed a strong correlation between LST and NDVI. To add more context and explain the results in the analysis, an explanation was drawn from Remote Sensing Phenology (2018) which explained results corresponding to NDVI values, stating that:

> ‘Areas of barren rock, sand, or snow usually show very low NDVI values (for example, 0.1 or less). Sparse vegetation such as shrubs and grasslands or senescing crops may result in moderate NDVI values (approximately 0.2 to 0.5). High NDVI values (approximately 0.6 to 0.9) correspond to dense vegetation such as that found in temperate and tropical forests or crops at their peak growth stage.’

The winter NDVI values in Figure 5.13 ranged from 0 to approximately 0.45. In this context, this meant that the land cover in the study area was mostly barren rock (land), and grasslands or shrubs. Therefore, this showed that the NDVI values that were less than 0.2 and comprised of higher land surface temperatures (~30℃) were that of bare land while the NDVI values that were greater than 0.2 and comprised of lower land surface temperatures (~25℃) were that of vegetation.

Similar results were obtained during the summer with NDVI values ranging from 0 to 0.35 as shown in Figure 5.14. The NDVI range was much smaller due to the reduced vegetation during the summer. Low NDVI values had much higher LSTs (~45℃) while the high NDVI values also had much higher LSTs (~35℃), compared to the winter. This analysis therefore corroborated and reiterated what was discussed in the preceding paragraphs.

With the savannah woodland which is comprised of scattered trees that do not form closed canopies, bare land continued to have a significant influence on LST even during winter when vegetation densities were higher.

6.2. Implications of Land Use Land Cover on UHI Characteristics

Analysis carried out in Section 5.1.1, Section 5.2, Section 5.3.2, and Section 5.4.1. spoke to one common fact. Regardless of year or time of the year (summer or winter), daytime land surface temperatures were higher in rural areas compared to urban areas. These results were consistent with the findings of Simwanda et al, (2019) who conducted a similar study of Lusaka using 2016 imagery.

The winter urban-rural gradient in Figure 5.1 showed that although temperatures were higher in rural areas, land surface temperatures in this gradient showed irregular patterns, with peak LSTs occurring about 6 km from the city centre, similar to the findings of Estoque et al., (2017) in Bangkok and Manila. This was most likely due to the irregular land cover pattern comprised of patches of vegetation amid bare land and impervious surfaces.

During the summer, however, the LSTs were gradually increasing much more regularly along the urban-rural gradient and at similar rates over the years as shown in Figure 5.2. The LSTs in this figure were much higher due to it being in the summer.

To explain the winter and summer daytime UHI effect or lack thereof, the influence of land cover in the study area was considered. Figures 4.1 and 4.3 showed that the LULC in rural areas were predominantly bare land which was, established in Section 5.1 and corroborated by Simwanda et al, (2019) stating that:

> ‘the gradual increase in the mean LST in…Lusaka within the defined rural area from the urban-rural cross-point… could be explained based on the land cover in the study areas… the remaining land cover beyond the urban footprint was… mainly characterized by bare lands and abandoned crop fields… [which] could have contributed to the observed higher LST values as bare lands can also elevate surface temperatures’ (p. 15)

The characteristics of the daytime urban-rural gradient led to the characteristics observed with the UHI intensity. The UHI intensity was characterized by negative intensities, as shown in Figure 5.7 and Figure 5.8. This meant that urban areas were cooler than the rural areas by 2.2°C on average during the summer.

Despite summer and winter day-time showing higher LSTs in rural areas, analysis carried out in Section 5.1.2 showed that night-time LSTs were higher in urban areas compared to rural areas by as much as 2.9℃ in the winter and 2.7℃ during the summer. Figures 5.3 and 5.4 in this section showed the relatively steeper gradients as LSTs reduced from the urban to the outlying rural areas. Similar results were obtained by (Lazzarini et al., 2013) who obtained results that showed an inversion of the standard UHI phenomenon during the daytime, where the downtown areas appear colder compared to the suburbs, and observed the standard SUHI during the night with values of downtown LSTs higher than the suburbs.

The type of land cover in the city and surrounding areas also had a major role to play in the opposite effect that was observed during the night. This was most like due to the variations in the thermal effusivity of the LULCs. Arellano & Roca (2023) in their study of the night-time UHI found that asphalt and concrete maintained high radiant temperatures during the night, 5% and 3% higher than the average of all measurements, while bare soil which was hot during the hours of sunlight cooled significantly fast during the night, and vegetated soil (grass) was always cooler. Therefore, the much lower ability of impervious surfaces to release heat compared to other land covers was the reason the night-time UHI effect occurred in Lusaka.

6.3. Trends in Land Surface Temperatures

This research also sought to analyse the trends in the UHI effect over the past 25 years. This was done to gain a general understanding of the behaviour of LST in the past and how it could potentially be projected into the future, provided current trends in the causing factors prevail.

To begin with, Figure 5.7 showed an irregular pattern in the winter UHI intensity over the years. This could have been due to the irregular land cover pattern of varying densities of vegetation in each of the years, especially in rural areas. Higher densities and extents of vegetation cover which would replace/cover bare land in rural areas in certain years meant that winter temperatures in rural areas would lower, thus giving UHI intensities greater than 0℃. This resulted in urban areas being hotter than rural areas in some years.

However, Figure 5.8 showed more regular summer UHI intensities. These intensities were consistently negative showing that urban areas were cooler while rural areas were hotter over the years. Trends in this figure showed that summer UHI has been increasingly less negative over the years. In addition, the trends in the rural and urban mean LST depicted in Figure 5.15 showed that LSTs in both urban and rural areas have been increasing. However, the urban LST is increasing at a much faster rate (slope of 1.1232) compared to the rural LST (slope of 0.9794). What can be deduced from the slopes of the linear regression analysis is that in the future, perhaps approximately 15 years from now, LSTs in urban areas may become higher than those in rural areas. This would ultimately result in the daytime UHI effect in Lusaka.

One possible explanation for this is the encroachment of the extent of urban areas into rural areas over the years. This would have meant that urban areas had more bare land in addition to the impervious surfaces being built up whilst rural areas were simultaneously losing the extents of bare land.

Finally, the mean LST for Lusaka city (or district) with respect to its administrative boundaries was obtained, excluding the outlying rural extents. This analysis, displayed in Figure 5.16, showed that the summer mean LST in Lusaka was increasing over the years. On the other, the winter LST trends were reducing at more than half the rate at which the summer temperatures were increasing.

6.4. Heat Vulnerability Indices

Analysis conducted in Section 5.5 developed a tool to represent overall heat risk which can help identify susceptible regions and sub-populations in cities in the face of heatwaves or extreme heat. Therefore, the imagery used to generate the HVI maps was the most recent summer imagery (2022).

Taking LST as a variable, this tool in Figure 6.17 (a), showed that neighbourhoods in the East of the city, especially those in the South-east were exposed to higher land surface temperatures and consequently had higher LST-HVI scores. These neighbourhoods mostly consisted of high densities of either bare land or impervious surface. The opposite was true about neighbourhoods located in the centre and towards the east of the city.

The next variable considered in the HVI was the amount of vegetation cover. Neighbourhoods with higher densities of vegetation had lower HVI scores as shown in Figure 6.17 (b). These were mostly affluent neighbourhoods established during the colonial time and developed with regard to vegetation cover, as well as those still having natural vegetation as a result of less dense human settlement. The opposite was true about neighbourhoods that lay on the opposite end of the HVI spectrum and consisted of mostly dense human settlements and activities.

Impervious surfaces were also considered as a variable and had a direct relationship with the HVI score. Areas in the city with very dense and rather unplanned human settlements exhibited much higher vulnerability due to heat exposure caused by impervious surfaces as shown in Figure 6.17 (c).

Neighbourhoods with the opposite characteristics had much lower HVI scores with respect to impervious surfaces.

Bare land, which was discovered to be of most significance to LSTs was also considered as a variable. With respect to this variable, neighbourhood with higher scores were mostly those closer to the boundaries of the city and towards the rural areas as seen in Figure 6.17 (d). These neighbourhoods were characterised by sparse human settlements and buildings and vegetation as well, leading to higher exposure to bare land. Neighbourhoods with the lowest bare land HVI scores were those with very dense, unplanned human settlements, therefore exposing less bare land.

Finally, all four HVI exposures analysed were merged into one single HVI index shown in Figure 5.18. HVI scores ranged from neighbourhoods characterised by sparse settlement and impervious surfaces, and high vegetation cover, to those with very low vegetation cover coupled with either very highly dense impervious surfaces or very spare impervious cover that exposes bare land.

It is therefore these areas with high HVI scores that most mitigation efforts should be directed to.

CHAPTER: 7

CONCLUSION

The assessment of land surface temperature using remote sensing and GIS carried out in this research unravelled a wealth of knowledge on the characteristics and contributing factors of the Urban Heat Island effect in Lusaka. In addition to this, an understanding was acquired of its trends and which particular areas of the city it affects.

It is from this knowledge that it was deduced that the UHI effect only existed in the city during the night times of both the winter and summer times of the year, with the effect being greater during the summer. However, that is not to say that daytime land surface temperatures are of no concern. This is because, despite temperatures in the urban city being lower than in outlying rural areas, they are still higher during the day compared to the night-time. Additionally, UHI intensity trends show that urban LSTs may indeed become higher than rural LSTs in the future.

Trends have also shown that over the years, the night-time UHI effect has become more widespread with higher land surface temperatures. The summer and winter daytime land surface temperatures in the city have also been increasing over the years as well with mean LSTs of 40.4℃ and maximum LSTs of up to 50℃ in 2022.

However, with regard to contributing factors, bare land was the greatest contributing factor to higher land surface temperatures compared to impervious surfaces. Natural vegetation on the other hand had observable cooling effects but not as significant as cropland and water.

This study also revealed that people living in neighbourhoods with higher densities of bare land and/or impervious surfaces coupled with low vegetation cover would be more susceptible to instances of extreme heat due to higher exposure.

It is therefore recommended local mitigation efforts should seek to encourage the growing of vegetation (e.g., grass, shrubs, and trees), in already built-up areas, especially those highlighted in the HVI map.

In addition, even as the city continues to expand within and beyond the confines of its administrative boundaries, urban planners, policymakers, and other various stakeholders should while attempting to both control the unplanned and carry out planned development, consider the dispersing built-up areas (buildings) and paved surfaces (roads and parking lots). Furthermore, they should encourage if not make it mandatory for citizens and estate developers to maintain and add to existing vegetation (grass, shrubs, and trees) cover.

This research therefore, provides useful information that can help provide better urban and rural environmental conditions and help Lusaka and other cities within Zambia ultimately realize the United Nations' third and eleventh sustainable development goals which are to attain good health and well-being, and sustainable cities and communities, respectively.

RECOMMENDATIONS

In terms of future research, investigating other contributing factors to the UHI effect besides land cover such as urban geometries, will also give more understanding of this phenomenon within the city. In addition, investigating the effects of land surface temperatures and the UHI effect on different aspects of the city known to be affected by high urban temperatures such as energy consumption, air pollution, and the health of humans and animals will also add to the body of knowledge surrounding this phenomenon.

With regards to assessing heat vulnerability, future research can consider the other two important HVI factors; sensitivity and adaptive capacity, to generate more accurate and comprehensive overall HVIs and HVI maps.

REFERENCES

1. Arellano, B., & Roca, J. (2023, April 6). *Remote Sensing and Night Time Urban Heat Island*. ResearchGate. Retrieved October 28, 2023, from https://www.researchgate.net/publication/352822228_REMOTE_SENSING_AND_NIGHT_TIME_URBAN_HEAT_ISLAND
2. Bekele, N. K., Hailu, B. T., & Suryabhagavan, K. V. (2022, July 29). *Spatial patterns of urban blue-green landscapes on land surface temperature: A case of Addis Ababa, Ethiopia*. Science Direct. Retrieved May 2, 2023, from https://www.sciencedirect.com/science/article/pii/S266604902200024X
3. Branea, A., Mihai-Ionut, D., Stelian, G. M., & Ștefana, B. (2016, November 8). *Challenges regarding the study of urban heat islands. Ruleset for researchers*. ResearchGate. Retrieved October 30, 2023, from https://www.researchgate.net/publication/309740257_Challenges_regarding_the_study_of_urban_heat_islands_Ruleset_for_researchers
4. Chitonge, H., & Mfune, O. (2015, August). *The urban land question in Africa: The case of urban land conflicts in the City of Lusaka, 100 years after its founding*. ResearchGate. Retrieved October 29, 2023, from https://www.researchgate.net/publication/275773432_The_urban_land_question_in_Africa_The_case_of_urban_land_conflicts_in_the_City_of_Lusaka_100_years_after_its_founding
5. Choate, M. J., Rengarajan, R., Storey, J. C., & Lubke, M. (n.d.). *Landsat Collection 2 | U.S. Geological Survey*. USGS.gov. Retrieved October 6, 2023, from https://www.usgs.gov/landsat-missions/landsat-collection-2
6. City and County of San Francisco. (n.d.). *San Francisco Vulnerability to the Health Impacts of Extreme Heat*. ArcGIS Story Map. Retrieved April 29, 2023, from https://sfgov.maps.arcgis.com/apps/MapJournal/index.html?appid=093e26ddb26a4e3180fa1e35158858bf
7. Conlon, K. C., Mallen, E., Gronlund, C. J., Berrocal, V., Larsen, L., & O’Neill, M. S. (2020, September 2). *Mapping Human Vulnerability to Extreme Heat: A Critical Assessment of Heat Vulnerability Indices Created Using Principal Components Analysis | Environmental Health Perspectives | Vol. 128, No. 9*. Environmental Health Perspectives. Retrieved October 30, 2023, from https://doi.org/10.1289/EHP4030

8. De Almeida, C. R., Gonçalves, A., & Teodoro, A. C. (2021, October 11). *Study of the Urban Heat Island (UHI) Using Remote Sensing Data/Techniques: A Systematic Review*. ResearchGate. Retrieved October 29, 2023, from https://www.researchgate.net/publication/355171565_Study_of_the_Urban_Heat_Island_UHI_Using_Remote_Sensing_DataTechniques_A_Systematic_Review
9. Druckenmiller, H. (2023, March 14). *Urban Heat Islands 101*. Resources for the Future. Retrieved April 29, 2023, from https://www.rff.org/publications/explainers/urban-heat-islands-101/
10. Earth Blox. (2022, August 12). *Advantages and disadvantages of Google Earth Engine | Blog*. Earth Blox. Retrieved October 5, 2023, from https://www.earthblox.io/blog/advantages-and-disadvantages-of-google-earth-engine
11. Environmental Protection Agency. (2022, September 2). *Learn About Heat Islands | US EPA*. Environmental Protection Agency. Retrieved April 29, 2023, from https://www.epa.gov/heatislands/learn-about-heat-islands
12. Estoque, R. C., Murayama, Y., & Myint, S. W. (2017, January 15). *Effects of landscape composition and pattern on land surface temperature: An urban heat island study in the megacities of Southeast Asia*. PubMed. Retrieved October 28, 2023, from https://pubmed.ncbi.nlm.nih.gov/27832866/
13. Fuladlu, K., Riza, M., & Ilkan, M. (2019, March 9). *The Effect Of Rapid Urbanization On The Physical Modification Of Urban Area*. ResearchGate. Retrieved October 29, 2023, from https://www.researchgate.net/publication/326316773_THE_EFFECT_OF_RAPID_URBANIZATION_ON_THE_PHYSICAL_MODIFICATION_OF_URBAN_AREA/figures?lo=1
14. Galodha, A., & Gupta, S. K. (2021, August). *Land Surface Temperature As An Indicator Of Urban Heat Island Effect: A Google Earth Engine Based Web-App*. ResearchGate. Retrieved October 29, 2023, from https://www.researchgate.net/publication/353822830_LAND_SURFACE_TEMPERATURE_AS_AN_INDICATOR_OF_URBAN_HEAT_ISLAND_EFFECT_A_GOOGLE_EARTH_ENGINE_BASED_WEB-APP
15. Ghalehteimouri, K. J., Shamsoddini, A., Mousavi, M. N., Che Ros, F. B., & Khedmatzadeh, A. (2022, July 29). *Predicting spatial and decadal of land use and land cover change using integrated cellular automata Markov chain model-based scenarios (2019–2049) Zarriné-Rūd River Basin in Iran*. Retrieved April 30, 2023, from https://doi.org/10.1016/j.envc.2021.100399

16. Haylemariyam, M. B. (2018). *Detection of Land Surface Temperature in Relation to Land Use Land Cover Change: Dire Dawa City, Ethiopia*. Semantic Scholar. Retrieved October 28, 2023, from https://doi.org/10.4172/2469-4134.1000245
17. Herold, M., Scepan, J., & Clarke, K. C. (2002, August). *The Use of Remote Sensing and Landscape Metrics to Describe Structures and Changes in Urban Land Uses*. Sage Journals. Retrieved September 14, 2024, from https://journals.sagepub.com/doi/10.1068/a3496
18. Hong, T., Xu, Y., Zhang, W., & Zeng, Z. (2021, April 12). *Heat Vulnerability Index Development and Mapping*. ResearchGate. Retrieved April 29, 2023, from https://www.researchgate.net/publication/350808683_Heat_Vulnerability_Index_Development_and_Mapping
19. Imhoff, M., Zhang, P., Wolfe, R. E., & Bounoua, L. (2010, March). *Remote sensing of the urban heat island effect across biomes in the continental USA | Request PDF*. ResearchGate. Retrieved October 29, 2023, from https://www.researchgate.net/publication/222978849_Remote_sensing_of_the_urban_heat_island_effect_across_biomes_in_the_continental_USA
20. John, J., Bindu, G., Srimuruganandam, B., Wadhwa, A., & Rajan, P. (2020, February 18). *Land use/land cover and land surface temperature analysis in Wayanad district, India, using satellite imagery*. Taylor & Francis Online. Retrieved October 24, 2023, from https://www.tandfonline.com/doi/full/10.1080/19475683.2020.1733662
21. Kottek, K., Grieser, J., Beck, C., & Rudolf, B. (2006). World Map of the Köppen-Geiger Climate Classification Updated. *Meteorologische Zeitschrift*, *15*(3), 259-263.
22. Landsat Missions. (n.d.). *Landsat 8*. USGS.gov. Retrieved May 3, 2023, from https://www.usgs.gov/landsat-missions/landsat-8
23. Landsat Missions. (n.d.). *Landsat 5 | U.S. Geological Survey*. USGS.gov. Retrieved April 29, 2023, from https://www.usgs.gov/landsat-missions/landsat-5
24. Lansat Missions. (n.d.). *Landsat 8 | U.S. Geological Survey*. USGS.gov. Retrieved April 29, 2023, from https://www.usgs.gov/landsat-missions/landsat-8
25. Lazzarini, M., Marpu, P. R., & Ghedira, H. (2013, March). *Temperature-land cover interactions: The inversion of urban heat island phenomenon in desert city areas | Request PDF*. ResearchGate. Retrieved October 28, 2023, from https://www.researchgate.net/publication/270831992_Temperature-land_cover_interactions_The_inversion_of_urban_heat_island_phenomenon_in_desert_city_areas

26. Logan, A. (2021, April 16). *Urban Heat Islands | MIT Climate Portal*. MIT Climate Portal. Retrieved April 29, 2023, from https://climate.mit.edu/explainers/urban-heat-islands
27. NASA. (n.d.). *MOD11A1.061 Terra Land Surface Temperature and Emissivity Daily Global 1km*. Google for Developers. Retrieved October 5, 2023, from https://developers.google.com/earth-engine/datasets/catalog/MODIS_061_MOD11A1#description
28. NASA. (n.d.). *USGS Landsat 5 Level 2, Collection 2, Tier 1 | Earth Engine Data Catalog*. Google for Developers. Retrieved October 7, 2023, from https://developers.google.com/earth-engine/datasets/catalog/LANDSAT_LT05_C02_T1_L2#description
29. NASA LAADS DAAC. (n.d.). *MOD11A1 - MODIS/Terra Land Surface Temperature/Emissivity Daily L3 Global 1km SIN Grid*. LAADS DAAC. Retrieved October 7, 2023, from https://ladsweb.modaps.eosdis.nasa.gov/missions-and-measurements/products/MOD11A1/
30. NASA - Landsat Science. (n.d.). *Thematic Mapper*. Landsat Science. Retrieved May 3, 2023, from https://landsat.gsfc.nasa.gov/thematic-mapper/
31. NASA - MODIS. (n.d.). *MODIS Land Surface Temperature and Emissivity (MOD21)*. MODIS Web. Retrieved May 2, 2023, from https://modis.gsfc.nasa.gov/data/dataprod/mod21.php
32. Nguvulu, A., & Okello, N. (2017). Spatial-Temporal Analysis of Land Use Land Cover Change in Lusaka City Using Geoinformatics Tools. *The International Journal of Multi-Disciplinary Research*.
33. Ogunjobi, K. O., Adamu, Y., Akinsanola, A. A., & Orimoloye, I. R. (2018, December 19). *Spatio-temporal analysis of land use dynamics and its potential indications on land surface temperature in Sokoto Metropolis, Nigeria*. The Royal Society. Retrieved October 24, 2023, from https://royalsocietypublishing.org/doi/10.1098/rsos.180661
34. Phan, T. N., Kuch, V., & Lehnert, L. W. (2020, July 27). *Land Cover Classification using Google Earth Engine and Random Forest Classifier—The Role of Image Composition*. MDPI. Retrieved October 7, 2023, from https://www.mdpi.com/2072-4292/12/15/2411
35. Poteet, L. N. (n.d.). *ARSET - Satellite Remote Sensing for Measuring Urban Heat Islands and Constructing Heat Vulnerability Indices*. NASA Applied Sciences. Retrieved May 4, 2023, from https://appliedsciences.nasa.gov/join-mission/training/english/arset-satellite-remote-sensing-measuring-urban-heat-islands-and
36. Poteet, L. N. (2020, November 10). *ARSET - Satellite Remote Sensing for Urban Heat Islands*. NASA Applied Sciences. Retrieved May 4, 2023, from https://appliedsciences.nasa.gov/join-mission/training/english/arset-satellite-remote-sensing-urban-heat-islands

37. Ranagalage, M., Murayama, Y., Dissanayake, D., & Simwanda, M. (2019, October). *The Impacts of Landscape Changes on Annual Mean Land Surface Temperature in the Tropical Mountain City of Sri Lanka: A Case Study of Nuwara Eliya (1996-2017)*. ResearchGate. Retrieved May 3, 2023, from https://www.researchgate.net/publication/336284475_The_Impacts_of_Landscape_Changes_on_Annual_Mean_Land_Surface_Temperature_in_the_Tropical_Mountain_City_of_Sri_Lanka_A_Case_Study_of_Nuwara_Eliya_1996-2017
38. Reid, C. E., Mann, J. K., Alfasso, R., English, P. B., King, G. C., Lincoln, R. A., Margolis, H. G., Rubado, D. J., Sabato, J. E., West, N. L., Woods, B., Navarro, K. M., & Balmes, J. R. (2012, January 31). *Evaluation of a Heat Vulnerability Index on Abnormally Hot Days: An Environmental Public Health Tracking Study*. NCBI. Retrieved October 30, 2023, from https://www.ncbi.nlm.nih.gov/pmc/articles/PMC3346770/
39. Remote Sensing Phenology. (2018, November 27). *NDVI, the Foundation for Remote Sensing Phenology | U.S. Geological Survey*. USGS.gov. Retrieved October 27, 2023, from https://www.usgs.gov/special-topics/remote-sensing-phenology/science/ndvi-foundation-remote-sensing-phenology
40. Roy, B., & Bari, E. (2022). Examining the relationship between land surface temperature and landscape features using spectral indices with Google Earth Engine. *Heliyon*, *8*.
41. Sebaibi, N. (2021, June 10). *(PDF) Urban Heat Island: Causes, Consequences, and Mitigation Measures with Emphasis on Reflective and Permeable Pavements*. ResearchGate. Retrieved October 29, 2023, from https://www.researchgate.net/publication/352258340_Urban_Heat_Island_Causes_Consequences_and_Mitigation_Measures_with_Emphasis_on_Reflective_and_Permeable_Pavements
42. Shrawankar, U., & Khandare, S. (2016, June 20). *Preprocessing Algorithm for High Resolution Satellite Imagery*. ResearchGate. Retrieved October 6, 2023, from https://www.researchgate.net/publication/304140062_Preprocessing_Algorithm_for_High_Resolution_Satellite_Imagery
43. Simwanda, M., & Murayama, Y. (2016). Urban growth in Lusaka city, Zambia: Characterizing the spatial pattern and intensity of changes in urban land use.
44. Simwanda, M., Murayama, Y., & Ranagalage, M. (2020, March). Modeling the drivers of urban land use changes in Lusaka, Zambia using multi-criteria evaluation: An analytic network process approach. *ScienceDirect, 92*. https://doi.org/10.1016/j.landusepol.2019.104441

45. Simwanda, M., Ranagalage, M., Estoque, R. C., & Murayama, Y. (2019). Spatial Analysis of Surface Urban Heat Islands in Four Rapidly Growing African Cities. *Remote Sensing*, *11*(14). https://doi.org/10.3390/rs11141645
46. Tariq, A., & Shu, H. (2020). CA-Markov Chain Analysis of Seasonal Land Surface Temperature and Land Use Land Cover Change Using Optical Multi-Temporal Satellite Data of Faisalabad, Pakistan. *Remote Sensing*, *12*(20). Retrieved April 30, 2023, from https://doi.org/10.3390/rs12203402
47. Terra- NASA. (n.d.). *MODIS Data*. Terra. Retrieved May 2, 2023, from https://terra.nasa.gov/data/modis-data
48. Ullah, N., Siddique, M. A., Ding, M., Grigoryan, S., Khan, I. A., Kang, Z., Tsou, S., Zhang, T., Hu, Y., & Zhang, Y. (2023). The Impact of Urbanization on Urban Heat Island: Predictive Approach Using Google Earth Engine and CA-Markov Modelling (2005–2050) of Tianjin City, China. *Int. J. Environ. Res. Public Health*, *20*(3). https://doi.org/10.3390/ ijerph20032642
49. UN Habitat. (2007). *Zambia: Lusaka Urban Profile*. UNON.
50. U.S. Environmental Protection Agency. (2008, June 1). *Reducing Urban Heat Islands: Compendium of Strategies*, *Urban Heat Island Basics*. Building America Solution Center. Retrieved October 30, 2023, from https://basc.pnnl.gov/library/reducing-urban-heat-islands-compendium-strategies-urban-heat-island-basics
51. US EPA. “Learn About Heat Islands | US EPA.” Environmental Protection Agency, 28 August 2022, https://www.epa.gov/heatislands/learn-about-heat-islands. Accessed 17 July 2023.
52. USGS. (n.d.). *What are the band designations for the Landsat satellites? | U.S. Geological Survey*. USGS.gov. Retrieved October 5, 2023, from https://www.usgs.gov/faqs/what-are-band-designations-landsat-satellites
53. Wang, J. W., Chow, W. T.L., & Wang, Y.-C. (2020). A global regression method for thermal sharpening of urban land surface temperatures from MODIS and Landsat. *International Journal of Remote Sensing*, *41*(8). https://doi.org/10.1080/01431161.2019.1697009
54. Wu, C., Li, J., Wang, C., Song, C., Chen, Y., Finka, M., & La Rosa, D. (2019, December 1). *Understanding the relationship between urban blue infrastructure and land surface temperature*. ScienceDirect. Retrieved October 27, 2023, from https://www.sciencedirect.com/science/article/abs/pii/S0048969719336800

APPENDICES

Appendix A: Additional LST Imagery

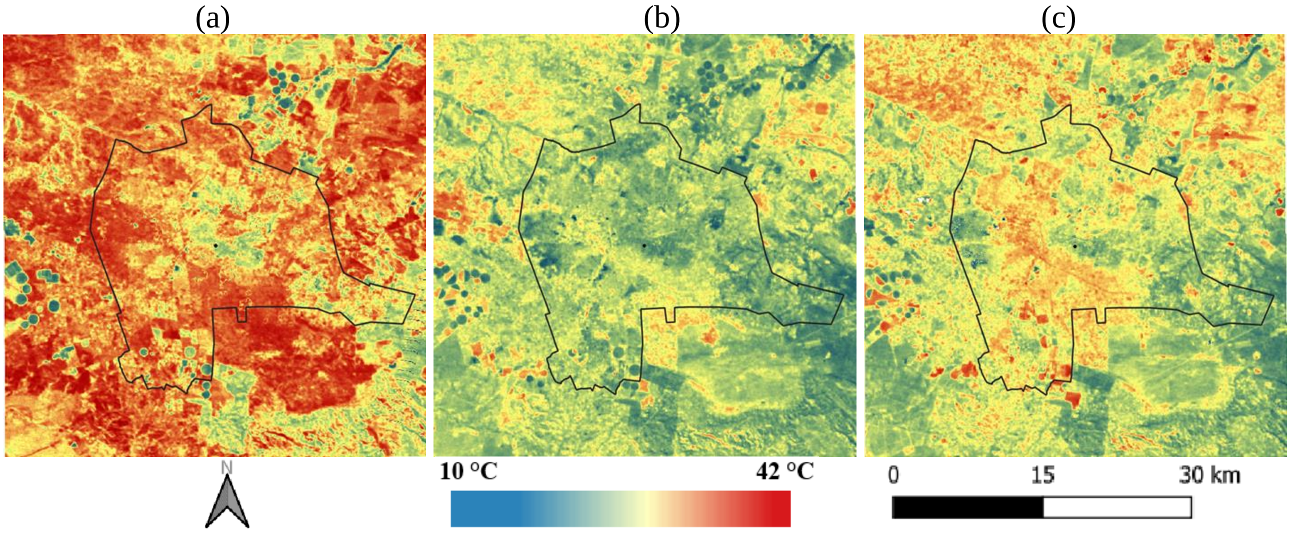

A-1. Winter Landsat LST for (a) 2005 (b) 2015, and (c) 2022.

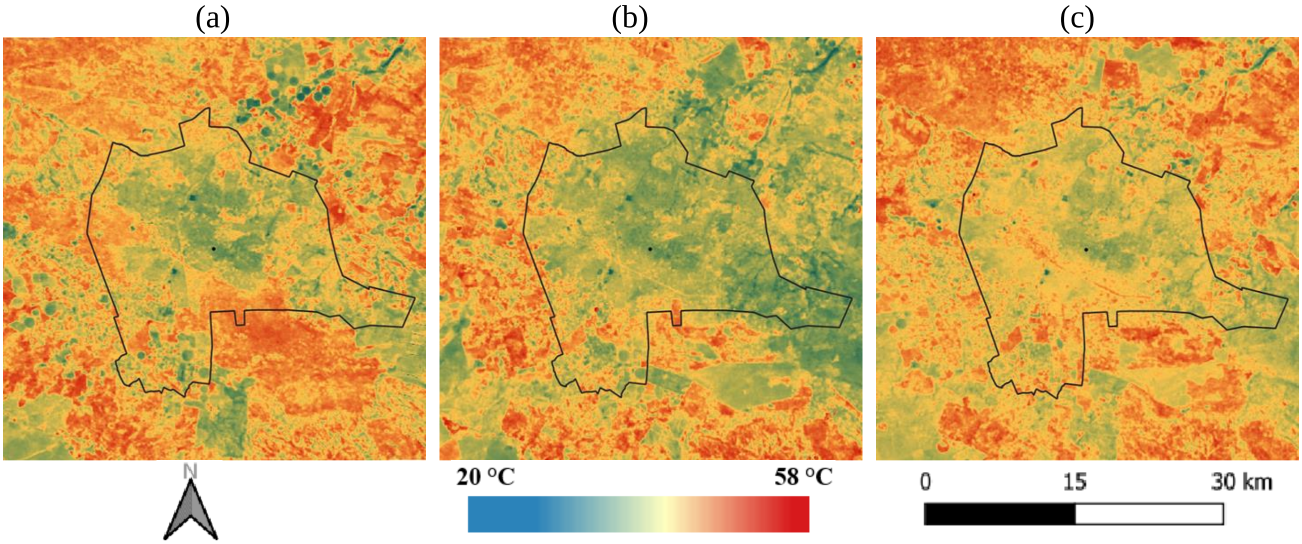

A-2. Summer Landsat LST for (a) 2005 (b) 2015, and (c) 2022.

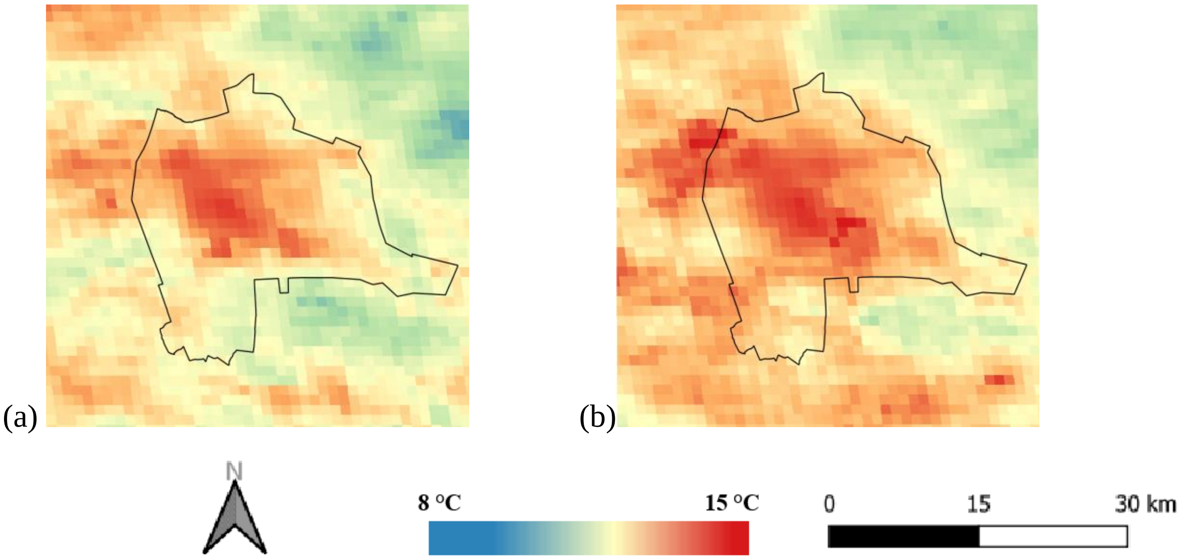

A-3. Nighttime-winter MODIS LST for (a) 2005-2007, and (b) 2015-2017.

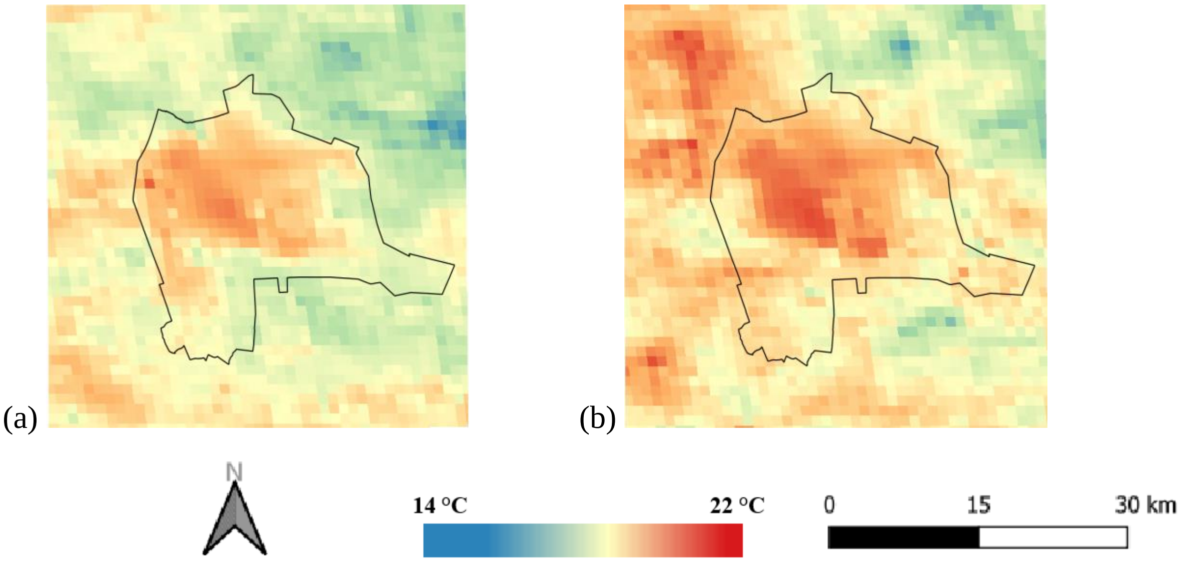

A-4. Nighttime-summer MODIS LST for (a) 2005-2007, and (b) 2015-2017.

Appendix B: Additional LULC Imagery

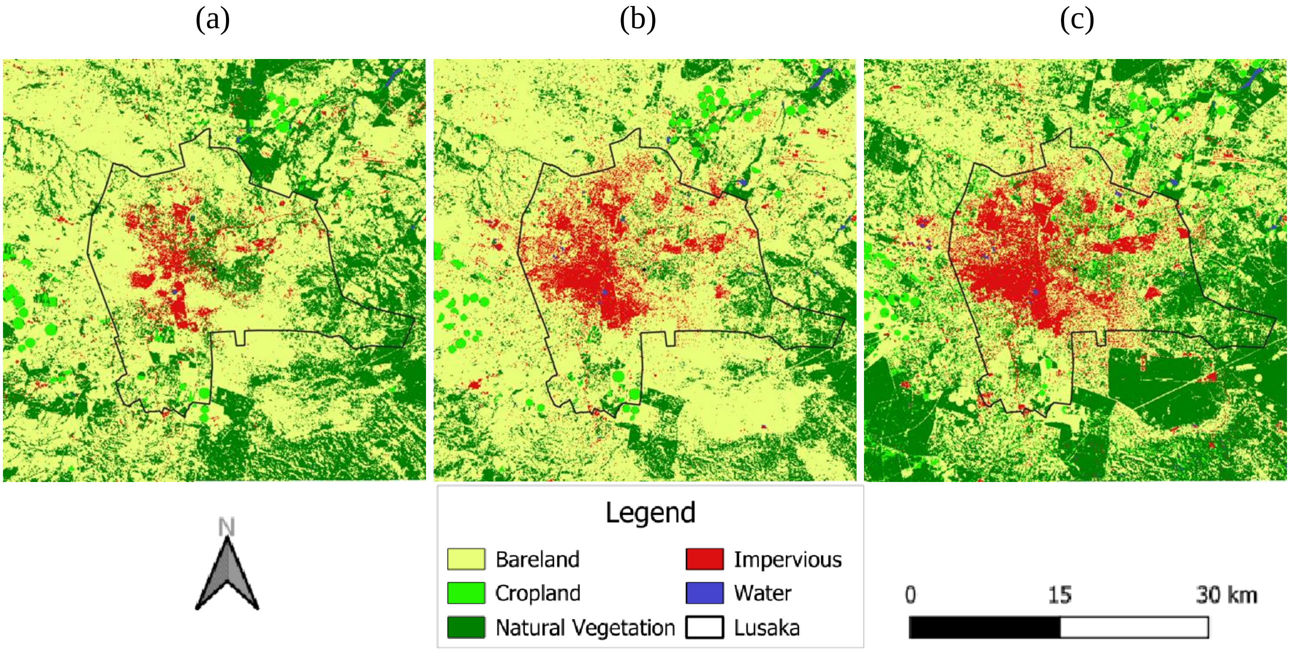

B-1. Winter Landsat LULC for (a) 2005 (b) 2015, and (c) 2022.

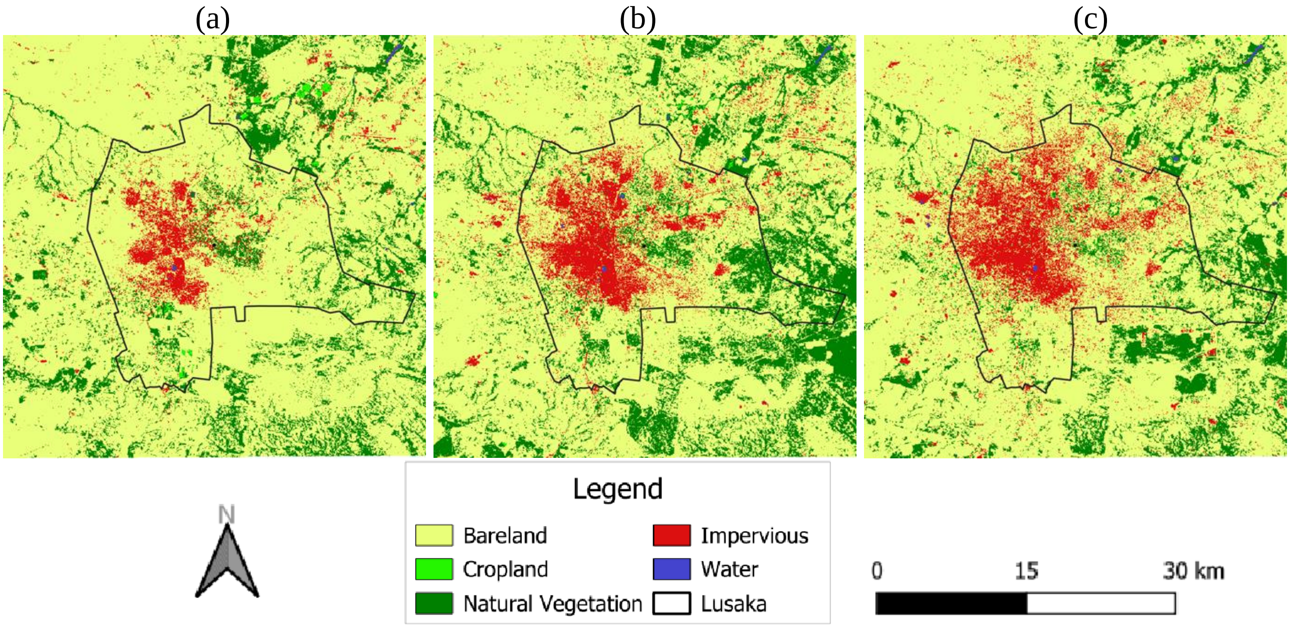

B-2. Summer Landsat LULC for (a) 2005 (b) 2015, and (c) 2022.

Appendix C: LULC Confusion Matrices and Classification Accuracies

(a)

```
Confusion matrix:
▾List (6 elements)
  ▸0: [0,0,0,0,0,0]
  ▸1: [0,92,0,0,0,0]
  ▸2: [0,0,9,0,0,0]
  ▸3: [0,0,0,34,0,0]
  ▸4: [0,0,0,0,55,0]
  ▸5: [0,0,0,0,0,17]

Training Overall Accuracy:
1

Training Kappa
1

Validation Error Matrix RF:
▾List (6 elements)
  ▸0: [0,0,0,0,0,0]
  ▸1: [0,18,0,0,0,0]
  ▸2: [0,0,2,0,0,0]
  ▸3: [0,0,0,6,0,0]
  ▸4: [0,2,0,0,9,0]
  ▸5: [0,0,0,0,0,2]

Validation Overall Accuracy RF:
0.9487179487179487

Validation Kappa
0.9233791748526522
```

(b)

```
Confusion matrix:
▾List (6 elements)
  ▸0: [0,0,0,0,0,0]
  ▸1: [0,73,0,0,0,0]
  ▸2: [0,0,41,1,0,0]
  ▸3: [0,1,1,35,0,0]
  ▸4: [0,0,0,0,53,0]
  ▸5: [0,0,0,0,0,12]

Training Overall Accuracy:
0.9861751152073732

Training Kappa
0.9817329816488017

Validation Error Matrix RF:
▾List (6 elements)
  ▸0: [0,0,0,0,0,0]
  ▸1: [0,19,0,0,0,0]
  ▸2: [0,0,14,0,0,0]
  ▸3: [0,0,0,7,0,0]
  ▸4: [0,0,0,0,10,0]
  ▸5: [0,0,0,0,0,8]

Validation Overall Accuracy RF:
1

Validation Kappa
1
```

(c)

```
Confusion matrix:
▾List (6 elements)
  ▸0: [0,0,0,0,0,0]
  ▸1: [0,71,0,0,0,0]
  ▸2: [0,1,21,0,0,0]
  ▸3: [0,0,0,35,0,1]
  ▸4: [0,0,0,0,48,0]
  ▸5: [0,0,0,0,0,17]

Training Overall Accuracy:
0.9896907216494846

Training Kappa
0.9862372304199774

Validation Error Matrix RF:
▾List (6 elements)
  ▸0: [0,0,0,0,0,0]
  ▸1: [0,19,0,0,1,0]
  ▸2: [0,0,8,0,0,0]
  ▸3: [0,0,2,6,0,0]
  ▸4: [0,0,0,0,13,0]
  ▸5: [0,0,0,0,0,3]

Validation Overall Accuracy RF:
0.9423076923076923

Validation Kappa
0.9221945137157107
```

(d)

```
Confusion matrix:
▾List (6 elements)
  ▸0: [0,0,0,0,0,0]
  ▸1: [0,114,0,0,0,0]
  ▸2: [0,0,111,0,0,0]
  ▸3: [0,0,0,49,0,0]
  ▸4: [0,0,0,0,89,0]
  ▸5: [0,0,0,0,1,27]

Training Overall Accuracy:
0.9974424552429667

Training Kappa
0.9966408068936483

Validation Error Matrix RF:
▾List (6 elements)
  ▸0: [0,0,0,0,0,0]
  ▸1: [0,24,0,0,1,0]
  ▸2: [0,0,22,1,0,0]
  ▸3: [0,0,1,16,0,0]
  ▸4: [0,1,0,0,19,0]
  ▸5: [0,0,0,0,0,8]

Validation Overall Accuracy RF:
0.956989247311828

Validation Kappa
0.9448234945120143
```

(e)

```
Confusion matrix:
▾List (6 elements)
  ▸0: [0,0,0,0,0,0]
  ▸1: [0,92,0,0,0,0]
  ▸2: [0,0,126,0,0,0]
  ▸3: [0,0,1,47,0,0]
  ▸4: [0,0,0,1,102,0]
  ▸5: [0,0,0,0,0,24]

Training Overall Accuracy:
0.9949109414758269

Training Kappa
0.9932588317023594

Validation Error Matrix RF:
▾List (6 elements)
  ▸0: [0,0,0,0,0,0]
  ▸1: [0,21,0,0,2,0]
  ▸2: [0,0,26,0,0,0]
  ▸3: [0,0,0,9,0,0]
  ▸4: [0,1,0,0,23,0]
  ▸5: [0,0,0,0,1,8]

Validation Overall Accuracy RF:
0.9560439560439561

Validation Kappa
0.9424232837709586
```

(f)

```
Confusion matrix:
▾List (6 elements)
  ▸0: [0,0,0,0,0,0]
  ▸1: [0,86,0,1,1,0]
  ▸2: [0,0,104,0,0,0]
  ▸3: [0,0,0,88,0,0]
  ▸4: [0,0,0,0,95,0]
  ▸5: [0,0,0,1,0,29]

Training Overall Accuracy:
0.9925925925925926

Training Kappa
0.9904878220635556

Validation Error Matrix RF:
▾List (6 elements)
  ▸0: [0,0,0,0,0,0]
  ▸1: [0,25,0,1,2,0]
  ▸2: [0,0,24,0,0,0]
  ▸3: [0,0,0,23,0,0]
  ▸4: [0,1,0,0,22,0]
  ▸5: [0,0,0,0,0,8]

Validation Overall Accuracy RF:
0.9622641509433962

Validation Kappa
0.9516202647193063
```

C-1. Winter Landsat LULC confusion matrices and classification accuracies for (a) 1998 (b) 2005 (c) 2008 (d) 2015, (e) 2020, and (f) 2022. Where 1-bare land, 2- cropland, 3-natural vegetation, 4-impervious surfaces, and 5- water.

(a)

```
Confusion matrix:
▾List (6 elements)
  ▸0: [0,0,0,0,0,0]
  ▸1: [0,98,0,0,0,0]
  ▸2: [0,0,10,0,0,0]
  ▸3: [0,0,1,36,0,0]
  ▸4: [0,0,0,0,49,0]
  ▸5: [0,0,0,0,0,17]

Training Overall Accuracy:
0.995260663507109

Training Kappa
0.9931460126685071

Validation Error Matrix RF:
▾List (6 elements)
  ▸0: [0,0,0,0,0,0]
  ▸1: [0,22,0,0,1,0]
  ▸2: [0,0,6,0,0,0]
  ▸3: [0,0,0,5,1,0]
  ▸4: [0,0,0,0,17,0]
  ▸5: [0,0,0,0,0,5]

Validation Overall Accuracy RF:
0.9649122807017544

Validation Kappa
0.9510519536281664
```

(b)

```
Confusion matrix:
▾List (6 elements)
  ▸0: [0,0,0,0,0,0]
  ▸1: [0,85,0,0,0,0]
  ▸2: [0,0,7,0,0,0]
  ▸3: [0,0,0,45,0,0]
  ▸4: [0,0,0,0,68,0]
  ▸5: [0,0,0,0,0,17]

Training Overall Accuracy:
1

Training Kappa
1

Validation Error Matrix RF:
▾List (6 elements)
  ▸0: [0,0,0,0,0,0]
  ▸1: [0,23,0,0,1,0]
  ▸2: [0,0,2,1,0,0]
  ▸3: [0,0,0,8,0,0]
  ▸4: [0,0,0,0,13,0]
  ▸5: [0,0,0,0,0,6]

Validation Overall Accuracy RF:
0.9629629629629629

Validation Kappa
0.9477756286266922
```

(c)

```
Confusion matrix:
▾List (6 elements)
  ▸0: [0,0,0,0,0,0]
  ▸1: [0,101,0,0,0,0]
  ▸2: [0,0,15,0,0,0]
  ▸3: [0,0,0,49,0,0]
  ▸4: [0,0,0,0,64,0]
  ▸5: [0,0,0,0,0,18]

Training Overall Accuracy:
1

Training Kappa
1

Validation Error Matrix RF:
▾List (6 elements)
  ▸0: [0,0,0,0,0,0]
  ▸1: [0,15,0,0,2,0]
  ▸2: [0,0,3,0,0,0]
  ▸3: [0,0,0,13,0,0]
  ▸4: [0,0,0,0,20,0]
  ▸5: [0,0,0,0,0,5]

Validation Overall Accuracy RF:
0.9655172413793104

Validation Kappa
0.9529602595296026
```

(d)

```
Confusion matrix:
▾List (6 elements)
  ▸0: [0,0,0,0,0,0]
  ▸1: [0,95,0,0,0,0]
  ▸2: [0,0,4,0,0,0]
  ▸3: [0,0,0,47,0,0]
  ▸4: [0,0,0,0,83,0]
  ▸5: [0,0,0,0,0,15]

Training Overall Accuracy:
1

Training Kappa
1

Validation Error Matrix RF:
▾List (6 elements)
  ▸0: [0,0,0,0,0,0]
  ▸1: [0,28,0,0,1,0]
  ▸2: [0,0,1,1,0,0]
  ▸3: [0,0,1,11,0,1]
  ▸4: [0,1,0,0,21,0]
  ▸5: [0,0,0,1,1,2]

Validation Overall Accuracy RF:
0.9

Validation Kappa
0.8545130641330166
```

(e)

```
Confusion matrix:
▾List (6 elements)
  ▸0: [0,0,0,0,0,0]
  ▸1: [0,82,0,0,1,0]
  ▸2: [0,0,17,0,0,0]
  ▸3: [0,0,0,51,0,0]
  ▸4: [0,1,0,0,85,0]
  ▸5: [0,0,0,0,0,14]

Training Overall Accuracy:
0.9920318725099602

Training Kappa
0.9889984659215428

Validation Error Matrix RF:
▾List (6 elements)
  ▸0: [0,0,0,0,0,0]
  ▸1: [0,22,1,0,0,0]
  ▸2: [0,0,2,1,0,0]
  ▸3: [0,0,1,11,0,0]
  ▸4: [0,1,0,0,19,0]
  ▸5: [0,0,0,0,0,4]

Validation Overall Accuracy RF:
0.9354838709677419

Validation Kappa
0.9102424900470504
```

(f)

```
Confusion matrix:
▾List (6 elements)
  ▸0: [0,0,0,0,0,0]
  ▸1: [0,99,0,0,1,0]
  ▸2: [0,0,5,0,0,0]
  ▸3: [0,0,0,49,0,0]
  ▸4: [0,0,0,0,89,0]
  ▸5: [0,0,0,0,0,17]

Training Overall Accuracy:
0.9961538461538462

Training Kappa
0.9944651410324641

Validation Error Matrix RF:
▾List (6 elements)
  ▸0: [0,0,0,0,0,0]
  ▸1: [0,28,0,1,1,0]
  ▸2: [0,0,1,0,0,0]
  ▸3: [0,1,0,12,0,1]
  ▸4: [0,1,0,0,18,0]
  ▸5: [0,0,0,0,0,2]

Validation Overall Accuracy RF:
0.9242424242424242

Validation Kappa
0.8864418444597384
```

C-2. Summer Landsat LULC confusion matrices and classification accuracies for (a) 1998 (b) 2005 (c) 2008 (d) 2015, (e) 2020, and (f) 2022. Where 1-bare land, 2- cropland, 3-natural vegetation, 4-impervious surfaces, and 5-water.

Appendix D: Additional LST-NDVI Correlation

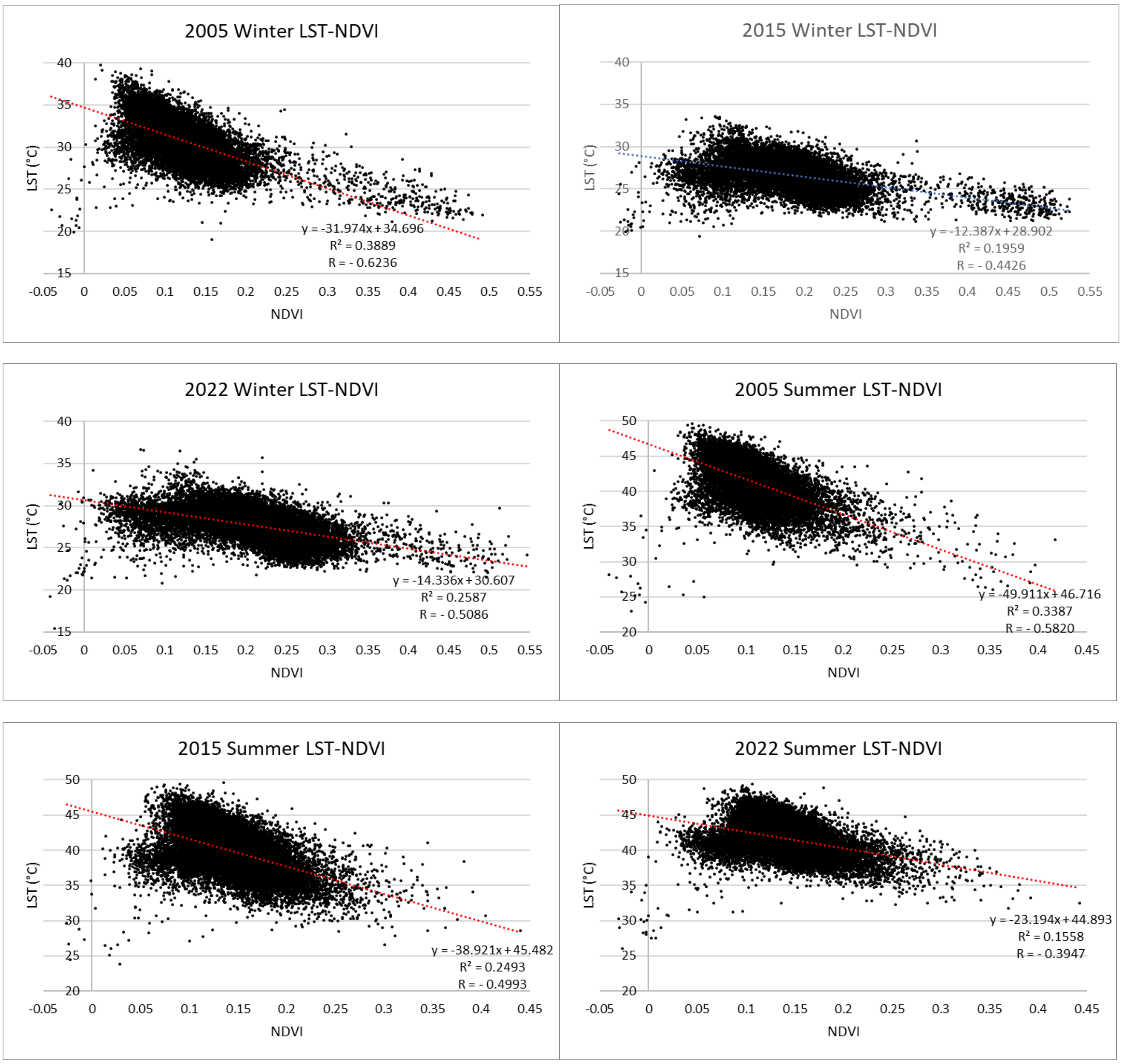

D-1. Landsat LST-NDVI correlations.

Appendix E: HVI Scores for Lusaka Neighbourhoods

E-1. Neighbourhood HVI Scores for LST.

Land Surface Temperature				
1	**2**	**3**	**4**	**5**
Kabulonga	Kalikiliki	Lusaka East Forest Reserve	Mutambe	Chawama-Liyali
Tukunka	Chifwema	Twin Palm	State Lodge	Lilayi
Cathedral Hill	Kangombe	Linda	Chalala	Chilenje
	Handsworth	NRDC	Leopards Hill	Libala
	Jesmondine	Avondale	Mimosa	Freedom
	Kalundu	Chainama	Balastone Park	Kabwata
	Olympia Park	Chudleigh	Chazanga	Kaunda Square
	Roma	Chamba Valley	Hillview Chalala	Chainda
	Ibex Hill	Chelstone	Konkwa	John Howard
	Longacres	Foxdale	Kwamwena	Chawama
	Maluba	Luburma	Makeni	Industrial Area
	Show Grounds	Ridgeway	Makeni Bonaventure	Kamwala
	Sunningdale	Salama Park	Munali	Namununga
	Kalikiliki	UNZA	Ngwerere	Chibolya
		Woodlands	PHI	Chinka
		Northmead	Chunga	
		Highland	Kamanga	
		Garden	Libala South	
		Garden Park	Matero North	
		Hellen Kaunda	Kalingalinga	
		Kabanana	Lilanda	
		Luneta	Matero	
		Madras	Mulobela	
		Mtendere	Chaisa	
		Ngombe	Chipata	
		Thornark	George	
		Bauleni	John Laing	
		Chilulu	Kamwala South	
		Misisi	Kanyama	

where an HVI score of 1 indicates very low vulnerability and an HVI score of 5 indicates a very high vulnerability to instances of extreme heat.

E-2. Neighbourhood HVI Scores for vegetation cover.

Vegetation Cover				
2	**3**	**4**	**5**	**6**
Kabulonga	Ibex Hill	Highland	Kalikiliki	Misisi
Tukunka	Longacres	Garden	Bauleni	
Cathedral Hill	Maluba	Garden Park	Chilulu	
Chifwema	Show Grounds	Hellen Kaunda	Chaisa	
Kangombe	Sunningdale	Kabanana	Chipata	
Handsworth	Linda	Luneta	George	
Jesmondine	NRDC	Madras	John Laing	
Kalundu	Chamba Valley	Mtendere	Kamwala South	
Olympia Park	Chelstone	Ngombe	Kanyama	
Roma	Foxdale	Thornark	Mutambe	
Lusaka East Forest Reserve	Luburma	Chunga	Freedom	
Twin Palm	Ridgeway	Kamanga	Chainda	
Avondale	Salama Park	Libala South	John Howard	
Chainama	UNZA	Matero North	Chawama	
Chudleigh	Woodlands	Kalingalinga	Industrial Area	
State Lodge	Northmead	Lilanda	Kamwala	
	Chalala	Matero	Namununga	
	Leopards Hill	Mulobela	Chibolya	
	Mimosa	Chilenje	Chinka	
	Balastone Park	Libala		
	Chazanga	Kabwata		
	Hillview Chalala	Kaunda Square		
	Konkwa			
	Kwamwena			
	Makeni			
	Makeni Bonaventure			
	Munali			
	Ngwerere			
	PHI			
	Chawama-Liyali			
	Lilayi			

where an HVI score of 2 indicates very low vulnerability and an HVI score of 6 indicates a very high vulnerability to instances of extreme heat.

E-3. Neighbourhood HVI Scores for impervious surfaces.

Impervious Surfaces				
2	**3**	**4**	**5**	**6**
Kabulonga	Cathedral Hill	Garden	Matero	Chibolya
Tukunka	Handsworth	Garden Park	Mulobela	Chinka
Chifwema	Jesmondine	Hellen Kaunda	Chilulu	Misisi
Kangombe	Kalundu	Kabanana	Chaisa	
Lusaka East Forest Reserve	Olympia Park	Luneta	Chipata	
Twin Palm	Roma	Madras	George	
State Lodge	Avondale	Mtendere	John Laing	
Linda	Chainama	Ngombe	Kamwala South	
NRDC	Chudleigh	Thornark	Kanyama	
Chalala	Ibex Hill	Kalingalinga	Mutambe	
Leopards Hill	Longacres	Lilanda	Chawama	
Mimosa	Maluba	Kabwata	Industrial Area	
Chawama-Liyali	Show Grounds	Kaunda Square	Kamwala	
Lilayi	Sunningdale	Kalikiliki	Namununga	
	Chamba Valley	Bauleni		
	Chelstone	Chainda		
	Foxdale	John Howard		
	Luburma			
	Ridgeway			
	Salama Park			
	UNZA			
	Woodlands			
	Balastone Park			
	Chazanga			
	Hillview Chalala			
	Konkwa			
	Kwamwena			
	Makeni			
	Makeni Bonaventure			
	Munali			
	Ngwerere			
	PHI			
	Chunga			
	Kamanga			
	Libala South			
	Matero North			
	Chilenje			
	Libala			
	Freedom			
	Northmead			
	Highland			

where an HVI score of 2 indicates very low vulnerability and an HVI score of 6 indicates a very high vulnerability to instances of extreme heat.

E-4. Neighbourhood HVI Scores for bare land.

Bare Land				
1	**2**	**3**	**4**	**5**
John Laing	Garden	Kabulonga	Tukunka	Twin Palm
Chibolya	Mulobela	Kangombe	Chifwema	Linda
Chinka	Chilulu	Cathedral Hill	Lusaka East Forest Reserve	Chalala
Misisi	Chaisa	Olympia Park	State Lodge	Leopards Hill
	Chipata	Show Grounds	NRDC	Mimosa
	George	Northmead	Handsworth	Chawama-Liyali
	Kamwala South	Garden Park	Jesmondine	Lilayi
	Kanyama	Hellen Kaunda	Kalundu	Chazanga
	Mutambe	Kabanana	Roma	Hillview Chalala
	Chawama	Luneta	Avondale	Kwamwena
	Industrial Area	Madras	Chainama	Makeni Bonaventure
	Kamwala	Mtendere	Chudleigh	Munali
	Namununga	Ngombe	Ibex Hill	Ngwerere
		Thornark	Longacres	Chilenje
		Kalingalinga	Maluba	Libala
		Lilanda	Sunningdale	
		Kabwata	Chamba Valley	
		Kalikiliki	Chelstone	
		Bauleni	Foxdale	
		Chainda	Luburma	
		John Howard	Ridgeway	
		Matero	Salama Park	
			UNZA	
			Woodlands	
			Balastone Park	
			Konkwa	
			Makeni	
			PHI	
			Chunga	
			Kamanga	
			Libala South	
			Matero North	
			Freedom	
			Highland	
			Kaunda Square	

where an HVI score of 1 indicates very low vulnerability and an HVI score of 5 indicates a very high vulnerability to instances of extreme heat.

E-5. Overall neighbourhood HVI Scores.

Overall HVI								
9	**10**	**11**	**12**	**13**	**14**	**15**	**16**	**17**
Kabulonga	Kangombe	Olympia Park	Show Grounds	State Lodge	Garden Park	John Laing	Misisi	Chibolya
	Cathedral Hill	Chifwema	Lusaka East Forest Reserve	NRDC	Hellen Kaunda	Mulobela	Chaisa	Chinka
	Tukunka		Handsworth	Avondale	Kabanana	Chilulu	Chipata	Chawama
			Jesmondine	Chainama	Luneta	Kalingalinga	George	Industrial Area
			Kalundu	Chudleigh	Madras	Lilanda	Kamwala South	Kamwala
			Roma	Ibex Hill	Mtendere	Bauleni	Kanyama	Namununga
				Longacres	Ngombe	Chunga	Mutambe	Chainda
				Maluba	Thornark	Kamanga	Kabwata	John Howard
				Sunningdale	Kalikiliki	Libala South	Matero	Freedom
				Twin Palm	Balastone Park	Matero North		Kaunda Square
				Garden	Konkwa	Highland		Chilenje
				Northmead	Makeni	Chawama-Liyali		Libala
				Chamba Valley	PHI	Lilayi		
				Chelstone	Chalala	Chazanga		
				Foxdale	Leopards Hill	Hillview Chalala		
				Luburma	Mimosa	Kwamwena		
				Ridgeway		Makeni Bonaventure		
				Salama Park		Munali		
				UNZA		Ngwerere		
				Woodlands				
				Linda				

where an HVI score of 9 indicates very low vulnerability and an HVI score of 17 indicates a very high vulnerability to instances of extreme heat.

Appendix F: Google Earth Engine Code

F-1. Landsat 5 GEE LST code for (a) 1998 (b) 2005, and (c) 2008 (Adapted from NASA Applied Remote Sensing Training (ARSET) program).

```
//****************** DEFINE THE STUDY AREA *****************//
// Assign a variable to filter the day of year from May 1 to July 30 and
September 1 to November 30.
var dateMJJ = ee.Filter.dayOfYear(121, 211); // May, June, July filter
var dateSON = ee.Filter.dayOfYear(244, 334); // Sept, Oct, Nov filter

// Assign a variable to filter years between 2000 - 2008.
var year2005 = ee.Filter.calendarRange(2005, 2005,'year');

// Center the map view at defined coordinates (longitude/latitude) with
the given zoom level.
Map.centerObject (aoi, 12);

//****************** CLOUD MASK FUNCTION *****************//
// Assign a variable to the sensor-specific bands unique to each Landsat
mission.
var LC05_bands = ['ST_B6', 'QA_PIXEL']; // Landsat 5 surface temperature
(ST) & QA_Pixel bands

// Create a function to mask clouds and cloud shadows based on the
QA_PIXEL band of Landsat 5
function cloudMask(image) {
  var qa = image.select('QA_PIXEL');
  var mask = qa.bitwiseAnd(1 << 3).or(qa.bitwiseAnd(1 << 4));
  return image.updateMask(mask.not());}

//****************** FILTER IMAGE COLLECTIONS *****************//
// Assign variables to import and filter the Landsat Collections.
//**********2005***************
var filterMJJ2005 =
ee.ImageCollection('LANDSAT/LT05/C02/T1_L2').select('ST_B6', 'QA_PIXEL')

.filterBounds(aoi).filter(dateMJJ).filter(year2005).map(cloudMask);
var filterSON2005 =
ee.ImageCollection('LANDSAT/LT05/C02/T1_L2').select('ST_B6', 'QA_PIXEL')

.filterBounds(aoi).filter(dateSON).filter(year2005).map(cloudMask);

// Filter the collections by the CLOUD_COVER property so each image
contains less than 10% cloud cover.
//**********2005***************
var filteredMJJ2005 = filterMJJ2005.filter(ee.Filter.lt('CLOUD_COVER',
10));
var filteredSON2005 = filterSON2005.filter(ee.Filter.lt('CLOUD_COVER',
10));

//****************** SCALE THE LAND SURFACE TEMPERATURE **************//
// Create a funtion using Landsat scale factors for deriving ST in Kelvin
and Celsius.
function applyScaleFactors(image) {
```

```
  var thermalBands =
image.select('ST_B6').multiply(0.00341802).add(149.0) // Scale factors
for Kelvin
  .subtract(273.15); // Scale factor for degrees Celsius
  return image.addBands(thermalBands, null, true);
}

// Define a variable to apply scale factors to the filtered image
collection.
//*********2005**************
var scaledMJJ2005 = filteredMJJ2005.map(applyScaleFactors);
var scaledSON2005 = filteredSON2005.map(applyScaleFactors);

// // Print the LST image collection arguments to the console.
// //*********2005**************
// print(filteredMJJ2005, 'MJJ 2005 Landsat 5 ST (Celsius)');
// print(filteredSON2005, 'SON 2005 Landsat 5 ST (Celsius)');

//***************** CALCULATE MEAN SURFACE TEMPERATURE **************//
// Define a variable to calculate mean ST for each pixel in the filtered
image collection.
//*********2005**************
var meanMJJ2005 = scaledMJJ2005.mean();
var meanSON2005 = scaledSON2005.mean();

// Define variable to use clip function to subset the imagery to the aoi.
//*********2005**************
var clipMeanMJJ2005 = meanMJJ2005.clip(aoi);
var clipMeanSON2005 = meanSON2005.clip(aoi);

// // Print the LST image arguments to the console.
// //*********2005**************
// print(clipMeanMJJ2005, '2005 MJJ Mean ST clipped to study area');
// print(clipMeanSON2005, '2005 SON Mean ST clipped to study area')

//***************** DISPLAY LST MAP ****************//
// Add the image to the map window, and display the results.
//*********2005**************
Map.addLayer(clipMeanMJJ2005, {bands: "ST_B6", min: 20, max: 36,
            palette: ['green','yellow','red']}, "MJJ2005");

Map.addLayer(clipMeanSON2005, {bands: "ST_B6", min: 30, max: 52,
            palette: ['green','yellow','red']}, "SON2005");

//***************** EXPORT LST MAP ****************//
// Export LST image to drive
//*********2005**************
Export.image.toDrive({image: clipMeanMJJ2005, description:
'MJJ2005Landsat5LST',
                      crs: "EPSG:4326", scale: 30, region: aoi,});

Export.image.toDrive({image: clipMeanSON2005, description:
'SON2005Landsat5LST',
                      crs: "EPSG:4326", scale: 30, region: aoi,});
```

F-2. Landsat 8 GEE LST code for (a) 2015 (b) 2020, and (c) 2022 (Adapted from NASA Applied Remote Sensing Training (ARSET) program)..

```
//****************** DEFINE THE STUDY AREA *****************//
// Assign a variable to filter the day of year from May 1 to July 30 and
September 1 to November 30.
var dateMJJ = ee.Filter.dayOfYear(121, 211);
var dateSON = ee.Filter.dayOfYear(244, 334);

// Assign a variable to filter years between 2015 - 2022.
var year2022 = ee.Filter.calendarRange(2022, 2022,'year');

// Center the map view at defined coordinates (longitude/latitude) with
the given zoom level.
Map.centerObject (aoi, 12);

//****************** CLOUD MASK FUNCTION *****************//
// Assign a variable to the sensor-specific bands unique to each Landsat
mission.
var LC08_bands = ['ST_B10', 'QA_PIXEL']; // Landsat 8 surface temperature
(ST) & QA_Pixel band

// Create a function to mask clouds and cloud shadows based on the
QA_PIXEL band of Landsat 8 & 9
function cloudMask(image) {
  var qa = image.select('QA_PIXEL');
  var mask = qa.bitwiseAnd(1 << 3).or(qa.bitwiseAnd(1 << 4));
  return image.updateMask(mask.not());}

//****************** FILTER IMAGE COLLECTIONS *****************//
/* Assign variables to import and filter the Landsat Collections. */
//*********2022**************
var filterMJJ2022 =
ee.ImageCollection('LANDSAT/LC08/C02/T1_L2').select('ST_B10', 'QA_PIXEL')
.filterBounds(aoi).filter(dateMJJ).filter(year2022).map(cloudMask);

var filterSON2022 =
ee.ImageCollection('LANDSAT/LC08/C02/T1_L2').select('ST_B10', 'QA_PIXEL')
.filterBounds(aoi).filter(dateSON).filter(year2022).map(cloudMask);


// Filter the collections by the CLOUD_COVER property so each image
contains less than 10% cloud cover.
//*********2022**************
var filteredMJJ2022 = filterMJJ2022.filter(ee.Filter.lt('CLOUD_COVER',
10));
var filteredSON2022 = filterSON2022.filter(ee.Filter.lt('CLOUD_COVER',
10));

//****************** SCALE THE LAND SURFACE TEMPERATURE ***************//
// Create a funtion using Landsat scale factors for deriving ST in Kelvin
and Celsius.
function applyScaleFactors(image) {
```

```
  var thermalBands =
image.select('ST_B10').multiply(0.00341802).add(149.0) // Scale factors
for Kelvin
  .subtract(273.15); // Scale factor for degrees Celsius
  return image.addBands(thermalBands, null, true);
}

// Define a variable to apply scale factors to the filtered image
collection.
//*********2022**************
var scaledMJJ2022 = filteredMJJ2022.map(applyScaleFactors);
var scaledSON2022 = filteredSON2022.map(applyScaleFactors);

// // Print the LST image collection arguments to the console.
// //*********2022**************
// print(filteredMJJ2022, 'MJJ 2022 Landsat 8 ST (Celsius)');
// print(filteredSON2022, 'SON 2022 Landsat 8 ST (Celsius)');

//****************** CALCULATE MEAN SURFACE TEMPERATURE ***************//
// Define a variable to calculate mean ST for each pixel in the filtered
image collection.
//*********2022**************
var meanMJJ2022 = scaledMJJ2022.mean();
var meanSON2022 = scaledSON2022.mean();

// Define variable to use clip funtion to subset the imagery to the aoi.
//*********2022**************
var clipMeanMJJ2022 = meanMJJ2022.clip(aoi);
var clipMeanSON2022 = meanSON2022.clip(aoi);

//****************** DISPLAY LST MAP *****************//
// // Add the image to the map window, and display the results.
// //*********2022**************
// Map.addLayer(clipMeanMJJ2022, {bands: "ST_B10", min: 20, max: 36,
//             palette: ['green','yellow','red']}, "MJJ2022");

// Map.addLayer(clipMeanSON2022, {bands: "ST_B10", min: 30, max: 52,
//             palette: ['green','yellow','red']}, "SON2022");

//****************** EXPORT LST MAP *****************//
// Export LST image to drive
//*********2022**************
Export.image.toDrive({image: clipMeanMJJ2022, description:
'MJJ2022Landsat8LST',
                      crs: "EPSG:4326", scale: 30, region: aoi,});

Export.image.toDrive({image: clipMeanSON2022, description:
'SON2022Landsat8LST',
                      crs: "EPSG:4326", scale: 30, region: aoi,});
```

F-3. MODIS GEE LST code (Adapted from NASA Applied Remote Sensing Training (ARSET) program).

```
// Filter day of year from September 1 to November 30.
var DATE_RANGE = ee.Filter.dayOfYear(244, 334);

// Filter years from 2010 – 2022.
var YEAR_RANGE = ee.Filter.calendarRange(2010, 2012,'year');

// Delineate your area of interest
var STUDYBOUNDS = aoi;
var DISPLAY = true;

 // Center the map on the image.
Map.centerObject(STUDYBOUNDS, 11);

// Set the basemap to display as satellite.
Map.setOptions('SATELLITE');


// QUALITY MASK
    // Compute the Quality Control bits to extract a value that
represents bit-packed combinations of surface, atmosphere, and sensor
conditions that can affect the overall usefulness of a given pixel.
var getQCBits = function(image, start, end, newName) {
    var pattern = 0;
    for (var i = start; i <= end; i++) {
      pattern += Math.pow(2, i);}
    // Return a single band image of the extracted QC bits, giving the
band a new name.
    return image.select([0], [newName.
                bitwiseAnd(pattern).rightShift(start);};

// Mask out cloudy pixels & cloud state using the QC band.
var maskQC = function(image) {
  // Select the QC_Night and QC_Day bands from the MODIS data product
  var QC = image.select('QC_Night','QC_Day');
  // Get the internal_cloud_algorithm_flag bit.
  var cloud = getQCBits(QC, 0,1, 'QC_state')
              .expression("b(0) == 3 || b(0) == 2");
  var error = getQCBits(QC, 6, 7, 'T_err')
              .expression(" b(0) == 3");
  // Return an image masking out cloudy and low quality areas
  image = image.updateMask(error.not());
  return image.updateMask(cloud.not());};

// RETRIEVING DATA
  // Filter MODIS image collection by year, date ranges, and geographical
boundaries. Apply the cloud mask to collection.
  var collection = ee.ImageCollection("MODIS/061/MOD11A1").
                      filter(DATE_RANGE).filter(YEAR_RANGE).map(maskQC);
// Print the argument to the console tab.
print(collection);

// TRANSFORM DAYTIME & NIGHTTIME LST TO CELSIUS THROUGH RESCALING
```

```
// Derive nighttime LST in Celsius
var NightLST_C = collection.map(function(image)
                {
                  return image.addBands(
                    image.expression(
                '(A * 0.02) - 273.15',
                {
                  'A' : image.select('LST_Night_1km')
                // rename the band LST_Night_1km to LSTN_C
                }).rename('LSTN_C'))});

// Derive daytime LST in Celsius
var DayLST_C = collection.map(function(image)
                {
                  return image.addBands(
                    image.expression(
                '(A * 0.02) - 273.15',
                {
                  'A' : image.select('LST_Day_1km')
                // rename the band LST_Day_1km to LSTD_C
                }).rename('LSTD_C'))});

// Add the nighttime LST to the map window specifying parameters for
visualization.
Map.addLayer(cLSTN, {
  bands: "LSTN_C",
  min: 14, max: 22,
  palette: ['blue','white','red']}, "Night LST", DISPLAY);

// Add the daytime LST to the map window specifying parameters for
visualization.
Map.addLayer(cLSTD, {
  bands: "LSTD_C",
  min: 30, max: 46,
  palette: ['blue','white','red']}, "Day LST", DISPLAY);

// Export classified map to drive
Export.image.toDrive({
           image: cLSTD,
           description: 'MJJ2022MODIS_DayLST',
           crs: "EPSG:4326",
           scale: 1000,
           region: aoi,
}

// Export classified map to drive
Export.image.toDrive({
           image: cLSTN,
           description: 'MJJ2022MODIS_NightLST',
           crs: "EPSG:4326",
           scale: 1000,
           region: aoi,
}
```

F-4. Landsat 5 GEE LULC code for (a) 1998 (b) 2005, and (c) 2008 (Adapted from NASA Applied Remote Sensing Training (ARSET) program).

```
//****************** FILTER IMAGE COLLECTIONS *****************//
// Center the map view at defined coordinates (longitude/latitude) with
the given zoom level.
Map.centerObject (aoi, 12);

// Assign variables to import and filter the Landsat Collections.
var filtered1998 = ee.ImageCollection("LANDSAT/LT05/C02/T1_L2")
                .filter(ee.Filter.date('1998-05-01','1998-07-30'))
                .filter(ee.Filter.bounds(aoi))
                .filter(ee.Filter.lt('CLOUD_COVER',15))
                .median().clip(aoi).select("SR_B[0-7]*");

// Print the LST image collection arguments to the console.
//*********1998**************
print(filtered1998, 'Filtered Landsat 8');


//****************** RANDOM FOREST MODEL CLASSIFICATION ***************//
//Create palette for the final land cover map classifications
var urbanPalette =
'<RasterSymbolizer>' +
' <ColorMap  type="intervals">' +
    '<ColorMapEntry color="#f0f400" quantity="1" label="bareland"/>' +
    '<ColorMapEntry color="#89e600" quantity="2" label="cropland"/>' +
    '<ColorMapEntry color="#108b1f" quantity="3" label="forest"/>' +
    '<ColorMapEntry color="#acb1bf" quantity="4" label="impervious"/>' +
    '<ColorMapEntry color="#1dacff" quantity="5" label="water"/>' +
  '</ColorMap>' +
'</RasterSymbolizer>';

// Specify the bands to use in the prediction.
var bands = ['SR_B2', 'SR_B3', 'SR_B4', 'SR_B5', 'SR_B7'];

// Merge land cover classifications into one feature class
var featureClass = bareland.merge(cropland).merge(forest)
                .merge(impervious).merge(water);

// Make training data by 'overlaying' the points on the image.
var points = filtered.select(bands).sampleRegions({collection:
     featureClass,properties: ['landcover'], scale: 30}).randomColumn();

// Randomly split the samples for testing the model's accuracy using the
"random" column. Roughly 80% for training, 20% for testing.
var split = 0.8;
var training = points.filter(ee.Filter.lt('random', split));
var testing = points.filter(ee.Filter.gte('random', split));

// Print these variables to see how much training and testing data being
used
print('Samples n =', points.aggregate_count('.all'));
print('Training n =', training.aggregate_count('.all'));
print('Testing n =', testing.aggregate_count('.all'));
```

```
// ********** RUN CLASSIFICATION AND ACCURACY ASSESSMENT ********
// Run the RF model using 300 trees and 5 randomly selected predictors
per split ("(300,5)").
// Train using bands and land cover property and pull the land cover
property from classes
var classifier = ee.Classifier.smileRandomForest(300,5).train({
                features: training, classProperty: 'landcover',
inputProperties: bands});

// Test the model accuracy. Print Confusion Matrix and Overall Accuracy
var confusionMatrix = classifier.confusionMatrix();
print('Confusion matrix: ', confusionMatrix);
print('Training Overall Accuracy: ', confusionMatrix.accuracy());

var kappa = confusionMatrix.kappa();
print('Training Kappa', kappa);

var validation = testing.classify(classifier);
var testAccuracy = validation.errorMatrix('landcover', 'classification');
print('Validation Error Matrix RF: ', testAccuracy);
print('Validation Overall Accuracy RF: ', testAccuracy.accuracy());

var kappa1 = testAccuracy.kappa();
print('Validation Kappa', kappa1);

// Apply the trained classifier to the image
var classified1998 = filtered1998.select(bands).classify(classifier);


//****** DISPLAY LAND COVER CLASSIFICATION******
//Add final map to the display
var finalmap = classified;
Map.addLayer(finalmap.sldStyle(urbanPalette), {}, "Land
ClassificationMJJ");
Map.addLayer(filtered, {bands: ['SR_B3', 'SR_B2', 'SR_B1'], min:8042,
max:13924}, 'Filtered');

//****** EXPORT CLASSIFIED AND UNCLASSIFIED IMAGE TO DRIVE ******
// Export classified map to drive
Export.image.toDrive({
  image: finalmap,
  description: 'MJJ1998LCC',
  crs: "EPSG:4326",
  scale: 30,
  region: aoi,});

// Export unclassified map to drive
Export.image.toDrive({
  image: filtered,
  description: 'MJJ1998Img',
  crs: "EPSG:4326",
  scale: 30,
  region: aoi,});
```

F-5. Landsat 8 GEE LULC code for (a) 2015 (b) 2020, and (c) 2022 (Adapted from NASA Applied Remote Sensing Training (ARSET) program)..

```
//***************** FILTER IMAGE COLLECTIONS ****************//
// Center the map view at defined coordinates (longitude/latitude) with
the given zoom level.
Map.centerObject (aoi, 12);

// Assign variables to import and filter the Landsat Collections.
var filtered2022 = ee.ImageCollection("LANDSAT/LC08/C02/T1_L2")
                .filter(ee.Filter.date('2022-09-01','2022-11-30'))
                .filter(ee.Filter.bounds(aoi))
                .filter(ee.Filter.lt('CLOUD_COVER', 10))
           .median().clip(aoi).select("SR_B[0-9]*");

// Print the LST image collection arguments to the console.
//*********2022**************
print(filtered2022, 'Filtered Landsat 8');

//***************** RANDOM FOREST MODEL CLASSIFICATION***************//
//Create palette for the final land cover map classifications
var urbanPalette =
'<RasterSymbolizer>' +
' <ColorMap  type="intervals">' +
    '<ColorMapEntry color="#f0f400" quantity="1" label="bareland"/>' +
    '<ColorMapEntry color="#89e600" quantity="2" label="cropland"/>' +
    '<ColorMapEntry color="#108b1f" quantity="3" label="forest"/>' +
    '<ColorMapEntry color="#acb1bf" quantity="4" label="impervious"/>' +
    '<ColorMapEntry color="#1dacff" quantity="5" label="water"/>' +
  '</ColorMap>' +
'</RasterSymbolizer>';

// Specify the bands to use in the prediction.
var bands = ['SR_B3', 'SR_B4', 'SR_B5', 'SR_B6', 'SR_B7'];

// Merge land cover classifications into one feature class
var featureClass = bareland.merge(cropland).merge(forest)
                .merge(impervious).merge(water);

// Make training data by 'overlaying' the points on the image.
var points = filtered.select(bands).sampleRegions({collection:
     featureClass, properties: ['landcover'], scale: 30}).randomColumn();

// Randomly split the samples for testing the model's accuracy using the
"random" column. Roughly 80% for training, 20% for testing.
var split = 0.8;
var training = points.filter(ee.Filter.lt('random', split));
var testing = points.filter(ee.Filter.gte('random', split));

// Print variables to see how much training and testing data being used
print('Samples n =', points.aggregate_count('.all'));
print('Training n =', training.aggregate_count('.all'));
print('Testing n =', testing.aggregate_count('.all'));
```

```
// ********** RUN CLASSIFICATION AND ACCURACY ASSESSMENT ********
// Run the RF model using 300 trees and 5 randomly selected predictors
per split ("(300,5)").
// Train using bands and land cover property and pull the land cover
property from classes
// var classifier = ee.Classifier.smileRandomForest(300,5).train({
                features: training, classProperty: 'landcover',
inputProperties: bands});

// Test the accuracy of the model
// Print Confusion Matrix and Overall Accuracy
var confusionMatrix = classifier.confusionMatrix();
print('Confusion matrix: ', confusionMatrix);
print('Training Overall Accuracy: ', confusionMatrix.accuracy());

var kappa = confusionMatrix.kappa();
print('Training Kappa', kappa);

var validation = testing.classify(classifier);
var testAccuracy = validation.errorMatrix('landcover', 'classification');
print('Validation Error Matrix RF: ', testAccuracy);
print('Validation Overall Accuracy RF: ', testAccuracy.accuracy());

var kappa1 = testAccuracy.kappa();
print('Validation Kappa', kappa1);

// Apply the trained classifier to the image
var classified = filtered.select(bands).classify(classifier);

// ****** DISPLAY LAND COVER CLASSIFICATION******
// Add final map to the display
var finalmap = classified;
Map.addLayer(finalmap.sldStyle(urbanPalette), {}, "Land
ClassificationJJ");
Map.addLayer(filtered,{bands: ['SR_B4', 'SR_B3', 'SR_B2'], min:8440,
max:15833}, 'Filtered')
Map.addLayer(lsk)

// ****** EXPORT CLASSIFIED AND UNCLASSIFIED IMAGE TO DRIVE ******
// Export classified map to drive
Export.image.toDrive({
  image: finalmap,
  description: 'SON2022LCC',
  crs: "EPSG:4326",
  scale: 30,
  region: aoi,});

// Export unclassified map to drive
Export.image.toDrive({
  image: filtered2022,
  description: 'SON2022Img',
  crs: "EPSG:4326",
  scale: 30,
  region: aoi,});
```

F-4. Landsat 5 GEE NDVI code for (a) 1998 (b) 2005, and (c) 2008.

```
Map.centerObject(aoi, 11);
// Map.addLayer(aoi);

*******IMAGE COLLECTIONS AND FILTERING*******
var MJJ2005 = ee.ImageCollection("LANDSAT/LC08/C02/T1_L2")
                .filter(ee.Filter.date('2005-05-01','2005-07-30'))
                .filter(ee.Filter.bounds(aoi))
                .filter(ee.Filter.lt('CLOUD_COVER', 50))
                .median().clip(aoi).select("SR_B[0-5]*");

//*******NDVI*******
// NDVI Calculation
var nir0m = MJJ2005.select('SR_B4');
var red0m = MJJ2005.select('SR_B3');
var MJJ2005NDVI =
nir0m.subtract(red0m).divide(nir0m.add(red0m)).rename('NDVI');

// NDVI Display
var ndviParams = {min: -1, max: 1, palette: ['blue', 'white', 'green']};

Map.addLayer(MJJ2005NDVI, ndviParams, 'MJJ2005NDVI');

// NDVI Export
// Export.image.toDrive({image: MJJ2005NDVI, description: 'MJJ2005NDVI',
crs: "EPSG:4326", scale: 30, region: aoi});
```

F-5. Landsat 8 GEE NDVI code for (a) 2015 (b) 2020, and (c) 2022.

```
Map.centerObject(aoi, 11);
// Map.addLayer(aoi);

// *******IMAGE COLLECTIONS AND FILTERING*******
var MJJ2022 =
ee.ImageCollection("LANDSAT/LC08/C02/T1_L2").filter(ee.Filter.date('2022-
05-01','2022-07-30'))

.filter(ee.Filter.bounds(aoi)).filter(ee.Filter.lt('CLOUD_COVER', 10))
                    .median().clip(aoi).select("SR_B[0-9]*");

// *******NDVI*******
// NDVI Calculation
var nir2m = MJJ2022.select('SR_B5');
var red2m = MJJ2022.select('SR_B4');
var MJJ2022NDVI =
nir2m.subtract(red2m).divide(nir2m.add(red2m)).rename('NDVI');

// NDVI Display
var ndviParams = {min: -1, max: 1, palette: ['blue', 'white', 'green']};

// Map.addLayer(MJJ2022NDVI, ndviParams, 'MJJ2022NDVI');

// NDVI Export
// Export.image.toDrive({image: MJJ2022NDVI, description: 'MJJ2022NDVI',
crs: "EPSG:4326", scale: 30, region: aoi});
```